



HAL
open science

Electrical and optical manipulation of exchange bias

Zongxia Guo

► **To cite this version:**

Zongxia Guo. Electrical and optical manipulation of exchange bias. Physics [physics]. Université de Lorraine; Beihang university (Pékin), 2023. English. NNT : 2023LORR0204 . tel-04536551

HAL Id: tel-04536551

<https://hal.univ-lorraine.fr/tel-04536551>

Submitted on 8 Apr 2024

HAL is a multi-disciplinary open access archive for the deposit and dissemination of scientific research documents, whether they are published or not. The documents may come from teaching and research institutions in France or abroad, or from public or private research centers.

L'archive ouverte pluridisciplinaire **HAL**, est destinée au dépôt et à la diffusion de documents scientifiques de niveau recherche, publiés ou non, émanant des établissements d'enseignement et de recherche français ou étrangers, des laboratoires publics ou privés.



**UNIVERSITÉ
DE LORRAINE**

**BIBLIOTHÈQUES
UNIVERSITAIRES**

AVERTISSEMENT

Ce document est le fruit d'un long travail approuvé par le jury de soutenance et mis à disposition de l'ensemble de la communauté universitaire élargie.

Il est soumis à la propriété intellectuelle de l'auteur. Ceci implique une obligation de citation et de référencement lors de l'utilisation de ce document.

D'autre part, toute contrefaçon, plagiat, reproduction illicite encourt une poursuite pénale.

Contact bibliothèque : ddoc-theses-contact@univ-lorraine.fr
(Cette adresse ne permet pas de contacter les auteurs)

LIENS

Code de la Propriété Intellectuelle. articles L 122. 4

Code de la Propriété Intellectuelle. articles L 335.2- L 335.10

http://www.cfcopies.com/V2/leg/leg_droi.php

<http://www.culture.gouv.fr/culture/infos-pratiques/droits/protection.htm>

Thèse

**Présentée et soutenue publiquement pour l'obtention du titre de
DOCTEUR DE L'UNIVERSITE DE LORRAINE**

Mention : Physique

par

Zongxia Guo

Electrical and optical manipulation of exchange bias

21/10/2023

Membres du jury:

Bert KOOPMANS, Professeur, TU Eindhoven	Président de jury
Pietro GAMBARDILLA, Professeur, ETH Zurich	Rapporteur
Giovanni FINOCCHIO, Professeur, University of Messina	Rapporteur
Jianhua ZHAO, Professeur, Institute of Semiconductors, CAS	Examinatrice
Stéphane MANGIN, Professeur, Université de Lorraine	Directeur de thèse
Weisheng ZHAO, Professeur, Beihang University	Co-directeur de thèse

Résumé

La croissance rapide des applications d'intelligence artificielle crée une demande importante de solutions matérielles avancées. L'industrie des semi-conducteurs recherche activement des technologies de stockage de nouvelle génération capables d'améliorer la vitesse, la densité, la consommation d'énergie et l'évolutivité. L'une de ces technologies est la mémoire MRAM (Magnetic Random Access Memory), qui stocke les informations dans l'état magnétique des matériaux. Toutefois, compte tenu de la demande constante de scénarios à haute densité et ultrarapides, l'antiferromagnétique en tant qu'unité de stockage de données de base présente des avantages évidents. Les matériaux antiferromagnétiques ont un magnétisme macroscopique négligeable, ce qui les rend très résistants aux champs magnétiques externes. Cette propriété permet également l'absence d'interactions dipolaires entre les cellules adjacentes, ce qui permet une intégration à plus haute densité. En outre, les matériaux antiferromagnétiques présentent une dynamique à haute fréquence jusqu'à la gamme des térahertz, ce qui permet théoriquement des vitesses d'écriture plus rapides que les dispositifs ferromagnétiques. Cependant, ces moments magnétiques entièrement compensés rendent l'état d'aimantation du matériau antiferromagnétique difficile à manipuler et à détecter.

Dans cette thèse, nous démontrons une commutation de biais d'échange antiferromagnétique dans des jonctions tunnel magnétiques à trois bornes et réussissons à détecter électriquement l'antiferromagnétisme par magnétorésistance à effet tunnel. Ce résultat est obtenu en imprimant l'état antiferromagnétique IrMn sur la couche libre de CoFeB. Nous obtenons également une commutation de l'IrMn dépendant de la polarité du courant, plutôt que de l'orientation du courant, jusqu'à 0,8 ns. Nous identifions deux mécanismes de commutation, le mode de chauffage et le mode induit par le couplage spin-orbite, en fonction de la largeur de l'impulsion de courant. Ce dernier est étayé par des simulations numériques, qui suggèrent que le couplage spin-orbite généré par le Pt induit la précession de l'IrMn et que le couplage d'échange à l'interface IrMn/CoFeB détermine la polarité de commutation de l'IrMn.

En outre, pour briser la précession ferromagnétique et la limite de vitesse d'écriture électrique, nous avons modifié expérimentalement le biais d'échange avec une seule impulsion laser femtoseconde. Dans la structure IrMn/CoGd, le biais d'échange a été modifié par un seul laser femtoseconde, et la dépendance des variations du biais d'échange par rapport à différentes fluences laser et nombres d'impulsions a été étudiée en détail. Des mesures résolues dans le temps sont utilisées pour démontrer que l'échelle de temps de commutation du biais d'échange est inférieure à 100 ps. Les simulations atomistiques montrent que l'IrMn présente une démagnétisation plus rapide que les matériaux ferromagnétiques, et que chaque grain d'IrMn se remagnétise en un seul domaine en seulement 2 ps. La manipulation électrique et optique du système de biais d'échange permet un contrôle ultra-rapide, sans champ et énergétiquement efficace de l'antiferromagnétique avec une température d'ordre élevée et une stabilité thermique, ce qui le rend tout à fait approprié pour des applications.

Mots clés : Antiferromagnétique, ferrimagnétique, biais d'échange, MRAM, commutation tout-optique

Abstract

The rapid growth in today's artificial intelligence applications is creating a significant demand for advanced underlying hardware. Industries are actively seeking next-generation storage technologies to satisfy the massive data storage and efficiency processing. Magnetoresistive random-access memory (MRAM) offers exceptional performance in terms of non-volatility, fast read and write speeds and power consumption. With the continuous requirement of high-density and ultrafast scenarios, antiferromagnet as the basic data storage unit shows great advantages. Antiferromagnetic materials have negligible macroscopic magnetism, making them highly robust to magnetic fields. This property also allows for the absence of dipole interactions between adjacent cells, enabling higher-density integration. Additionally, antiferromagnetic materials exhibit high-frequency dynamics up to the terahertz range, theoretically enabling faster write speeds than ferromagnetic devices. However, the lack of macroscopic magnetization makes antiferromagnet particularly hard to detect and manipulate. One conventional and effective approach is to use the exchange bias, where the antiferromagnet is controlled by the orientation of a coupled ferromagnet, which can then be detected using conventional means.

In this thesis, we demonstrate the exchange bias switching in a three-terminal magnetic tunnel junction (MTJ) device and realize electrical detection of antiferromagnetism by tunnel magnetoresistance (TMR). This is achieved by the unidirectional anisotropy from exchange-coupled CoFeB ferromagnetic and IrMn antiferromagnetic layers. We further achieve current polarity-dependent switching, rather than current orientation-dependent switching of IrMn down to 0.8 ns. We identify two switching mechanisms, the heating mode, and the spin-orbit torque driven mode, depending on the current pulse width. The latter case is supported by numerical simulations, which suggest that spin-orbit torque generated by Pt induces the precession of IrMn and exchange coupling at the IrMn/CoFeB interface determines the switching polarity of IrMn.

Furthermore, to break the ferromagnetic precession and electrical write speed limit, we experimentally realize exchange bias switching by a single femtosecond laser pulse. In the IrMn/CoGd bilayer, the perpendicular exchange bias is investigated for various IrMn thicknesses and CoGd concentrations. We demonstrated the exchange bias switching under a single femtosecond laser, and the dependence of the exchange bias variations with different laser fluence and pulse numbers was investigated. The time-resolved MOKE measurement is used to demonstrate the exchange bias switching timescale of less than 100 ps. The atomistic simulations show the IrMn exhibits even faster demagnetization than ferromagnetic materials and each IrMn grain remagnetizes to a single-domain state in only 2 ps. The electrical and all-optical manipulation of the exchange bias system allows ultrafast, field-free, and energy-efficient control of antiferromagnet with high ordering temperature and thermal stability, making it highly suited to applications.

Key words: Antiferromagnet, ferrimagnet, exchange bias, MRAM, all-optical switching

Acknowledgments

I would like to express my deepest gratitude to those who have generously contributed to the completion of my Ph.D. thesis.

First and foremost, my sincere thanks go to my supervisor, Stéphane Mangin. His guidance and support have been crucial throughout this journey. He introduced me to the intricate world of ultrafast magnetism and provided the foundation for my research, and also gave me the opportunity to delve into the topics presented in this thesis, allowing me to fully explore my interests. His constructive feedback on my manuscripts and presentations was very encouraging and led to significant improvements.

I would also like to thank my co-supervisor, Weisheng Zhao from Beihang University. He not only introduced me to the field of spintronics, but also facilitated the collaboration with the Université de Lorraine. His mentorship allowed me the freedom to pursue my research project. Under his guidance, my Ph.D. was focused and resourceful, allowing for rapid progress in my Ph.D. work.

I thank Prof. Pietro Gambardella and Prof. Giovanni Finocchio for reading my manuscript and giving very valuable suggestions in the brief reports, as well as the Prof. Jianhua Zhao as my Ph.D. jury. I am especially grateful to Prof. Bert Koopmans for being the president of my defense. The discussions we had during the defense are very helpful for my thesis.

I would like to thank Michel Hehn and Grégory Malinowski for their invaluable contributions. It was a privilege to work with them and I greatly appreciated our insightful discussions, their accessibility and their comprehensive explanations of both experimental and theoretical aspects of this Ph.D. topic. Their constructive feedback and suggestions have greatly enriched my work.

For this thesis, I would like to thank my colleagues from Beihang University, Daoqian and Ao, who provided extensive help with measurements and theoretical work in Chapter 5. I am particularly grateful to Wei Zhang and Yi Peng for their invaluable help with the optical experiments in Chapter 6. I am also grateful for the collaboration with the University of York, particularly for the invaluable contributions to the atomistic simulations in Chapter 6 by Roy Chantrell, Richard Evans and Junlin Wang.

Special thanks go to Tianxun, who provided essential support when I first arrived in France. I am also grateful to my friend, Hangtian, whose company and help in various aspects of life and works have been invaluable. Navigating a foreign country, especially with a limited knowledge of French, was no small feat. Among them, I would like to thank Lin Liu, Tao Wang, Sheng Wan, Mengxi Zhou, Wei Yang, Chen Lv, Xiaofei Fan, Junxiao Lin, Junta Igarashi, Eva Díaz, Anna-Maria Friedel and Héloïse Damas.

Finally, I would like to thank my parents and family for their unwavering support. I am lucky to have parents who always support my decisions. Despite the distance between Nancy and home, they never hesitated to encourage me to come here.

Contents

Chapter 1. Introduction	1
Chapter 2. State of Art.....	3
2.1 Magnetic storage	3
2.1.1 Magnetic materials	3
2.1.2 Magnetic storage technology	6
2.1.3 Magnetoresistive random-access memory (MRAM).....	13
2.2 Antiferromagnet and exchange bias.....	14
2.2.1 Discovery of exchange bias	15
2.2.2 Néel and Mauri domain wall models	18
2.2.3 Malozemoff random field model	20
2.2.4 Grains and spin-glass-like models	21
2.2.5 Atomistic model of exchange bias	25
2.3 Application and manipulation of exchange bias	27
2.3.1 Spin valve.....	27
2.3.2 Thermally assisted MRAM.....	28
2.3.3 Spin current-induced exchange bias switching.....	29
2.3.4 All-optical manipulation of exchange bias	31
2.4 Summary	34
Chapter 3. Experimental Methods	35
3.1 Fabrication process of spintronic devices	35
3.1.1 Magnetron sputtering	35
3.1.2 Photolithography	36
3.1.3 Etching	38
3.1.4 Dielectric deposition	39
3.1.5 Devices fabrication	40
3.2 Electrical characterization of spintronic devices	43

3.2.1	DC measurement	43
3.2.2	Short-pulse and time-domain measurement	44
3.3	Magneto-optical measurement	45
3.3.1	Magneto-optic Kerr effect (MOKE).....	46
3.3.2	All-optical switching and MOKE microscope	47
3.3.3	Time-resolved MOKE	48
3.4	Summary.....	50
Chapter 4. Double Exchange Bias Magnetic Tunneling Junction (MTJ).....		51
4.1	Double exchange biased MTJ stack design.....	51
4.2	Antiferromagnetic layer thickness dependence.....	54
4.3	IrMn seed layer thickness dependence	55
4.4	Insert layer thickness dependence	56
4.5	The temperature dependence of exchange bias	57
4.6	The field annealing optimization.....	58
4.7	Summary.....	59
Chapter 5. Electrical Manipulation of Exchange Bias		60
5.1	Field-free switching of exchange bias	60
5.2	The endurance and magnetic field immunity	62
5.3	Thermal-assisted and Oersted field-induced switching.....	63
5.4	The short-pulse measurement and sub-nanosecond dynamics.....	65
5.5	Exchange bias switching mechanism	67
5.6	Exchange biased devices with tungsten (W) insert layer	71
5.7	Exchange bias switching in IrMn bottom electrode devices	72
5.8	Summary.....	74
Chapter 6. Manipulating Exchange Bias by a Single Femtosecond Laser Pulse		75
6.1	IrMn/CoGd perpendicular exchange bias bilayer.....	77
6.2	Single-shot laser-induced exchange bias switching	80
6.3	Exchange bias manipulation with multi-pulses	82

Contents

6.4	Timescale for exchange bias switching.....	85
6.5	Atomistic simulation of antiferromagnetic dynamics.....	87
6.6	Summary	93
Chapter 7. Ultrafast Antiferromagnet Rearrangement in Co/IrMn/CoGd Trilayers		94
7.1	Co/IrMn/CoGd double exchange bias trilayer	94
7.2	Interlayer coupling in Co/IrMn/CoGd	95
7.3	Exchange bias switching and ultrafast antiferromagnet rearrangement	97
7.4	Summary	100
Chapter 8. Conclusion.....		101
Bibliography.....		108

Chapter 1.

Introduction

Exchange bias interaction has been widely studied and utilized in various spintronic devices thanks to its ability to provide a strong bias field. There have been numerous theoretical models proposed to explain this effect and questions remain unanswered. Various models developed since the discovery of exchange bias and discuss its specific applications in different spintronic devices. It also highlights recent research on the manipulation of the exchange bias effect using various stimuli, which not only allows efficient control of exchange bias but also provides insights into the underlying mechanisms. These findings open up new possibilities for novel spintronic devices. In this thesis, current-induced exchange bias switching has been achieved in a double exchange bias magnetic tunnel junction (MTJ) device. Additionally, the ultrafast magnetization reversal dynamics in antiferromagnetic/ferrimagnetic perpendicular exchange bias heterostructure have been investigated using femtosecond lasers which induce all-optical switching. This research has the potential to offer efficient solutions for antiferromagnet manipulation.

This thesis is organized as follows:

Chapter 2 begins with an introduction to magnetic materials and magnetic data storage and reviews the discovery of exchange bias, the evolution of theoretical models, and its applications for spintronic devices. It specifically focuses on the various proposed theoretical models of exchange bias, as well as the traditional use of exchange bias structure to pin a reference layer. The chapter also summarizes the different technics applied in recent years to manipulate exchange bias.

Chapter 3 begins with a description of the spintronic device fabrication, which covers magnetic film stack deposition, pattern processes, and dielectric deposition. The electrical performance of spintronic device is characterized by DC and shot-pulse measurement. Additionally, the magneto-optical effect and related measurements are introduced as well as ultrafast magnetism measurements based on femtosecond laser.

Chapter 4 focuses on the design of a top-pinned double exchange bias MTJ stack, followed by a detailed study of optimizing the antiferromagnet/ferromagnet (AFM/FM) storage layer. Precise control over the magnetic properties of the storage layer is achieved through thorough investigations into the thicknesses of the antiferromagnetic layer, seed layer, and insert layer. By studying the temperature dependence of exchange bias and exploring optimal annealing conditions, the MTJ stack with ideal properties can be obtained. This serves as a foundation for achieving electrical control of exchange bias in the next chapter.

Chapter 5 investigates the exchange bias switching characteristics in a three-terminal MTJ device and analyzes the influence of the Oersted field and Joule heating. Furthermore, it

examines the contribution of thermal or spin-orbit torque (SOT) effects through shot-pulse time-domain measurement. Finally, it investigates the W insert layer thickness dependence and IrMn bottom electrode devices for the optimizing the power consumption in writing process.

Chapter 6 delves into the ultrafast manipulation of exchange bias by femtosecond laser. It provides a detailed characterization of the IrMn/CoGd (AFM/FiM) perpendicular exchange bias heterostructure, including the thickness of antiferromagnet IrMn, concentration of ferrimagnet CoGd, and temperature dependence. This chapter also presents experiments on the ultrafast repeatable switching of exchange bias, exploring the dependence on laser fluence and pulse number. Time-resolved measurement confirms that the exchange bias switching occurs within a timescale of 100 ps. Atomistic simulations are used to further explore the mechanism of exchange bias switching, sub-picosecond dynamics and probabilistic switching behavior of antiferromagnetic grains.

Chapter 7 realizes the manipulation of exchange bias in Co/IrMn/CoGd (FM/AFM/FiM) trilayers with double perpendicular exchange bias. The quasi-static characteristics show the IrMn thickness-dependent interlayer interaction of the double exchange bias interface. The single femtosecond laser-induced exchange bias switching indicates the ultrafast rearrangement of the AFM spins at the IrMn/CoGd interface and further demonstrates the competition across the AFM volume orders.

Chapter 8 provides a conclusion and discusses the perspective of this thesis.

Chapter 2.

State of Art

In this chapter, we will provide an overview of the magnetic materials and their respective properties and the progress made in magnetic storage and spintronic devices. We will discuss the utilization of antiferromagnetic materials in spintronic devices and then focus on the discovery, modeling, and manipulation of antiferromagnetic exchange bias. We also summarize the spin-valve applications and different techniques employed in recent years to manipulate exchange bias. This comprehensive review will set the foundation for the research objectives and main content of this thesis.

2.1 Magnetic storage

2.1.1 Magnetic materials

Magnetism origin from the interaction of electrons in their orbits and spins. Different types of magnetic materials respond differently to magnetic fields. In fact, all materials have part of magnetism, but the magnetization varies depending on the interactions between the atoms' magnetic moments[1]. Magnetization \mathbf{M} changes over the magnetic field \mathbf{H} , can be described $\mathbf{M} = \chi \mathbf{H}$, where the χ is the susceptibility of the materials.

Diamagnetic materials have a zero magnetic moment due to all electron orbitals being fully occupied, leaving no unpaired electrons. When a magnetic field is applied, the magnetic moment produced by the electron orbital momentum opposes the field, resulting in an additional magnetic moment in the opposite direction illustrated in Fig. 2.1(b). Diamagnetic materials typically exhibit a relative permeability χ below 1 and a magnetization \mathbf{M} below 0, usually around 10^{-5} . It is important to note that all materials exhibit diamagnetism.

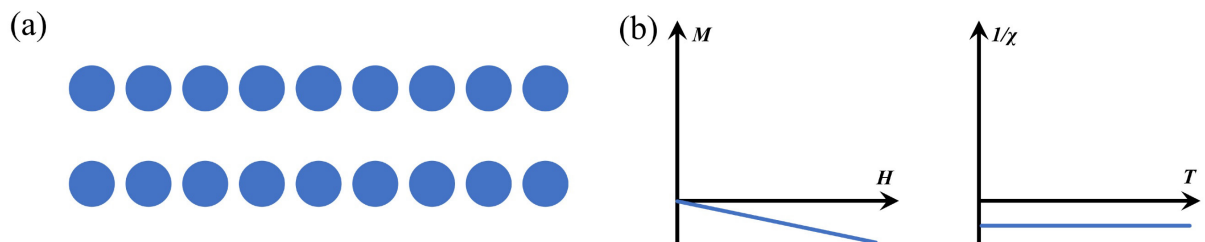


Fig. 2.1 (a) Schematic of diamagnetic materials. (b) Magnetization of the diamagnetic materials produces magnetic moments in opposite directions with the increase of the magnetic field, and the relative permeability remains constant with the change of temperature.

Paramagnetic materials possess electron orbitals that are partially filled with unpaired electrons, leading to the net magnetic moment. However, there is no interaction between these magnetic moments, resulting in zero magnetization in the absence of an external magnetic field, as shown in Fig. 2.2(a). When a magnetic field is applied, the atomic magnetic moments

partially align with the field, resulting in a smaller positive magnetization, as shown in Fig. 2.2(b). Typically, at room temperature, the magnetization of paramagnetic materials falls within the range of 10^{-3} to 10^{-5} . Examples of paramagnetic materials include magnesium (Mg), molybdenum (Mo), lithium (Li), and tantalum (Ta).

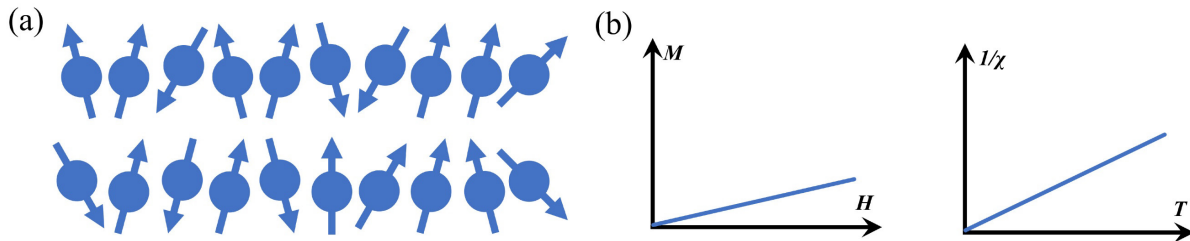


Fig. 2.2 (a) Magnetic moments schematic of paramagnetic materials. (b) Increase in the magnetization of paramagnetic materials with increasing magnetic field produces smaller net magnetic moments, and the inverse of the permeability increases with increasing temperature.

Ferromagnetic materials exhibit strong interactions between atomic magnetic moments, which come from electron exchange interactions. In 1907, Weiss proposed that the presence of molecular fields could explain ferromagnetism[2]. In quantum mechanics, the Heisenberg model provides a detailed description of how neighboring magnetic moments align in parallel due to exchange interactions[3]. Ferromagnetic materials display long-range ordering at the atomic scale, with their unpaired electron spins arranged in parallel within magnetic domains, as shown in Fig. 2.3(a).

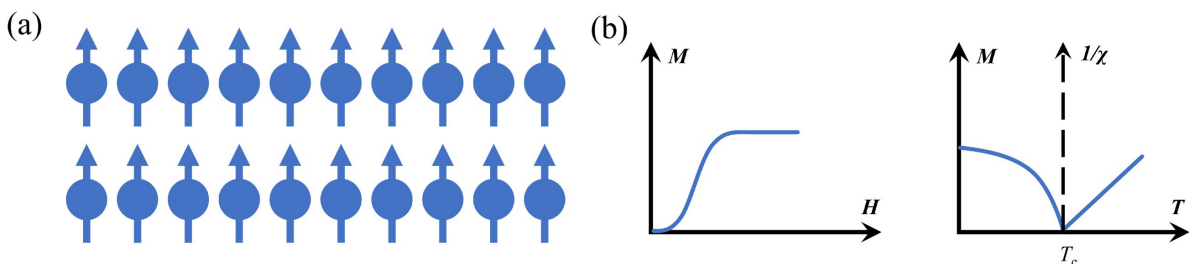


Fig. 2.3 (a) Magnetic moments of the ferromagnetic materials. (b) The magnetization of ferromagnetic material increases and saturates with increasing magnetic field and transforms to paramagnetic after exceeding Curie temperature.

Ferromagnetic materials have two notable characteristics: spontaneous magnetization and magnetic ordering temperature. Spontaneous magnetization refers to the net magnetization that exists within a uniformly magnetized microscopic volume even in the absence of an external magnetic field. At a temperature of 0 K, the magnitude of the magnetization intensity is precisely equal to the magnetic moment of the electron spin. However, despite the strong electron exchange interactions in ferromagnetic materials, these interactions can be overcome at high temperatures, causing the magnetic moments to align randomly and exhibit paramagnetism. As shown in Fig. 2.3(b), the temperature of ferromagnetism transitions to paramagnetism is referred to as the Curie temperature (T_c). Examples of common ferromagnetic materials include iron (Fe), nickel (Ni), cobalt (Co), and certain rare earth elements like gadolinium (Gd) and dysprosium (Dy).

Ferrimagnetic materials are typically made up of alloys that contain multiple elements. In these materials, the exchange interactions between electrons cause the magnetic moments to align opposite in different sublattices, as shown in Fig. 2.4(a). Similar to ferromagnetism, ferrimagnetic materials maintain their magnetic below the Curie temperature, transitioning into a paramagnetic state upon surpassing T_c . However, in ferrimagnetic materials, the sublattices have the same magnitude of magnetic moments at specific temperatures below the T_c . This results in a net zero magnetic moment, as illustrated in Fig. 2.4(b), which is known as the compensation temperature (T_{comp}). Some common examples of ferrimagnetic materials include divalent and trivalent iron oxides, yttrium-iron garnet (YIG), and alloys of transition and rare-earth (TM-RE) alloys.

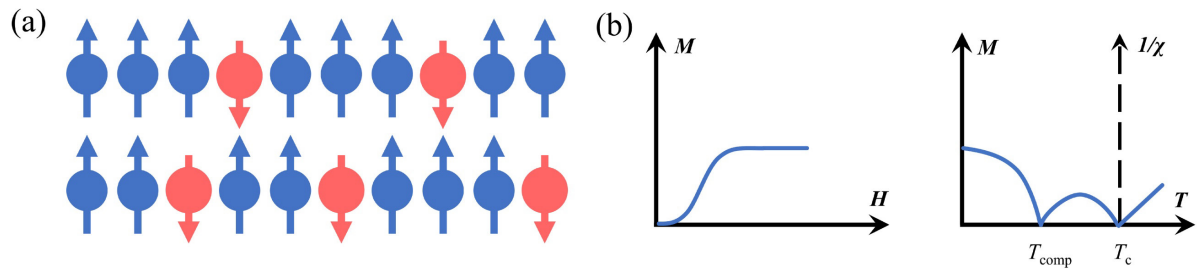


Fig. 2.4 (a) Magnetic moments of ferrimagnetic materials. (b) Magnetization of ferrimagnetic materials increases and saturates with increasing magnetic field, and in the temperature dependence, ferrimagnetic has zero net magnetic moment at the compensation point and becomes paramagnetic beyond the Curie temperature.

Antiferromagnetic materials exhibit a macroscopic behavior similar to paramagnetic materials, showing a weak positive magnetization. Antiferromagnetic materials share similarities with ferromagnetic materials, except that exchange interactions between neighboring atoms cause magnetic moments to align antiparallely, as shown in Fig. 2.5(a). The fully compensated magnetic moments of antiferromagnet show similar behavior with paramagnetic materials. Antiferromagnets also have a transition to paramagnetic behavior at a specific temperature known as the Néel temperature (T_N), as shown in Fig. 2.5(b). Antiferromagnetic materials like nickel oxides (NiO), manganese (Mn) alloys, and chromium (Cr) is the only element in the periodic table that demonstrates antiferromagnetism at room temperature.

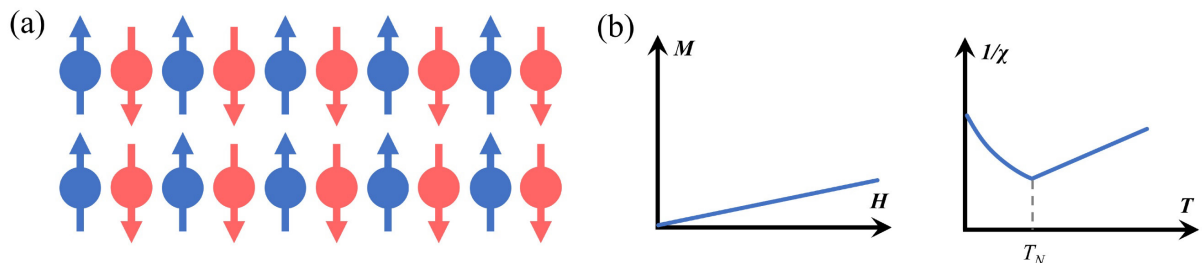


Fig. 2.5 (a) Magnetic moment schematic of antiferromagnetic materials. (b) Antiferromagnetic materials share the similar behavior to paramagnetic materials in an applied magnetic field, and transition paramagnetic over the Néel temperature.

2.1.2 Magnetic storage technology

The magnetic anisotropy of magnetic materials plays a crucial role in magnetic storage. This anisotropy arises from electric fields within solids or crystals, the shape of the magnetic object, or mechanical stresses and tensions. Typically, a magnetic material exhibits spontaneous magnetization that aligns along one or a few specific directions, known as the easy magnetization axis, which corresponds to the lowest energy state. Conversely, there are directions, referred to as the hard magnetization axis, along which magnetization requires the highest energy. Magnetic anisotropy quantifies the energy required to shift the direction of magnetization from the easy axis to the hard axis[4].

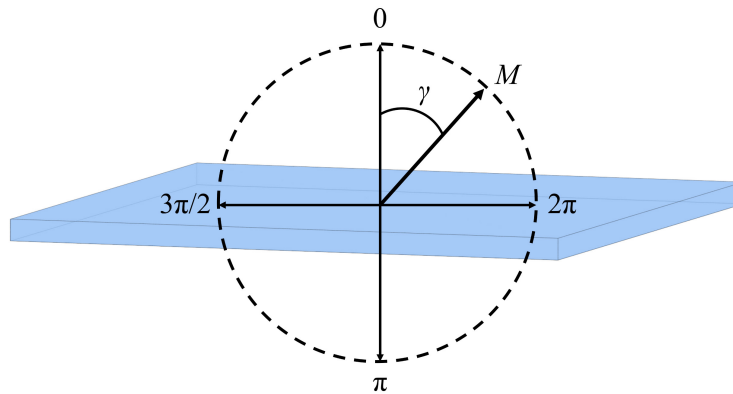


Fig. 2.6 In thin film samples, the γ is defined as the angle between the magnetization and the special axis of the sample.

The energy density E_{ani} associated with magnetic anisotropy is typically determined by the angle of the easy axis and exhibits symmetry around this axis. This type of anisotropy is often referred to as uniaxial anisotropy. As illustrated in the Fig. 2.6, we can express E_{ani} as an even function of the angle γ , which represents the angle between the direction of magnetization and the easy axis.

$$E_{\text{ani}} = K_1 \sin^2 \gamma + K_2 \sin^4 \gamma + K_3 \sin^6 \gamma + \dots \quad (2.1)$$

where K_n ($n=1,2,3 \dots$) is the magnetic anisotropy constant in J/m^3 . Usually, the value of the first order term K_1 is much larger than the other terms, which can be generally approximated as $E_{\text{ani}} = K_1 \sin^2 \gamma$. According to Eq. (2.1), we can see that if the magnetization is perpendicular to the surface, there is $K_1 > 1$; for the magnetization axis in the plane, there is $K_1 < 0$. For magnetic thin film materials, if the direction of the easy axis is perpendicular to the direction of the film plane, the material is called to have perpendicular magnetic anisotropy (PMA), in this case, the direction of the magnetization is perpendicular to the direction of the film plane when the energy is the lowest, and along the direction of the film plane along the energy of the highest; if the direction of the easy axis is parallel to the direction of the film plane, the material is called to have in-plane magnetic anisotropy (IMA), when the magnetization direction has the lowest energy along the in-plane direction and the highest energy along the direction perpendicular to the film.

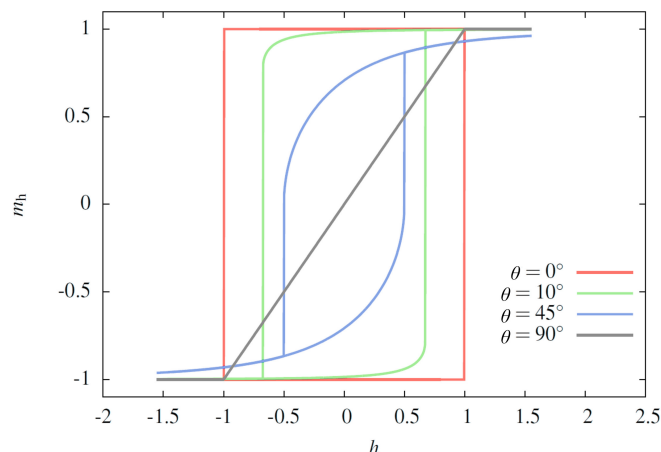


Fig. 2.7 Hysteresis loops when the external magnetic field is at different angles to the easy axis of the sample, showing the maximum coercive field when the external magnetic field is parallel to the easy axis, and a linear hysteresis loop when it is parallel to the hard axis.

In the Stoner-Wohlfarth model, the energy of a single-domain magnetic particle, subjected to an external magnetic field H , magnetic anisotropy constant K , and magnetization M , can be mathematically represented as:

$$E = K \sin^2 \gamma - MH \cos(\theta - \gamma) \quad (2.2)$$

The angles γ and θ , representing the orientations of M and H respectively in relation to the easy magnetization axis, we can determine that the energy of the single-domain particle exhibits two minima at γ values of 0° and 180° . These minima are separated by an energy barrier. By solving the above equation numerically, we can obtain the hysteresis loop for the single domain particle, as shown in Fig. 2.7. The shape of this loop depends on the angle θ of the external field relative to the easy axis. If the external field H aligns with the hard magnetization axis, no hysteresis loop will be observed. In this case, the direction of M will change linearly with increasing magnetic field H . However, if the external magnetic field H aligns with the easy magnetization axis, the direction of magnetization will abruptly reverse when H reaches the coercive field H_c . This hysteresis phenomenon is the basis for magnetic materials as a storage media, where the up or down state of magnetization can be represented as binary "0" or "1".

Valdemar Poulsen invented the world's first publicly available magnetic storage device, which was showcased at the 1900 Paris World's Fair. In 1928, Fritz Pfleumer created the first magnetic tape recorder for analog sound signals. Presently, data tapes utilized in data centers are employed for recording binary data. The most prevalent magnetic storage device in use today is the hard disk drive (HDD). The first hard drive made by IBM had a capacity of approximately 5 MB and comprised 50 disks, each with a diameter of 24 inches and a face-recording density of only 2 Kb/in². In 2014, the data recording density had surged to 1 Tb/in², marking a remarkable increase of about 600 million times in the past 60 years. This tremendous growth can be attributed to the optimization of materials for magnetic storage media and the scaling down of read/write components[5].

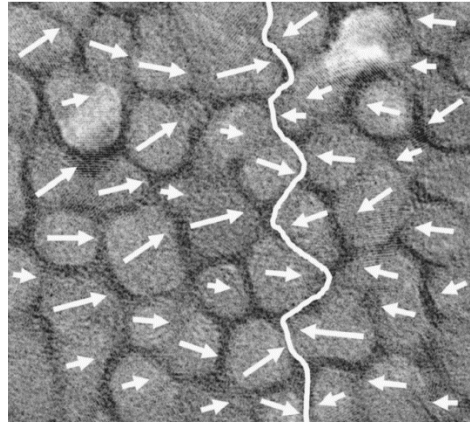


Fig. 2.8 Magnetic grains and magnetic domain wall on the disk surface in an HDD[5].

A conventional HDD usually consists of a disk for data storage, a read/write head, and a control system. The disk substrate is typically made of aluminum (Al) or glass, which is coated with a magnetic thin film. The magnetic film is commonly polycrystalline with sub-micron magnetic domains, each containing numerous magnetic grains, as shown in Fig. 2.8. In the beginning, the longitudinal magnetic recording media (LMR) is employed (Fig. 2.9(a)), which involved magnetic recording parallel to the disk surface. However, with the increase in data storage density, the size of magnetic particles has been further reduced. Consequently, the inherent magnetic anisotropy energy barriers have weakened, leading to the spontaneous magnetization of the grains fluctuating due to thermal excitation. When the heat approaches the minimum of the potential barrier, the grains will unpredictably switch between two magnetization states, resembling a large paramagnetic magnetic moment. This phenomenon is referred to as superparamagnetic behavior. After 2005, perpendicular magnetic recording media (PMR) was developed to enhance the storage density of HDD and reduce the spacing between magnetic domains, as shown in Fig. 2.9(b). This advancement allowed storage capacity to reach the Tbit[6].

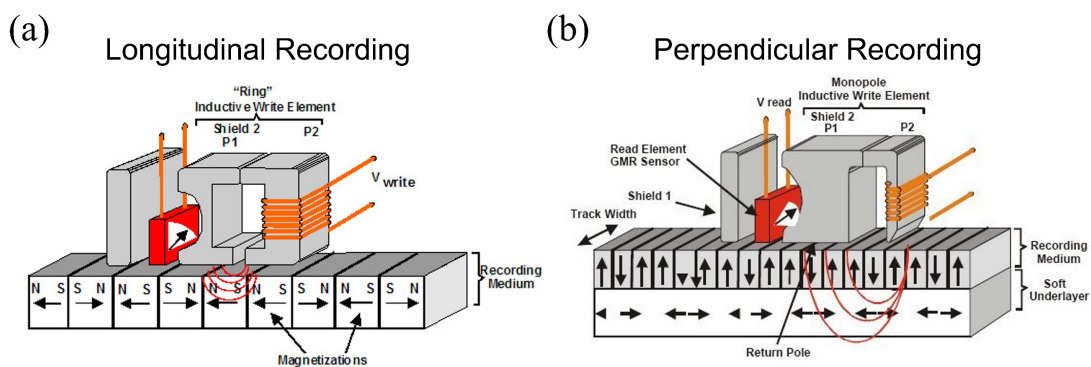


Fig. 2.9 Read/write heads structure of HDD with (a) longitudinal recording media and (b) perpendicular recording media techniques[6].

The advancement of HDD read/write technology and the enhancement of disk storage density go hand in hand. The early HDD utilized read/write integrated inductive heads, where a single inductive coil was responsible for generating both the magnetic field for data writing and the

induced current for data reading from the magnetic storage unit. However, as the size of the magnetic storage unit continued to decrease, the inductive read/write heads were unable to satisfy the required sensitivity for data read/write operations. Consequently, separate read/write head technology was developed. The write component of the separate head consists of a soft magnetic yoke and an inductive coil, which writes data by utilizing the stray field generated by the gap in the yoke. On the other hand, the read component employs a magnetic thin-film sensor that utilizes the anisotropic magnetoresistance (AMR) effect. Fig. 2.10 illustrates the development of storage densities, key technologies, and compound annual growth rate (CAGR) in HDDs. In 1991, magnetic read heads based on the AMR effect started replacing traditional inductive magnetic read heads. Although the magnetoresistance of the AMR device was initially less than 1%, it significantly boosted the growth rate of disk areal recording density. To further increase recording density, higher sensitivity and thinner magnetic read heads were required. Within eight years of the discovery of the giant magnetoresistance (GMR) effect in 1989, IBM incorporated magnetic heads based on this effect into commercial HDDs, achieving a face density of 2 Gb/in². Subsequently, GMR magnetic read heads have several technological iterations, sustaining a growth rate of areal density at around 60% to 100%. In 2005, Seagate introduced the first magnetic read head based on the tunnel magnetoresistance (TMR) effect. The TMR effect offered a much higher magnetoresistance rate compared to the GMR effect, enabling recording areal density to surpass 100 Gb/in² to 1 Tb/in² with continues improvements in materials and device integration technology[7][8][9].

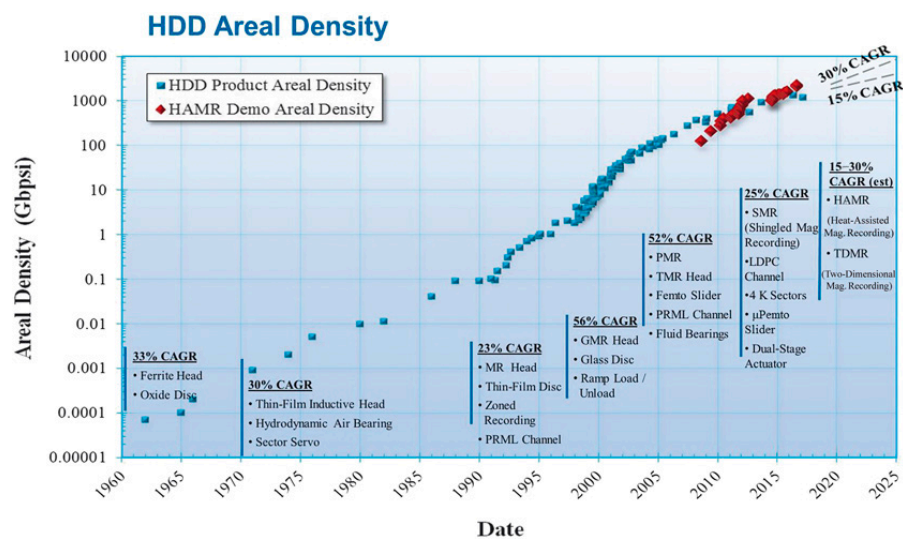


Fig. 2.10 Development in HDDs’ data areal density, key technologies, and compound annual growth rate (CAGR)[9].

The GMR effect, a significant discovery in spintronics, was independently made by Prof. Albert Fert of the University of Paris XI, France, and Dr. Peter Grunberg of the Jülich Institute, Germany, in 1988 and 1989, respectively[10][11][12]. This discovery had a rapid application in the magnetic read heads of hard drives (IBM, 1997), greatly contributing to the advancement of the information industry. In recognition of their groundbreaking work, both professors were awarded the Nobel Prize in Physics in 2007. Fig. 2.11(a) illustrates the magnetoresistance

phenomenon observed by Fert's group in a Fe/Cr antiferromagnetically coupled multilayer layer in 1988[11]. It demonstrates that the resistance of the Fe/Cr multilayer film gradually decreases as the applied magnetic field increases. This decrease in resistance occurs because the magnetic moments of each Fe layer gradually align in parallel under the external field. The resistance of the multilayer film is minimized when the external magnetic field is over the switching threshold. Moreover, by increasing the number of repetitive layers and reducing the thickness of the nonmagnetic spacer layer, the change in resistance of the multilayer film under the external magnetic field becomes more pronounced. In the $[\text{Fe}(3.0)/\text{Cr}(1.2)]_{60}$ multilayer, the magnetoresistance effect can reach nearly 80%. This value is one to two orders of magnitude higher than that of the AMR devices previously used. The GMR effect's discovery and subsequent developments have had a profound impact on the field of spintronics and have revolutionized magnetic read head technology, leading to significant advancements in the storage industry.

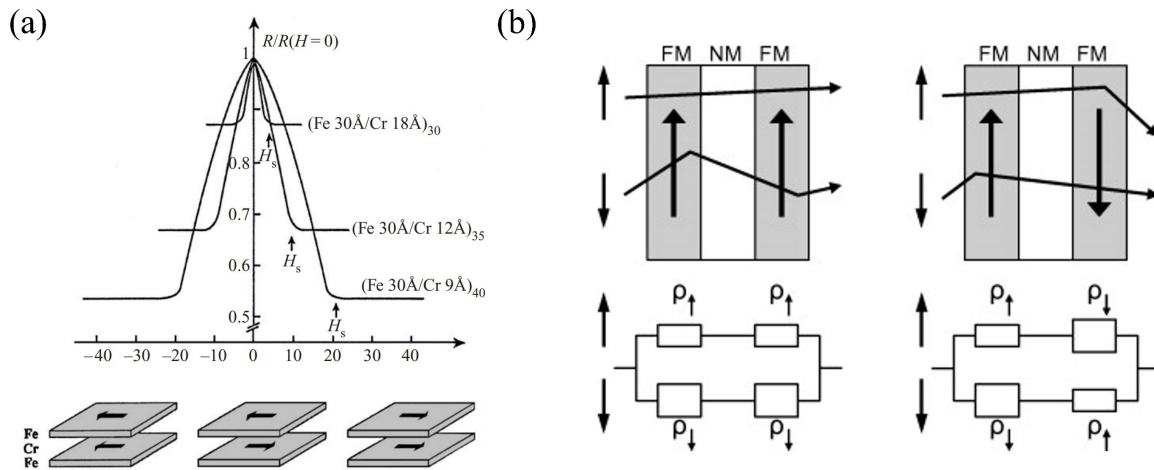


Fig. 2.11 (a) GMR effect in $[\text{Fe}/\text{Cr}]_n$ multilayers, the magnetoresistance increases with the increase of the repetition period of the multilayers; (b) Schematic diagram of the two-current model[11].

The physical mechanism behind the GMR effect is the spin-correlated scattering of electrons within ferromagnetic materials. This concept of spin-correlated scattering was initially proposed by Mott and is based on the two-current model[13]. The two-current model is a simplified theoretical framework that divides the transport of conduction electrons into two distinct pathways: one for spin-up electrons and another for spin-down electrons. These pathways are considered independent and parallel to each other, with different distribution functions and relaxation times for electron spins. In a ferromagnetic/nonmagnetic/ferromagnetic sandwich structure, as depicted in Fig. 2.11(b), the magnetic moments of the left and right ferromagnetic layers can be in either a parallel or antiparallel state. In the parallel state, spin-up electrons must pass through two ferromagnetic layers with the same magnetization, resulting in the spin-down path being equivalent to a series connection of two smaller resistors, R_L . Similarly, spin-down electrons also pass through two ferromagnetic layers with opposite magnetization, making the spin-up path equivalent to a series connection of two larger resistors, R_H . The resulting equivalent resistance can be calculated as $R_P = 2R_H R_L / (R_H + R_L)$. In the

antiparallel state, both spin-up and spin-down electrons need to pass through the antiparallel ferromagnetic layers consecutively. Thus, each spin path is equivalent to a series connection of a large resistor R_H and a small resistor R_L , with an equivalent resistance of $R_{AP} = (R_H + R_L)/2$. The magnetoresistivity is defined as $MR = (R_{AP} - R_P)/R_P$, which can be written to $MR(R_H - R_L)^2/4R_H R_L$, in this sandwich structure. This simplistic resistive model not only provides a qualitative explanation of the GMR effect but also highlights the relationship between magnetoresistance and scattering asymmetry. However, the resistive model is inadequate when explaining the GMR effect in in-plane current structures within a thin layer thickness and spin-valve configurations. This is because the resistive model assumes that the electron mean free path for both spin-up and spin-down channels is greater than the thickness of each layer, rendering it inapplicable when the thickness of the ferromagnetic or nonmagnetic layer exceeds the electron mean free path.

The magnetic tunneling junction (MTJ) based on the TMR effect is similar to the GMR device. The MTJ consists of two layers of ferromagnetic layer (FM) separated by an insulating barrier layer. The resistance state of an MTJ is also determined by the magnetization direction of the two ferromagnetic layers[14]. When the magnetization directions are parallel, the MTJ exhibits low resistance (Fig. 2.12(a)). Conversely, when the magnetization directions are antiparallel, the MTJ demonstrates a high resistance state (Fig. 2.12(b)). The energy perspective shows the principle of spin-correlation tunneling. In Fig. 2.12(c), when the magnetization directions are parallel, electrons in the "majority-spin" subband of FM2 tunnel through the barrier layer into FM1 and occupy the empty state of the "majority-spin" subband. Similarly, electrons in the "minority-spin" subband of FM2 also tunnel into FM1 and occupy the empty

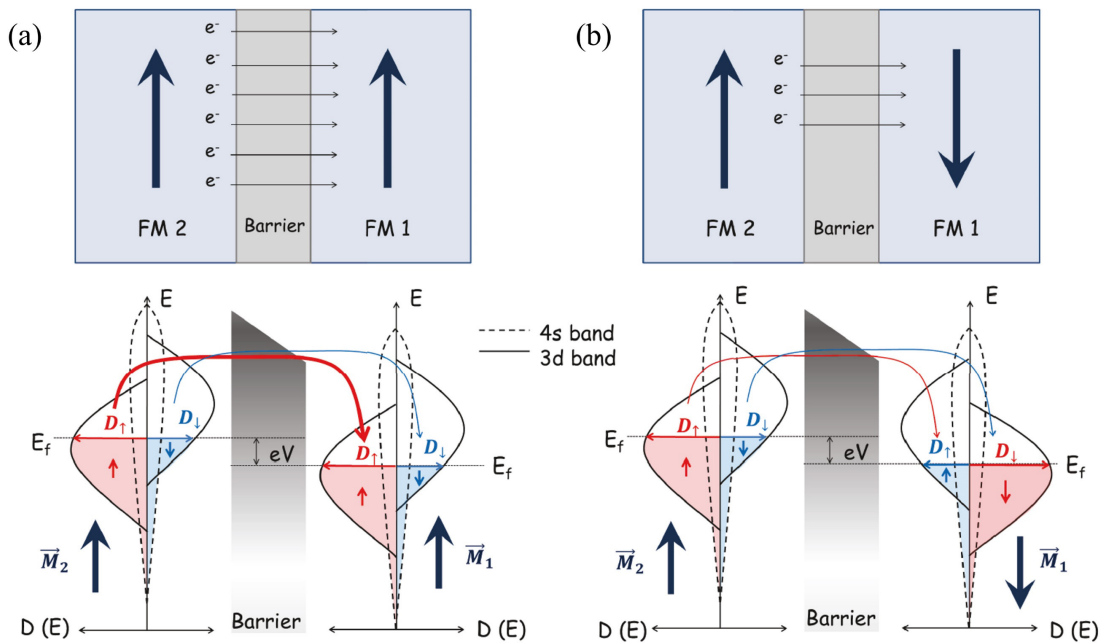


Fig. 2.12 (a) FM1 and FM2 magnetization directions are parallel; (b) FM1 and FM2 magnetization directions are antiparallel. D_{\uparrow} and D_{\downarrow} represent the densities of states of the ferromagnetic layer on the Fermi surface for "majority spin" and "minority spin"[15].

state of the "majority-spin" subband. Additionally, electrons in the "minority-spin" subband of FM2 tunnel into the empty state of the "minority-spin" subband of FM1. This results in a low-resistance state for the entire MTJ. In contrast, when the magnetization directions are antiparallel (Fig. 2.12(b)), the tunneling transport occurs in the "majority-spin" subband of FM2. Electrons in the "majority-spin" subband of FM2 enter FM1 and occupy the empty state of the "minority-spin" subband. Simultaneously, electrons in the "minority-spin" subband of FM2 enter FM1 and occupy the empty state of the "majority-spin" subband. This reduction in the number of electrons involved in transport within the MTJ leads to a high-resistance state. The magnitude of the TMR effect is commonly quantified by the tunneling magnetoresistance ratio as follows:

$$TMR = \frac{R_{AP}-R_P}{R_P} \times 100\% \quad (2.3)$$

The R_P represents the resistance when the magnetization directions of the two ferromagnetic layers are parallel and R_{AP} represents the resistance when the magnetization directions are antiparallel.

In 1975, Prof. Jullière from France observed a 14% TMR in Fe/Ge-O/Co MTJ at low temperature (4.2 K)[16]. However, reproducing this result proved to be challenging, and for the next two decades, no one was able to repeat it. Eventually, in 1995, Prof. Miyazaki and colleagues at Tohoku University in Japan, as well as Prof. Moodera and colleagues at MIT in the USA, independently discovered TMR of 18% and 12% at room temperature, respectively, in MTJs utilizing amorphous Al-O as a barrier[17][18]. Since then, despite continuous optimization of electrode materials and process conditions of Al-O, the tunneling magnetoresistance of MTJs with Al-O as a barrier has only reached a maximum of 81%[19].

In 2001, Mathon and colleagues predicted through first-principles calculations that epitaxially grown single-crystal Fe/MgO/Fe (001) junction could achieve a TMR of more than 1000%[20]. This was attributed to the fact that in MTJs with single-crystal MgO as the barrier layer, the wavefunctions' symmetry leads to different probabilities of electron tunneling into another ferromagnetic layer. As a result, single-crystal MgO exhibits a selective effect on polarized electrons[21]. Consequently, Jullière's model, which explains the TMR of MTJs with amorphous Al-O as the barrier layer, is no longer applicable to those with single-crystal MgO as the barrier layer. In the same year, Yuasa's group [22] and Parkin's group [23] experimentally achieved TMR close to 200% in single-crystalline Fe/MgO/Fe and single-crystalline CoFe/MgO/CoFe, respectively. This breakthrough led to the widespread application of MgO-based MTJ devices, not only as sensors for magnetic read heads in HDD but also resulted in the development of MRAM.

2.1.3 Magnetoresistive random-access memory (MRAM)

Among the range of non-volatile storage technologies available today, MRAM based on spintronic technology stands out as a promising candidate for the next generation of memory technology. MRAM offers exceptional performance in terms of non-volatility, fast read and write speeds, compatibility with CMOS back-end-of-line processes, and remarkable capabilities for high-density integration. These advantages have resulted in the active endorsement of MRAM by leading chip manufacturers. The fundamental storage unit in MRAM is an MTJ, and the TMR ratio is a critical parameter for evaluating its performance. Currently, most MRAM implementations utilize the change in magnetoresistance as the method for data reading. As technology has progressed and the demand for low power consumption has increased, the magnetoresistive state writing method for MTJs has undergone multiple generations of improvement. Fig. 2.13 portrays the current development roadmap of MRAM, considering factors such as power consumption, speed, and process nod[27].

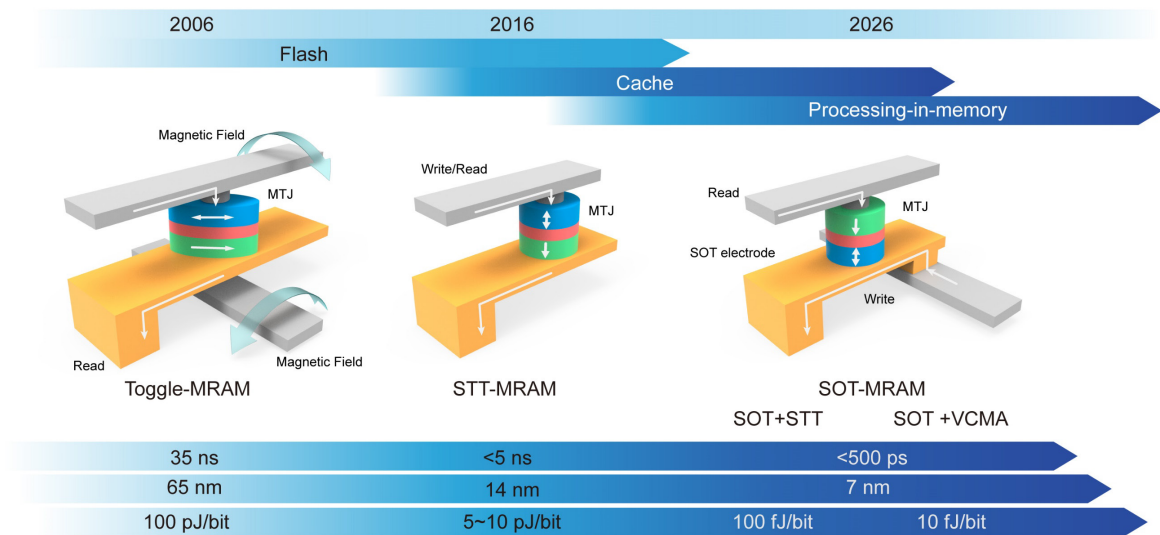


Fig. 2.13 Spintronic devices technology development roadmap[27].

Based on magnetic field-switch writing mode, Toggle-MRAM is the first generation of commercial MRAM[24]. A vital advantage of field switching is its unlimited write endurance, since reversing the free-layer magnetization with a magnetic field does not create any wear-out effect. However, it has difficulties in scaling down and power reduction to adapt to advanced technology nodes. The second generation of commercial MRAM uses current-induced spin-transfer torque (STT) switching to program the MTJ[28]. As a result of the spin filtering synergistic effect, STT switching can achieve relatively high efficiency (5-10 pJ/bit). For higher STT switching speed and efficiency, perpendicular magnetic anisotropy magnetic tunnel junction (p-MTJ) has become a research emphasis. In 2019, reliable 2 ns writing for the last level cache application has been demonstrated[29]. Due to the high density and fast write speed, the leading industries like Intel[30], Samsung[31], and GlobalFoundries[32] are releasing perpendicular STT-MRAM products as a cost-effective option for IoT, general-purpose microcontrollers, automotive, edge-AI, and other low-power applications.

However, fast switching requires a large current through the thin tunnel barrier of MTJs, which accelerates the aging of the barrier and leads to reliability issues[33]. The discovery of spin-orbit torque (SOT) switching by applying an in-plane charge current through a heavy metal channel in three-terminal devices provides a promising alternative mechanism[34]. SOT switching can enhance the endurance, switching speed and reliability of MRAM because of the separation of the read and write current paths in an MTJ, avoiding the electrical stress of the tunnel barrier during writing. However, an external magnetic field collinear with the SOT current is required to accomplish deterministic switching of MTJs with PMA. This intrinsic constraint limits the practical application of SOT-MRAM. Various methods for field-free switching of the SOT are under intensive investigation, among which the joint effect could be a potential solution that combines SOT and other effects like the STT effect[35][36] or voltage-controlled magnetic anisotropy (VCMA) effect[37][38] to assist switching in p-MTJs. The interplay of SOT and STT can break the symmetry to acquire field-free switching and obtain lower power dissipation (in the range of 10-100 fJ/bit) by reducing critical write current density. Besides, compared to SOT+STT, synergy with VCMA offers the potential to further reduce power dissipation and enhance scalability by eliminating the need for STT currents.

Owing to the non-volatility of MRAM, data can be retained in the absence of a power supply. Thus, by leveraging MRAM in caches and main memory to replace SRAM and DRAM, the leakage power dissipation could be dramatically reduced. Moreover, to further increase the computational energy efficiency, STT and SOT-MRAM have been exploited in diverse processing-in-memory architectures, where computations are performed in add-on processing circuits in proximity to memory units or within memory units with operation results generated in peripheral circuits or MRAM array. Both spintronics deterministic and stochastic computing show extensive application prospects with high energy efficiency in various domains, including neural networks and security.

2.2 Antiferromagnet and exchange bias

Throughout the development history of magnetic storage, the pursuit of higher data storage density and faster read/write speeds has been constant, whether in HDD or MRAM. Currently, perpendicular shape anisotropy (PSA) MTJ devices have proven effective even at a diameter of 2 nm[39]. In the latest heat-assisted magnetic recording (HAMR) technology, the diameter of FePt alloy grains used as storage media has been reduced to less than 5 nm[9]. SOT-MRAM has achieved magnetization switching in the sub-nanosecond timescale, approaching the limit of ferromagnet precession speed[40]. To further enhance storage density and read/write speed, researchers are now focusing on antiferromagnetic materials. Compared to ferromagnetic materials, antiferromagnetic materials possess negligible macroscopic magnetism due to the fully compensated magnetic moments in sublattices, making them resistant to external magnetic fields. Additionally, the absence of macroscopic magnetism eliminates dipole interactions between neighboring bits, preventing bit errors caused by such interactions. Furthermore, antiferromagnetic materials exhibit high-frequency dynamics up to the terahertz range, offering

the potential for faster operation speeds than ferromagnetic devices. The efficient control and detection of the state of antiferromagnets as a storage medium has emerged as a prominent subject recently[40].

However, the zero net magnetic moment characteristic of antiferromagnets presents significant challenges in manipulating the antiferromagnetic spin and detecting its state. In recent years, researchers have made notable advancements in various antiferromagnetic systems. One widely used method involves utilizing heavy metal/antiferromagnet (HM/AFM) heterostructures to manipulate the antiferromagnetic state through the SOT effect generated by the spin current injected from the heavy metal into the antiferromagnetic layer[42], reading the state by use of AMR or anomalous Hall Effect (AHE)[43][45]. Despite the prevalence of this modulation technique in different types of colinear and non-colinear antiferromagnetic materials, the efficiency of manipulation and detection remains limited.

Another method utilizes the exchange coupling between antiferromagnetic and ferromagnetic materials[46][47]. Through a coupled ferromagnetic layer, various techniques for manipulating the ferromagnet can indirectly act on the interfacial antiferromagnetic spins, and the antiferromagnetic state can be represented by the bias field and detected efficiently by using GMR, TMR, or magneto-optical effects. This thesis focuses on the manipulation of antiferromagnet in exchange coupled heterostructures. In the following section, we will provide a comprehensive discussion on the discovery, theoretical advancements, and practical applications of exchange bias at AFM/FM systems, then leading to the introduction of our work in this thesis, which aims to efficiently control the interfacial antiferromagnetic spin using spintronic devices and ultrafast optical laser.

2.2.1 Discovery of exchange bias

In 1956, Meiklejohn and Bean discovered exchange anisotropy in Co/CoO core-shell nanoparticles, which they coined as Exchange Bias (H_e)[48]. This phenomenon occurs at the interface between contacted ferromagnetic and antiferromagnetic materials. Exchange bias causes a shift in the hysteresis loops of the ferromagnet along the magnetic field axis, as depicted in Fig. 2.14(a), which illustrates the exchange bias phenomenon they initially observed. Fig. 2.14(a) shows a symmetry hysteresis loop (dashed line) that represents the Co/CoO particles annealing and cooling in the zero field. The increases in the loop's width, in comparison to that of the single ferromagnetic layers, signifies an enhancement in both the coercive field and anisotropy of the ferromagnet due to interfacial coupling between the antiferromagnet and ferromagnet. As shown in Fig. 2.14(b), the torque of the Co particles varies with the external magnetic field still following $\sin(2\theta)$ determined by uniaxial anisotropy, where θ represents the angle between the magnetization direction and the external magnetic field. The solid line hysteresis loop shows the results after annealing and cooling with the magnetic field. The behavior of the magnetic torque under the external field changes from $\sin(2\theta)$ to $\sin(\theta)$, and the energy peak is reduced from two to one, as shown in Fig. 2.14(c). This is due to the exchange coupling between the ferromagnetic Co and the antiferromagnetic CoO shell, which induced a biased direction of magnetization to the Co, known as unidirectional anisotropy.

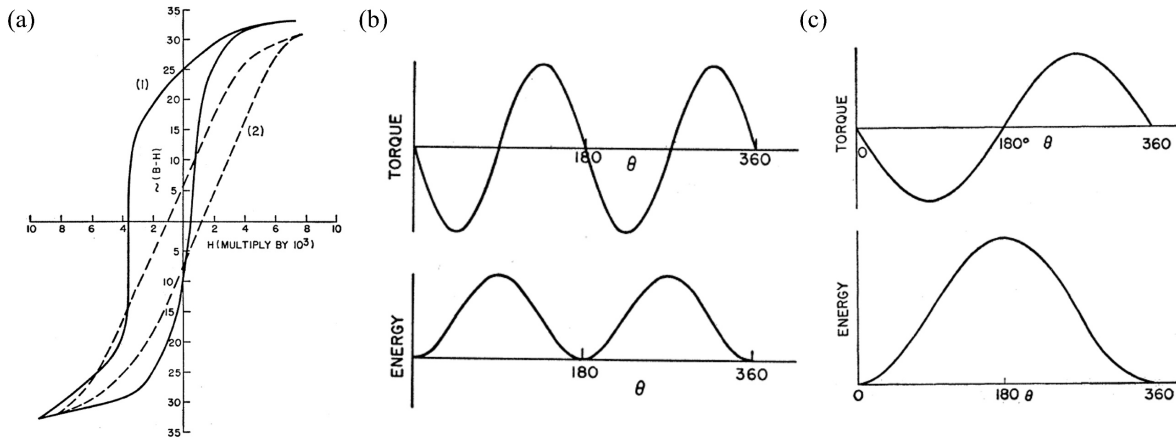


Fig. 2.14 (a) Hysteresis loops in Co/CoO core-shell nanoparticles cooling in zero field (dashed line) or with magnetic field (solid line) at 77 K. (b)(c) Characteristic curves of torque and energy as a function of magnetic field angle in Co particles (without bias) or Co/CoO core-shell particles (with bias).[50].

The exchange bias phenomenon exhibits a significant temperature dependency. Beyond the Néel temperature, the exchange bias field will diminish until it eventually reaches zero. However, at lower temperatures, the exchange bias field completely disappears due to the transition of antiferromagnetic interface grains into a superparamagnetic state. This critical temperature, referred to as the blocking temperature (T_b)[49], represents the point at which the exchange bias field decreases to zero. The determination of the blocking temperature is influenced not only by the interfacial coupling but also by the anisotropic characteristics inherent in the antiferromagnetic grains themselves.

After Meiklejohn and Bean discovered exchange bias, they proposed a macro spin model to explain the interaction between the ferromagnetic layer and the antiferromagnetic uncompensated interface[48][50]. This model aims to provide a better understanding of this phenomenon. By utilizing this model, it becomes feasible to represent the energy of interfacial coupling:

$$E = -HM_F t_F \cos(\theta - \beta) + K_F t_F \sin^2(\beta) + K_{AF} t_{AF} \sin^2(\alpha) - J_{F/AF} \cos(\beta - \alpha) \quad (2.4)$$

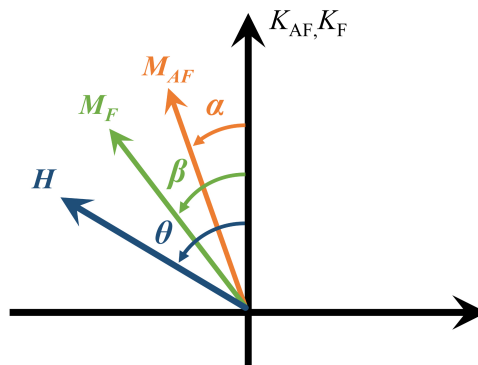


Fig. 2.15 Relationship between antiferromagnetic, ferromagnetic magnetic moment and external field in the Meiklejohn and Bean model.

In Eq. (2.4), H represents the applied external magnetic field, M_F denotes the saturation magnetization strength of the ferromagnetic material, t_F and t_{AF} represent the thicknesses of the ferromagnetic and antiferromagnetic layers, respectively. $J_{F/AF}$ corresponds to the exchange coupling constant at the interface. Additionally, α , β , and θ represent the angles between the antiferromagnetic magnetic moment and the antiferromagnetic easy axis, the angle between the ferromagnetic magnetic moment and the ferromagnetic easy axis, and the angle between the external magnetic field and the easy axis of the ferromagnetic material, respectively. The specific relationships between these angles are illustrated in Fig. 2.15.

Due to the larger anisotropy of the antiferromagnetic layer in comparison to the ferromagnetic layer, the antiferromagnetic moment remains constant when subjected to an external magnetic field, resulting in $\alpha \approx 0$ and $\sin(\alpha) \approx 0$. By taking partial derivatives of Eq. (2.4) with respect to the angular α and β energy terms, the exchange bias field can be expressed as:

$$H_e = -\frac{J_{F/AF}}{M_F t_F} \quad (2.5)$$

The Meiklejohn and Bean model provides a macroscopic perspective on the exchange bias phenomenon, while Eq. (2.5) demonstrates that the magnitude of the exchange bias field is inversely proportional to the thickness of the ferromagnetic layer. This relationship offers insight into the origin of the interface effect responsible for exchange bias and has been supported by experiments[51][52].

However, Meiklejohn's model had limitations as it only considered a finite antiferromagnetic anisotropy. The purpose of this model was to explain the shifted hysteresis loop observed in magnetic moment measurements. When there is exchange bias present, indicated by $K_{AF}t_{AF}/J_{F/AF} > 1$, it signifies that the antiferromagnetic moment remains stable while the ferromagnetic moment rotates in response to an external magnetic field. Conversely, when $K_{AF}t_{AF}/J_{F/AF} < 1$, both the antiferromagnetic and ferromagnetic moments rotate together under the external field. In this scenario, the hysteresis loop does not shift, but there is an increase in the coercive field. This suggests that a thicker antiferromagnetic layer provides greater stability when the ferromagnetic layer switches at a certain $J_{F/AF}$ value. Although this model is simplistic, it demonstrates that the switch of the exchange coupled ferromagnet can impact the interface antiferromagnetic spin, thereby establishing a theoretical foundation for subsequent advancements in ultrafast manipulation of exchange bias. Meiklejohn and Bean provide a macroscopic explanation of the exchange bias phenomenon at the interface of ferromagnetic layers and antiferromagnetic uncompensated interfaces, but at the time further microscopic explanation was still lacking. In the following subsections, we will explore other microscopic models of exchange bias that address these crucial questions:

1. What is the reason that the exchange bias field is much larger than the experimental value in the ideal model?
2. What parameters contribute to the large reduction of the exchange bias field?

3. What is the mechanism for the generation of unsaturated spins at antiferromagnetic interfaces?
4. How does the antiferromagnetic grain structure affect the exchange bias field?
5. What factors determine the temperature dependence of the exchange bias field?
6. What is the relationship between the interface exchange coupling constant $J_{F/AF}$ and the anisotropy of antiferromagnetic?

2.2.2 Néel and Mauri domain wall models

In order to further elucidate the shifted hysteresis loop in the exchange bias phenomenon, Néel expanded Meiklejohn and Bean's theory by incorporating the concept of planar magnetic domain walls in magnetization switching[53]. This extension of the theory accounted for the compression of the antiferromagnetic moment at the interface during the switching of the ferromagnetic layer. Consequently, a part of the exchange coupling energy was stored in the antiferromagnetic domain walls. This energy storage resulted in a reduction of the exchange bias field at the interface, explaining the observed discrepancy between experimentally measured and theoretically predicted exchange bias fields. It is worth noting, however, that Néel's theory is solely applicable to antiferromagnetic layers of considerable thickness and does not adequately address the behavior of thin films with a few nanometers of thickness.

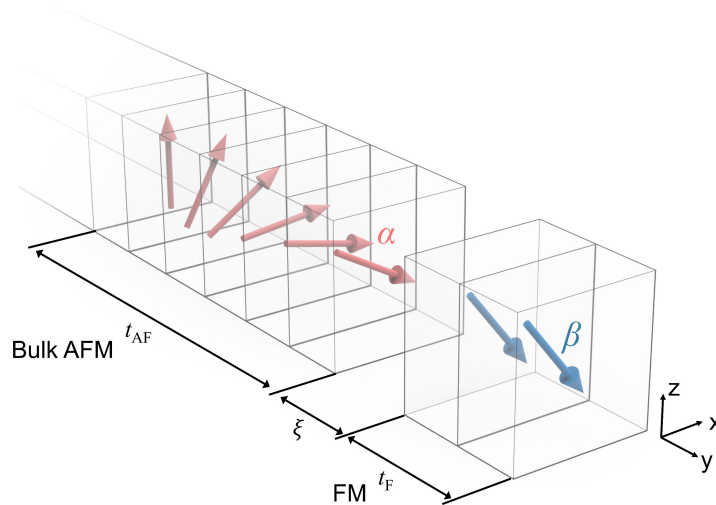


Fig. 2.16 Magnetic domain wall model proposed by Mauri in the exchange coupled AFM/FM bilayer.

In Mauri's model, the magnetic domain walls that result from the switching of the ferromagnetic layer are in close proximity to the interface between the ferromagnet and the antiferromagnet[54], as shown in Fig. 2.16. Mauri analyzed the energy attributed to these magnetic domain walls within the antiferromagnetic layer, which is represented by $2A_{AF}K_{AF}$. In this equation, A_{AF} denotes the antiferromagnetic exchange coupling, while K_{AF} represents the antiferromagnetic anisotropy. Consequently, the total energy within the exchange coupled

system can be expressed as follows:

$$E = 2\sqrt{A_{AF}K_{AF}}(1 - \cos \alpha) + A_{12}/\xi[1 - \cos(\alpha - \beta)] + K_F t_F \cos^2(\alpha - \beta) + HMt_F(1 - \cos \beta) \quad (2.6)$$

In this equation, t_F represents the thickness of the ferromagnetic layer, and ξ represents the interface thickness. K_F and M represents the anisotropy and magnetization of the ferromagnetic layer, respectively, while α and β represent the angles between the antiferromagnetic magnetic moments and the ferromagnetic magnetic moment with the antiferromagnetic anisotropy axis. The first term in Eq. (2.6) corresponds to the energy of the antiferromagnetic domain wall, the second term represents the exchange coupling energy with A_{12} the exchange stiffness at the AFM/FM interface, the third term represents the magnetic anisotropy energy of the ferromagnetic layer, and the final term represents the static magnetic energy. Additionally, Eq. (2.6) can be rephrased as the energy per unit area of the magnetic domain wall:

$$E/A = (1 - \cos \alpha) + \lambda[1 - \cos(\alpha - \beta)] + \mu \cos^2 \beta + k(1 - \cos \beta) \quad (2.7)$$

$$\lambda = \frac{A_{12}}{\xi 2\sqrt{A_{AF}K_{AF}}} = \frac{J_{F/AF}}{2\sqrt{A_{AF}K_{AF}}} \quad (2.8)$$

Eq. (2.7) establishes the relationship between the interfacial coupling energy and the antiferromagnetic exchange coupling strength via λ . If $J_{F/AF} < A_{AF}K_{AF}$, it indicates a weak coupling between the antiferromagnetic and the ferromagnetic layer. Consequently, there will not be a magnetic domain wall, resulting in no contribution to the exchange bias field. On the other hand, if $J_{F/AF} > A_{AF}K_{AF}$, a 180° domain wall will form within the antiferromagnet. In these cases, the exchange bias field can be expressed as follows:

$$\lambda \leq 1, H_e = -2 \left(\frac{\sqrt{A_{AF}K_{AF}}}{\mu_0 M_S t_{FM}} \right) \quad (2.9)$$

$$\lambda \geq 1, H_e = - \left(\frac{J_{F/AF}}{\mu_0 M_S t_{FM}} \right) \quad (2.10)$$

In general, the theoretical model proposed by Néel and Mauri is suitable for thicker antiferromagnetic layers and effectively explains the exchange spring behavior. It also introduces the impact on the antiferromagnetic magnetic order during the ferromagnetic layer switching. However, this model still has the following limitations:

1. The antiferromagnetic magnetic domain walls require both strong interfacial coupling and weak antiferromagnetic anisotropy. Otherwise, from an energy perspective, domain walls will be more favorable to form in the ferromagnetic layer.
2. This model assumes an ideal interface between the antiferromagnet and the ferromagnet.

3. The thickness of the ferromagnetic layer must be significantly smaller than the antiferromagnetic layer, and the magnetization of both layers needs to switch coherently.
4. The model does not account for the effect on the magnetic order of the antiferromagnetic layer during ferromagnetic magnetization switching.
5. Additionally, this model does not explain the observed increase in the coercive field.

These drawbacks highlight the need for further refinements or alternative models to provide a more comprehensive understanding of the exchange bias phenomenon.

2.2.3 Malozemoff random field model

Describing the exchange anisotropy at the microscopic level can be more complex, especially when considering the influence of magnetic structural defects at the interface, as addressed in the Malozemoff random field model[55]. While the models discussed in sections 2.2.1 and 2.2.2 assume an ideal AFM/FM interface, Malozemoff's theoretical study of exchange bias takes into account practical scenarios, such as surface roughness and defects in the antiferromagnetic/ferromagnetic thin films prepared through magnetron sputtering, as depicted in Fig. 2.17. These factors can lead to magnetic frustration at the interface.

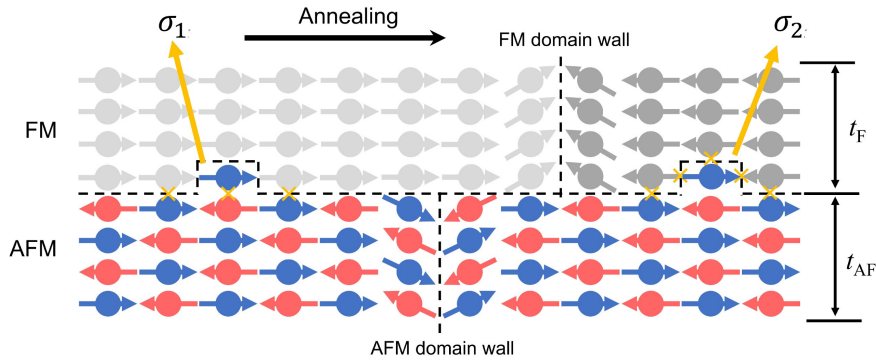


Fig. 2.17 Schematic of a FM/AFM bilayer with a ferromagnetic wall driven by an applied field and vertical domain wall in the AFM layer.

In this context, Malozemoff introduced the concept of interfacial random fields to explain exchange anisotropy. He proposed that magnetic frustration at the interface generates a random field acting between the ferromagnetic and antiferromagnetic layers. As illustrated in Fig. 2.17, if the magnetic domain walls within the ferromagnetic layer move under the influence of an external magnetic field, and the interfacial coupling energies between the antiferromagnetic domains on either side of the domain walls and the ferromagnetic layer differ (σ_1 and σ_2), then the exchange bias field can be equated to the external magnetic field required to drive the magnetic domain walls within the ferromagnetic layer. This relationship can be expressed as:

$$H_e = \frac{\Delta\sigma}{2M_F t_F} \quad (2.11)$$

where $\Delta\sigma$ represents the difference between σ_2 and σ_1 . It is evident that a perfectly compensated ideal interface cannot generate an exchange bias since $\Delta\sigma$ is zero across the entire interface.

However, at an ideal interface, $\Delta\sigma$ can be expressed as $\Delta\sigma = 2J_i/a^2$, where J_i denotes the interfacial coupling constant and a represents the lattice constant. Consequently, the exchange bias field at the interface of an ideal interface can be formulated as:

$$H_e = \frac{J_i}{a^2\mu_0M_F t_F} \quad (2.12)$$

As depicted in Eq. 2.12, the exchange bias field identified is determined by the strength of coupling and exceeds the value generally observed in experimental measurements. To tackle this issue, Malozemoff introduced the concept of a random field that induces unidirectional anisotropy at a localized area but decreases rapidly as the interface area expands. Consequently, the antiferromagnetic layer tends to fragment into multiple magnetic domains to minimize the overall unidirectional anisotropy of the interface.

To further explore the stability of magnetic domain, we suspect that the characteristic length of the frozen AFM domains can be expressed by $L \approx \pi\sqrt{A_{AF}K_{AF}}$. Then we can get the energy change per unit area $\Delta\sigma = 4zJ/\pi aL$ when FM layer is switching. The z is a constant for representing the random interfacial coupling. The exchange bias can be further expressed by:

$$H_e = \frac{2z\sqrt{A_{AF}K_{AF}}}{\pi^2M_F t_F} \quad (2.13)$$

In Eq. 2.13, the predicted magnitude of the exchange bias, as the theoretical model incorporating a random field, aligns much closer to experimental observations. The Malozemoff random field model elucidates the impact of the interfacial spin-glass state on exchange bias, illustrating that magnetic frustration induced by atomic-level interfacial roughness can generate antiferromagnetic magnetic domain walls. In certain cases, this can give rise to antiferromagnetic magnetic domain bubbles.

2.2.4 Grains and spin-glass-like models

Since the 1990s, the use of grain models and spin-glass-like states has become commonplace in explaining the exchange bias phenomenon. The proposal and experimental verification of the spin-glass-like states on exchange bias were conducted by Takano and Berkowit[56]. They further expanded the concept of spin glass to include antiferromagnetic polycrystalline films. In the NiFe/CoO bilayer structure, the exchange bias originates from the presence of uncompensated spins at the antiferromagnetic interface. This magnetic frustration at the interface gives rise to spin-glass-like states, as shown in Fig.2.18(a). Takano's model incorporates the roughness of the AFM/FM interface and CoO polycrystalline films in a single-domain structure, as depicted in Fig. 2.18(b). The model predicts that only 1% of the antiferromagnetic uncompensated interfacial spins contribute to the exchange bias. In 2003, Ohldag et al. observed pinned uncompensated spins at the interface in Co/NiO and Co/IrMn by X-ray Magnetic Circular Dichroism (XMCD). They found that only 4% of the interface layer contains pinned spins[57]. These findings explain why the earlier theoretical models

overestimated the exchange bias field compared to experimental results and indicated the inverse relationship between exchange bias and antiferromagnetic grain size.

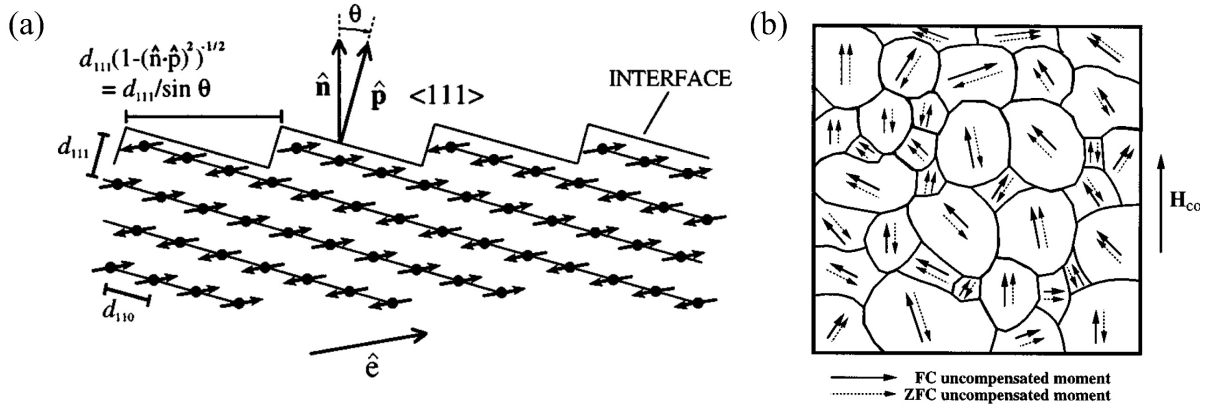


Fig. 2.18 (a) Schematic of antiferromagnetic CoO magnetic moment alignment and interfacial magnetic frustration. (b) Schematic of interfacial antiferromagnetic grains, with antiferromagnetic uncompensated moments randomly aligned after zero-field cooling (dashed arrows); and uncompensated moments have a component along the direction of magnetic-field cooling (solid arrows)[56].

The grains model was initially proposed by Fulcomer and Charap in their investigation of the progressive oxidation process of NiO/Ni, which resulted in grains of varying sizes[58]. By using the Stoner-Wohlfarth model, they analyzed the energy barriers involved in the reversal of antiferromagnetic grains. The contribution of antiferromagnetic grains to the exchange bias is dependent on their size and quantity at a given temperature. The impact of grains on the exchange bias in AFM/FM bilayer films is briefly illustrated in Fig. 2.19. The antiferromagnetic grains are independent of each other without any mutual coupling effect. Each grain possesses a pinning energy of KV , where K represents the anisotropy energy per unit volume, and V denotes the volume of the antiferromagnetic grains. The coupling strength of each antiferromagnetic grain to the ferromagnetic layer is determined by the exchange coupling constant $J_{F/AF}$ per unit area.

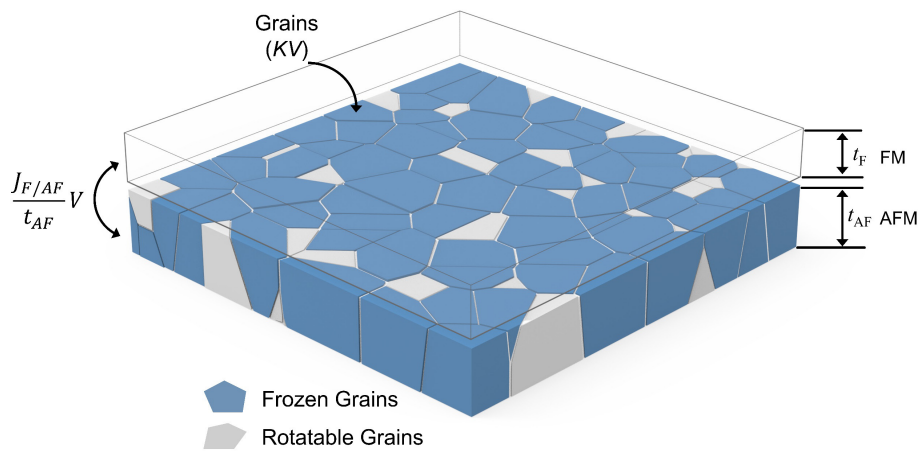


Fig. 2.19 Antiferromagnetic grain structure, blue grains indicate contribution to exchange bias, gray grains indicate unstable grains.

Following the initialization of exchange bias after magnetic field annealing, all grains align themselves in the direction of the ferromagnetic layer during field cooling. The antiferromagnetic magnetic moment of each grain strives to satisfy the exchange coupling at the AFM/FM interface, minimizing the total energy of the system. In the presence of exchange bias, all antiferromagnetic grains experience moments from the exchange interaction of the magnetic moments of the ferromagnetic layer when the ferromagnetic layer is switched by a large external magnetic field. The condition for each antiferromagnetic grain to achieve a reversible process depends on the intrinsic pinning energy (KV), the interface coupling constant ($J_{F/AF}$), and the thermal excitation energy. At a specific temperature, Fulcomer and Charap classified antiferromagnetic grains into three states, as shown in Fig. 2.20(a): (1) Grains exhibiting superparamagnetism that rotate with the ferromagnet switching. These grains contribute to the increase in the coercive field and not to the exchange bias field. This portion of the magnetic moment is referred to as “Rotatable Spin”. (2) Grains with strong antiferromagnetic anisotropy that can maintain their magnetization direction during the ferromagnetic layer switching. This portion of the magnetic moment is called “Frozen Spin” and is responsible for the shift in the hysteresis loop of the ferromagnetic layer. (3) Grains with weaker antiferromagnetic anisotropy but strong coupling to the ferromagnetic layer. These grains contribute to both the increase in the exchange bias field and the coercive field. However, their magnetization direction deviates when the ferromagnetic layer is switched, leading to the reduction of the exchange bias field, which is known as the training effect (Fig. 2.20(b)). In this model, the total energy of the system can be expressed as:

$$E = -HM_F t_F \cos(\theta - \beta) + K_F t_F \sin^2(\beta) + K_{AF} t_{AF} \sin^2(\alpha) + K_{eff}^{SG} \sin^2(\beta - \gamma) - J_{eff} \cos(\beta - \alpha) \quad (2.14)$$

In addition to the initial model proposed by Meiklejohn and Bean, a fourth term is included in the equation to account for the average effective magnetic anisotropy of antiferromagnetic grains under the spin-glass model. This term is represented by $J_{eff} = f \cdot J_{F/AF}$ ($0 < f \leq 1$),

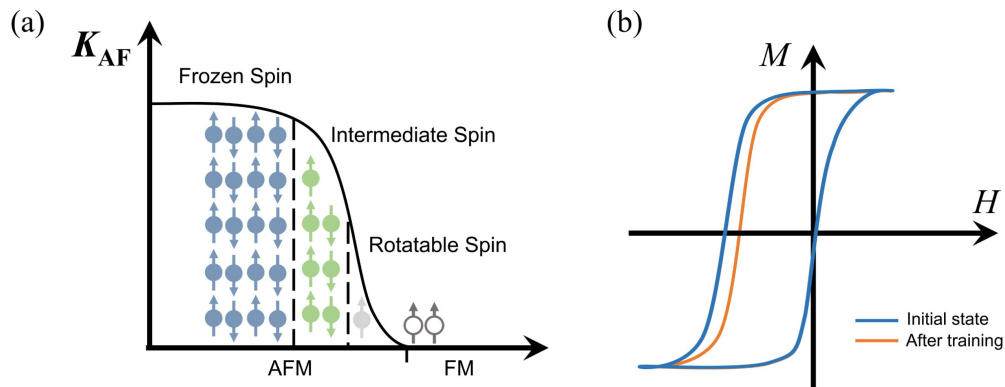


Fig. 2.20 (a) Different behaviors exhibited by antiferromagnetic grains with different anisotropic energies during ferromagnetic layer reversal. (b) Training effect induced exchange bias decreases and gradually stabilizes after numbers of ferromagnetic layer switching.

where f denotes a factor determining the contribution of antiferromagnetic grains, and $K_{eff}^{SG} = (1 - f)J_{F/AF}$. The parameter γ represents the angle of the antiferromagnetic grain's anisotropy along the interface with the average angle between the ferromagnetic easy axis.

Up until now, our primary focus has been on understanding the mechanism of exchange bias itself, largely neglecting the thermal effect of exchange bias. Therefore, we will delve into the thermal excitation process of exchange bias in the polycrystal with multiple grains. The antiferromagnetic anisotropy and interfacial coupling strength are closely associated with temperature. In the grain model, the freezing temperature (T_F) serves as a crucial threshold temperature. Below T_F , the antiferromagnetic spin exhibits spin-glass behavior, while above T_F , it resembles a spin liquid. Over the T_F , the ferromagnetic and antiferromagnetic regions with magnetic frustration become completely decoupled, even though the antiferromagnetic magnetic moment is fully fixed. Conversely, below T_F , the antiferromagnetic and ferromagnetic layers recouple. To characterize the temperature distribution of interface antiferromagnetic grains, the blocking temperature distribution is commonly used[59]. The measurement procedure involves the following steps: (1) The exchange-biased sample is cooled from a magnetic field environment above the blocking temperature T_b to the reference temperature (T_m), typically room temperature (300 K) or a low temperature below 10 K. At this point, the magnetization direction of all interfacial antiferromagnetic grains aligns uniformly with the external magnetic field, as shown in Fig. 2.21(a)(b). (2) The sample is then raised from the reference temperature to a temperature point (T_a) located between T_m and T_b . Subsequently, the sample is cooled back to the reference temperature, and the hysteresis loop in the opposite magnetic field direction is measured, allowing for the determination of the exchange bias field, as shown in Fig. 2.21(c)(d). By repeating these steps, the blocking temperature distribution of the interfacial antiferromagnetic grains can be obtained. This measurement method provides insights into the unlock of the exchange coupling between grains with different antiferromagnetic anisotropies at various temperature points. Such as the choice of antiferromagnetic material and the thickness of the antiferromagnetic layer greatly influence

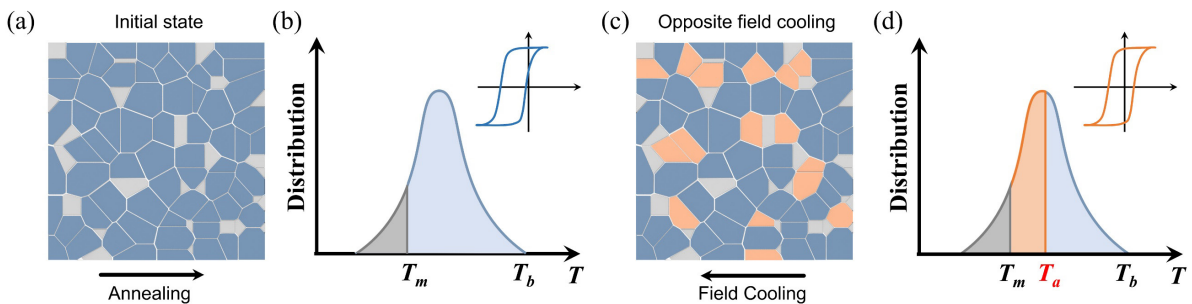


Fig. 2.21 Blocking temperature distribution. (a) (b) After magnetic field annealing, the antiferromagnetic grains oriented along the ferromagnetic layer magnetization. (c) (d) After temperature rising and cooling with a opposite magnetic field, the magnetic moments of some of the antiferromagnetic grains are reversed, and the exchange bias field is reduced.

the characteristics of the blocking temperature distribution. It is important to note that since different antiferromagnetic grains have different T_b and T_F values, the conversion between freezing spin and rotating spin occurs at different temperatures[60]. As the sample temperature gradually decreases, the exchange bias field usually increases, indicating the conversion of a rotating spin into a freezing spin. This conversion provides an additional pinning effect on the ferromagnetic layer.

2.2.5 Atomistic model of exchange bias

The antiferromagnetic IrMn alloys are widely used in spintronic devices. It possesses favorable properties such as high Néel temperature, antiferromagnetic anisotropy, and the ability to generate a strong exchange bias field. However, due to the complex nature of their structure and magnetic properties, the mechanisms behind these characteristics are still being investigated. In a recent study conducted by Sarah Jenkins et al. in 2021, the atomistic modeling of IrMn alloys using the Vampire toolkit indicates the microscopic mechanism of exchange bias in the IrMn/CoFe system, as shown in Fig. 2.22(a)[61][64]. The focus was primarily on two types of IrMn compounds: $L1_2$ -IrMn₃, which exhibits a magnetically ordered and 120° triangular (T1) spin structure, and γ -IrMn₃, which displays a magnetically disordered and 109.5° tetrahedral (3Q) spin structure[63]. Fig. 2.22(b) shows hysteresis loops of the IrMn/CoFe bilayer with $L1_2$ -IrMn₃ and γ -IrMn₃. The results, depicted in the localized, revealed that the

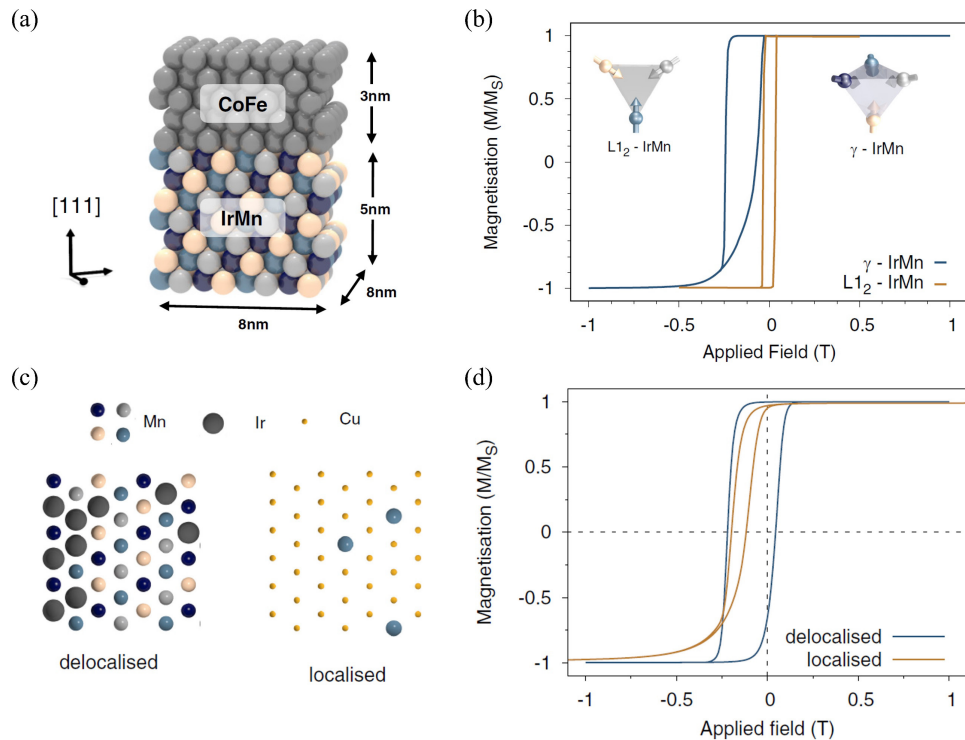


Fig. 2.22 (a) Schematic of the IrMn/CoFe atomistic model; (b) Hysteresis loops in the IrMn/CoFe system with $L1_2$ -IrMn₃ and γ -IrMn₃ antiferromagnetic structures; (c) Atomic structural differences between local and off-domain pinned spins at the interfaces; (d) Comparison of the exchange bias formed by antiferromagnetic local and off-domain pinned spins[61].

magnetically disordered γ -IrMn₃ exhibited a noticeable exchange bias, while the magnetically ordered L1₂-IrMn₃ hysteresis loop displayed no bias and a small coercive field. In the case of the magnetically disordered γ -IrMn₃, the exchange bias was found to originate from the natural disorder of the structure. This disorder led to a slight statistical imbalance in the number of IrMn spins at the interface, resulting in uncompensated magnetic moments that pinned the ferromagnetic layer and caused the exchange bias phenomenon. On the other hand, the magnetically ordered L1₂-IrMn₃ did not exhibit exchange bias in the (111) direction due to the absence of uncompensated spins. However, some exchange bias fields could be observed at the (001) interface. Additionally, in Fig. 2.22(c), the researchers discovered that pinned spins produced exchange bias regardless of whether the interface was localized or delocalized. The delocalized pinned spins were caused by statistical imbalances in the magnetic disorder of the interface, while locally distributed pinned spins were typically the result of interfacial defects, nonmagnetic element doping, or grain boundaries[61], as shown in Fig. 2.22(d).

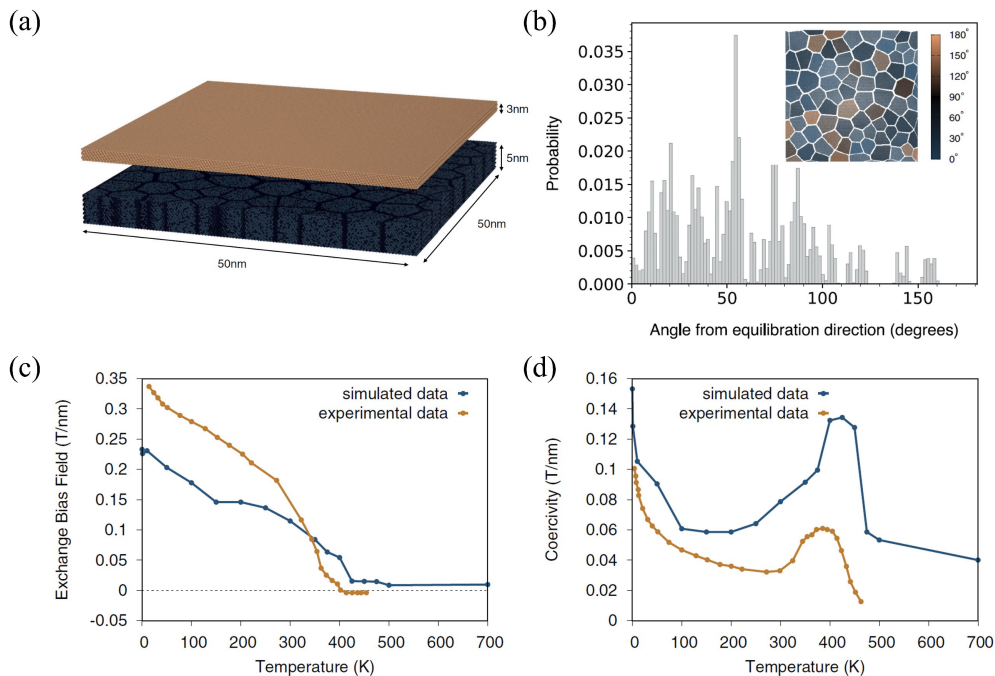


Fig. 2.23 (a) Schematic diagram of the IrMn/CoFe polycrystalline grain model. (b) Statistics of the magnetization direction of IrMn grains after magnetic field cooling, most of the grains that were set up had an orientation deviation of 10° to 60°, while those that were not set up had an angular deviation of more than 150°. (c) (d) Trends of the exchange bias and coercive field as a function of temperature, obtained both in simulation and in experiments[62].

Previously, various models were proposed to explain exchange bias in polycrystalline thin films, assuming that the antiferromagnetic grains had a predefined distribution of magnetic moment directions. However, Jenkins took a different approach by utilizing the local pinning spin distribution of magnetically disordered γ -IrMn₃, without pre-setting the antiferromagnetic magnetic moment direction and anisotropy direction. The results obtained were based on the natural distribution of atoms at the interfaces. To investigate this further, Jenkins modeled the multigrain γ -IrMn₃/CoFe bilayer structure[62], as illustrated in Fig. 2.23(a)(b). Through

simulations of magnetic field cooling, they observed that the magnetic moments of most antiferromagnetic grains aligned with the direction of the cooling field. However, due to the shape of the grains, there were still some grains with magnetization directions different from that set by the magnetic field. In Fig. 2.23(c)(d), the model also captured temperature-dependent properties, such as the variations in exchange bias field and coercive field, which closely matched experimental results. As the temperature approached the blocking temperature, the exchange bias field gradually decreased to zero. Additionally, around 400 K, the coercive field increased due to the coherent switching behavior of the IrMn grain magnetic moment under thermal disturbance. Near the blocking temperature, intermediate switching of the IrMn grains occurred, causing the adjacent ferromagnetic layers to transition from unidirectional anisotropy to uniaxial anisotropy. This implied an enhancement of exchange bias in the opposite direction and a thermal reset in hysteresis loop measurement. Moreover, this thermal resetting led to an increase in the coercivity, even without exchange bias. In this thesis, the exchange bias model developed by Jenkins will also be employed to explain the intricate behavior observed during the ultrafast switching of exchange bias in the presence of a femtosecond laser.

2.3 Application and manipulation of exchange bias

2.3.1 Spin valve

Antiferromagnetic materials have been widely used in magnetic storage applications, although not for storing data directly in the beginning. Their first application was using the interface exchange bias effect to provide a strong bias field for pinning one of the ferromagnetic layers in GMR or MTJ devices, as shown in Fig. 2.24 (a-c). This structure allows for the specific response of only one ferromagnetic layer to external magnetic fields or spin currents and is

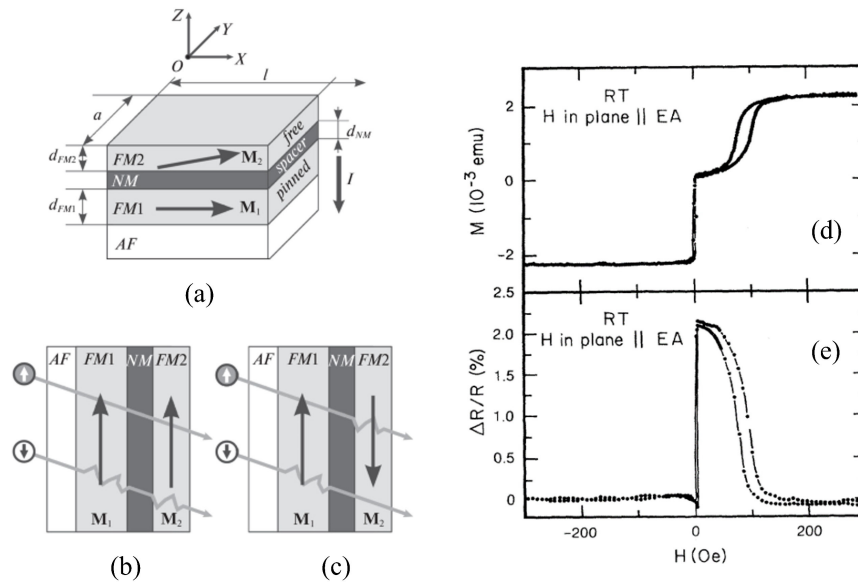


Fig. 2.24 (a) Schematic diagram of the spin valve structure. (b)(c) GMR effect in the spin valve structure. (d) Magnetization curve of the spin valve with various magnetic field. (e) Magnetoresistance curve of the spin valve with various magnetic field[65].

commonly known as a spin valve[65].

The spin valve structure was developed to address the issue of Fe/Cr/Fe multilayers requiring large external fields to overcome the antiferromagnetic coupling of neighboring ferromagnetic layers. In 1990, Dupas et al. discovered that even in GMR multilayers without antiferromagnetic coupling, the GMR effect could still be observed as long as the ferromagnetic layers had different coercive fields [66]. Then, Dieny et al. observed a 5% change in GMR magnetoresistance in a spin valve stack with Si/Ta (5.0)/NiFe (6.0)/Cu (2.0)/NiFe (4.5)/FeMn (7.0)/Ta (7.0) (nm) structure[67]. Fig. 2.24(d) illustrates that as the magnetic field increases, the bottom NiFe layer, which is not pinned by the antiferromagnetic FeMn, switches at 10 Oe. This switching can be observed in the magnetic moment and relative magnetoresistance of the spin valve, indicating that the resistance change is caused by the switching of this ferromagnetic free layer. As the magnetic field continues to increase, the ferromagnetic layer is pinned by the FeMn (beyond 100 Oe), leading to a further increase in the magnetic moment of the spin valve. Simultaneously, Fig. 2.24(e) shows the magnetoresistance curve, the relative resistance decreases as the two ferromagnetic layers align in parallel states.

The spin valve structure offers numerous advantages, making GMR sensors widely used in applications like HDD read heads and electronic compass chips. Following the discovery of the room-temperature TMR effect, the spin valve structure has also been employed in in-plane MTJ devices, where the antiferromagnetic layer provides a pinning effect for the reference layer.

2.3.2 Thermally assisted MRAM

In 2004, Spintec introduced a spin device structure called thermally assisted magnetic random memory (TA-MRAM)[68][70]. It explains how the heating generated near the tunnel barrier when electrons pass through the MTJ can be advantageously used to assist data writing. Applying a heating pulse in combination with an Oersted field pulse allows writing a storage layer that is pinned by an antiferromagnet. This thermally assisted writing scheme allows for circumventing the classical dilemma in storage technologies between thermal stability (memory retention) and writability (write power consumption).

The TA-MRAM device is based on the double exchange biased MTJ, as depicted in Fig. 2.25(a). The antiferromagnet pinning layer for reference has higher blocking temperatures (e.g., PtMn, blocking temperature above 350°C). The storage layer is also pinned by another antiferromagnetic layer and the exchange bias of the storage layer should be large than its coercivity ensuring the existence of only one state at zero field. The antiferromagnetic layer of the storage layer usually chooses thin thickness and low blocking temperature antiferromagnetic materials (e.g., FeMn, IrMn, with a blocking temperature ranging from ~150°C to ~230°C). Fig. 2.25(a-c) shows the thermally assisted writing process: (1) The initial state of the storage layer's hysteresis loop is entirely shifted to the left side of the y-axis, and the device stabilizes in a high resistance state at zero field. (2) To switch the ferromagnetic storage layer, the composite AFM/FM bilayer must be heated above the blocking temperature (around 200°C). It is crucial to control the magnitude of the heating current to prevent the device

temperature from over the blocking temperature of the reference antiferromagnetic layer (approximately 350°C). At this time, the exchange bias field will reduce to zero, allowing the ferromagnetic layer state manipulation by an Oersted field or spin transfer torque. (3) After the heating and writing, the cooling process of the composite storage layer establishes an exchange bias in the opposite direction. Finally, the hysteresis loop of the storage layer is entirely shifted

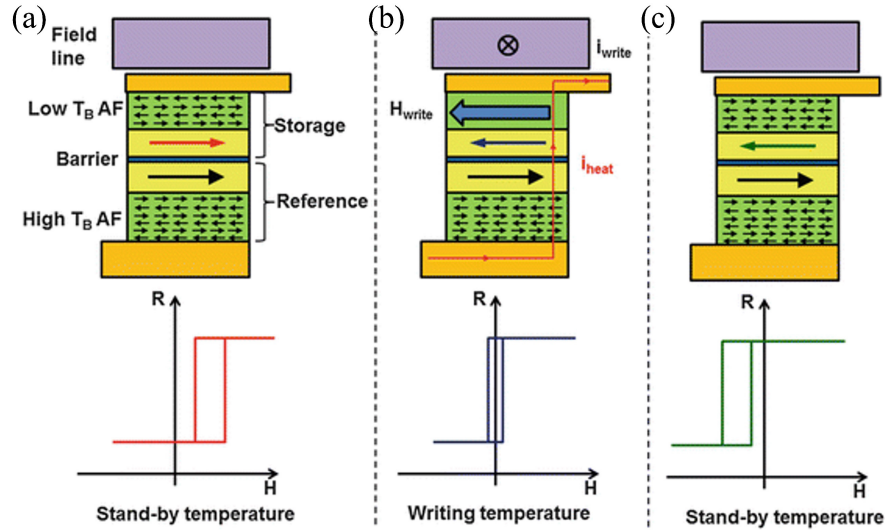


Fig. 2.25 Basic structure and writing principle of a thermally assisted magnetic random memory device: (a) initial state, (b) data writing under the combined effect of heating current and magnetic field current, (c) completion of writing by withdrawing the current.[70]

to the right side, and the device changes to a stable low-resistance state.

The double exchange bias MTJ device offers several advantages compared with Toggle-MRAM. The Oersted field writing mode features a more simplified circuit structure for writing. Furthermore, in the STT write mode, the additional current line for the Oersted field can be completely eliminated. Based on exchange bias, the device size of in-plane MTJ can be miniaturized to less than 20 nm without relying on an elliptical device shape to obtain shape anisotropy. Moreover, the data retention time is extended to over 10 years by leveraging the high anisotropy barrier of the antiferromagnet. However, the development of TA-MRAM meets challenges due to endurance issues. The writing current and heating process greatly affects the lifetime of the MgO barrier.

2.3.3 Spin current-induced exchange bias switching

In the previous section, we noticed the potential of the current-induced SOT as a solution to the antiferromagnet writing efficiency. In antiferromagnetic materials with inversion symmetry breaking, such as CuMnAs[71] and Mn₂Au[72], the antiferromagnetic SOT field-like torque can result in a 90° rotate of the antiferromagnetic Néel vector when applying an orthogonal writing current. For symmetric collinear antiferromagnets, the study of SOT effects follows a similar approach used for ferromagnetic materials, requiring an HM/AFM heterostructure[73]. The SOT damping-like torque generated by heavy metals is utilized to produce equivalent

staggered fields in the two sublattices with opposite magnetization. This results in the tilting and rotating of the antiferromagnetic Néel vector. After the writing current is removed, the antiferromagnetic magnetic moment stabilizes in the direction perpendicular to the spin current polarization, driven by the antiferromagnetic anisotropy field. However, H. Meer et al. have demonstrated that the thermomagnetoelastic switching mechanism in Pt/NiO combined with thermal excitations as the origin, which the final state of antiferromagnet is defined by the strain distributions and heat [74]. The HM/AFM heterostructure can also be applied to manipulate noncolinear antiferromagnet. Y. Takeuchi et al. have observed SOT-induced switching of the magnetization in Mn₃Sn [75]. However, unlike colinear antiferromagnet, this switching is mainly attributed to the effect of SOT on the non-commutative antiferromagnetic chiral self-polarization, which is related to the twisting of the non-colinear antiferromagnetic chiral spin structure. Typically, the electrical readout of antiferromagnetic states is achieved through the utilization of the AMR or the AHE. However, these two relatively weak effects are not sufficient for practical memory applications.

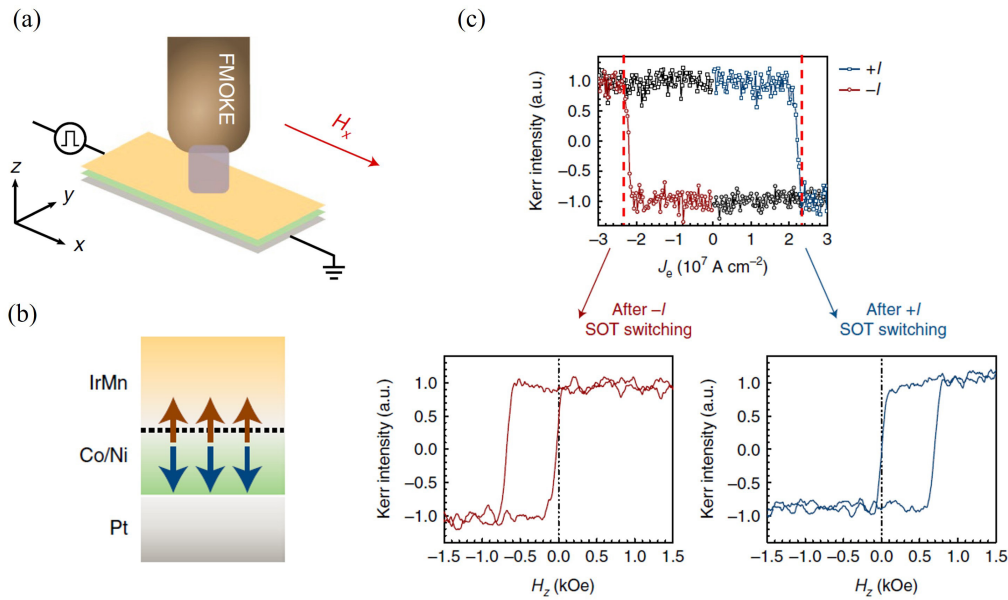


Fig. 2.26 Manipulation of exchange bias using SOT (a) measurement setup, (b) film structure, (c) spin-orbit moment-driven switching of the ferromagnetic layer similarly changes the direction of the exchange bias field[46].

Recent studies have revealed that the SOT effect can serve as an effective method for controlling the exchange bias. In 2019, a research group from Taiwan successfully achieved exchange bias switching at the Co/IrMn interface using the SOT generated by injecting current into the heavy metal Pt in the Pt/Co/IrMn perpendicular exchange bias system[46], as depicted in Fig. 2.26(b). The experimental setup, shown in Fig. 2.26(a), involved the use of a pulsed generator as a driven source and observed the magnetic layer state using the magneto-optical Kerr effect. Fig. 2.26(c) demonstrated the successful manipulation of both the ferromagnetic layer and exchange bias through the SOT effect.

In 2020, Peng et al. from Beihang University achieved a similar exchange bias switching by

utilizing the SOT of IrMn itself. This was accomplished in the IrMn/CoFeB/MgO perpendicular exchange bias multilayer[47], as shown in Fig. 2.27(a)(b). The study demonstrated that independent modulation of both the ferromagnetic layer and exchange bias field is achievable (Fig. 2.27(c)). Fig. 2.27(d) shows the exchange bias reversal follows the SOT-induced CoFeB switching. Moreover, the XMCD and Polarized Neutron Reflectometry (PNR) illustrate that less than 10% of the spins of the Mn atoms at the uncompensated interface of IrMn switches during the exchange bias switching. This small net magnetic moment changes of the Mn atoms at the uncompensated interface of IrMn plays a critical role in the reversal of the exchange bias.

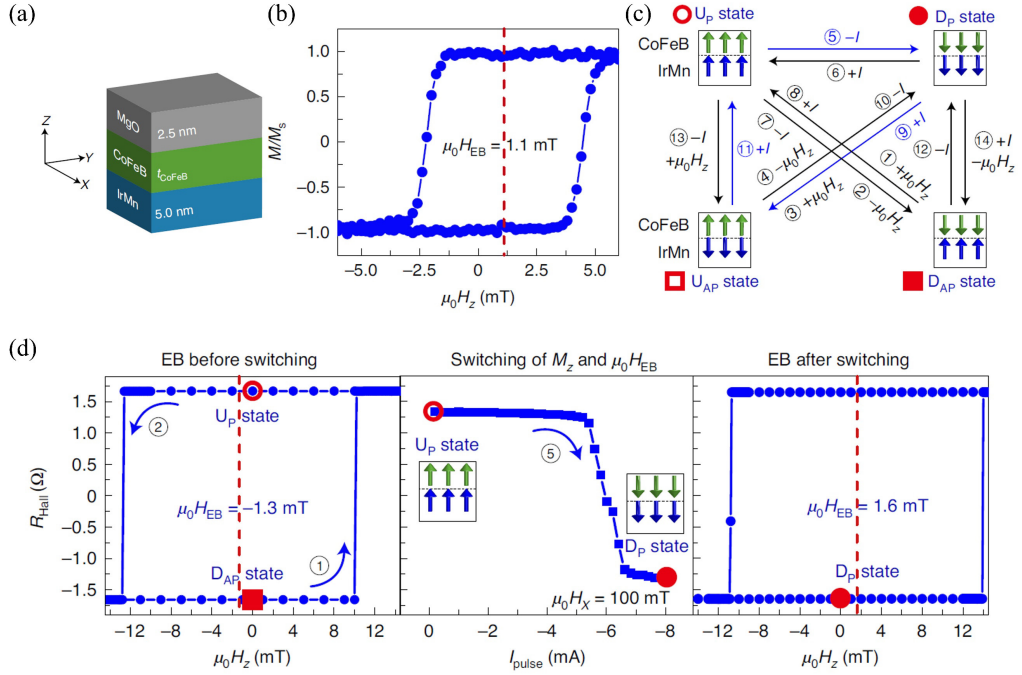


Fig. 2.27 (a) IrMn/CoFeB/MgO stack structure. (b) Hysteresis loop with exchange bias. (c) Independent manipulation of the ferromagnetic layer and the exchange bias, which can be performed under different combinations of SOT current and external magnetic field. (d) Concurrent switching of the magnetization and exchange bias driven by a pulse current[47].

2.3.4 All-optical manipulation of exchange bias

The selection of magnetic materials and the effective manipulation of the magnetic state are crucial in the field of magnetic recording. In removable magnetic storage media, data is stored in tiny magnetic particles, typically a few micrometers or smaller, with their spins either pointing in one direction known as "1" or the opposite direction known as "0". In the case of disks and tapes, an external read/write head is employed to create a small magnetic field for writing these binary bits. In a magneto-optical disk, a laser beam is utilized to heat a ferrimagnetic film over its compensation point, thereby modifying the magnetization state by an applied pulse magnetic field. In 1985, Shieh and Kryder demonstrated that in GdTbCo films, the demagnetizing field can be effectively utilized as a bias field for magnetic field-free thermomagnetic writing[76]. The utilization of GdTbCo, TbCo, and TbFeCo magnetic films with hundreds of nanometers thicknesses enables their application in magnetic storage. But the write speed had not received much attention at this time.

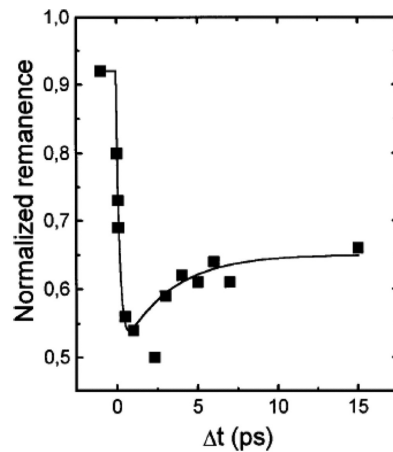


Fig. 2.28 Dynamics of normalized magnetization in the time domain obtained using the pump/probe time-resolved measurement in Ni (20.0)/MgFe₂ (100.0) (nm) thin films[76].

With the development of ultrafast laser technology in the 1980s and 1990s, it became possible to observe both electron dynamics and spin dynamics in the time domain. In 1991, Vaterlaus et al. made an intriguing discovery that the time required for thermal equilibrium to be established between the lattice and spin systems in FeGd alloys, under ultrafast laser excitation, was only 100 ± 80 ps[77]. This finding was later confirmed by Hubner and Bennemann in 1996[78]. In the same year, Beaurepaire et al. demonstrated that Ni thin films could be rapidly demagnetized within 1 ps using 60 fs laser pulses[79]. The results of their time-domain magnetic dynamic experiments are depicted in Fig. 2.28. The utilization of ultrafast laser pulses to manipulate spin dynamics has garnered significant interest due to its potential applications. This field of research, often referred to as ultrafast magnetism, allows for the study of spin dynamics on femtosecond timescales. The remarkably short demagnetization time observed cannot be explained by conventional spin theory, leading to extensive research on ultrafast magnetic dynamics for many years to come.

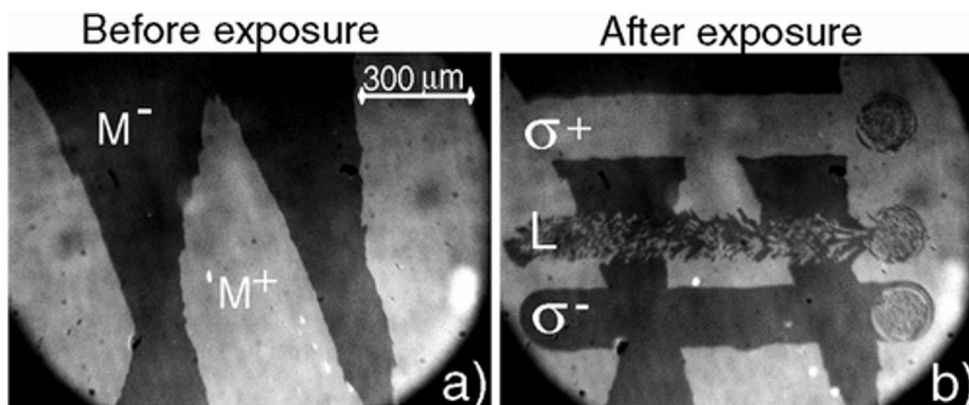


Fig. 2.29 Magnetic domains after the action of ultrashort polarized laser pulses on Gd₂₂Fe_{74.6}Co_{3.4}. (a) Magneto-optical image of the initial magnetic state of the sample before lasing. (b) Line-polarized (L), right-rotating (σ^+) and left-rotating (σ^-) circularly polarized laser scanning the sample surface. The laser-centered area at the end of the scan is at the end of each scanning line, and all of them are made up of small magnetic domains, with the ratio between the upper and lower domains close to 1[80].

Rare earth and transition metal (RE-TM) ferrimagnetic alloys, particularly GdFeCo, have been extensively researched in the context of magneto-optical storage applications. These alloys exhibit strong magneto-optical Kerr signals and possess significant perpendicular magnetic anisotropy, without relying on interfacial effects. In 2007, Stanciu and his colleagues made a significant discovery regarding a ferrimagnetic alloy, $\text{Gd}_{22}\text{Fe}_{74.6}\text{Co}_{3.4}$ [80]. They found that when this alloy was excited by a 40 fs laser pulse and a wavelength of 800 nm, a permanent magnetization switch could be observed. As shown in Fig. 2.29, they observed that right circularly polarized light (σ^+) reversed the magnetization from down to up. However, if the magnetic domains in the irradiated region were already in the spin-up state, the laser pulse had no effect. Similarly, left circularly polarized light (σ^-) converted spin-down to spin-up, but had no impact on the spin-down magnetic domain region. When linearly polarized light was used for irradiation, the region was not switched but instead fragmented into randomly oriented multidomain states. This phenomenon, known as all-optical helicity-dependent switching (AO-HDS), was induced by multiple circularly polarized laser pulses. Stanciu et al. demonstrated that the dependence of AO-HDS on light polarization could be attributed to Magnetic Circular Dichroism (MCD), where the absorption of light by a material with a specific magnetization intensity is influenced by the polarization of the light (or, equivalently, the direction of magnetization that determines the polarization of the light). Another proposed mechanism is the Inverse Faraday Effect (IFE), which has shown potential for altering the magnetization kinetics of low-absorbing materials[81]. However, the precise physical mechanism behind AO-HDS is still being investigated, particularly from an experimental standpoint, and the exact impact of laser spin remains unknown.

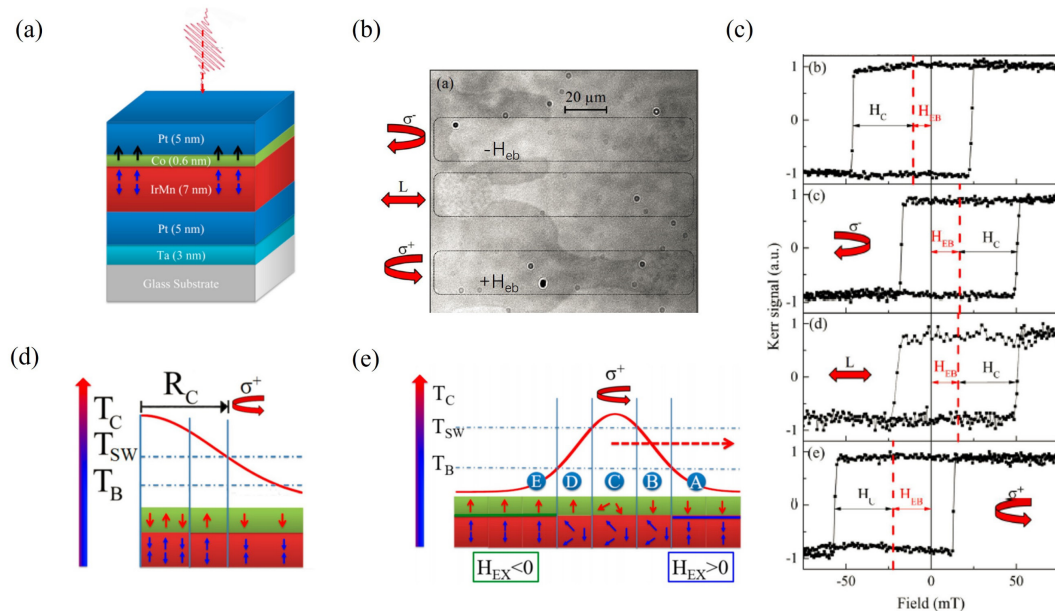


Fig. 2.30 Exchange bias manipulation by all-optical switching (a) membrane layer structure; (b) image of the AO-HDS flip experiment; (c) exchange bias in the region after irradiation with different polarized light; (d) schematic diagram of the temperature gradient in the static experiment; (e) temperature gradient in the dynamic experiment[82].

Furthermore, ultrafast lasers have been employed to investigate the interaction between antiferromagnetic layers and ferromagnetic layers. Optical laser excitation can modulate the exchange bias at their interfaces on a femtosecond timescale, which is significantly shorter than the thermally assisted and spin-orbit-moment modulation achieved using electric pulses. In 2017, Vallobra et al. utilized ultrafast lasers to achieve femtosecond-scale exchange bias modulation in an IrMn/[Co/Pt]_n thin film structure, as shown in Fig. 2.30(a)[82]. They employed different circularly polarized lasers to achieve the AO-HDS of the magnetic layer and alter the exchange bias direction at the antiferromagnetic/ferromagnetic interface (Fig. 2.30(b)(c)). The switching mechanism, as shown in Fig. 2.30(d)(e), involved heating the antiferromagnetic layer to the blocking temperature using the laser, causing it to lose its magnetic order. Subsequently, the laser continued to heat the ferromagnetic layer to the Curie temperature, allowing it to switch according to the circular polarizability of the laser light. Finally, during the cooling-down process, the antiferromagnetic layer determined its magnetic order based on the magnetization in the ferromagnetic layer, completing the switching in exchange bias. The modulation of exchange bias through AO-HDS combines the principles of all-optical switching and annealing. This method offers the advantage of achieving field-free and rapid exchange bias modulation under femtosecond laser excitation, in contrast to the time-consuming process of magnetic field annealing that takes hours. It provides a possibility to have a deeper understanding of the exchange bias.

2.4 Summary

In this chapter, we first reviewed the basic magnetic materials and magnetic data storage. We analyze the potential advantages of antiferromagnet in future magnetic storage and show that the exchange bias effect at the AFM/FM interface can be used to manipulate the antiferromagnetic spin. Then we reviewed the discovery of exchange bias, the evolution of theoretical models, and its applications in spin devices. we begin to introduce the traditional application of exchange bias as a pinning layer and further summarize the different manipulation methods for exchange bias that have been employed in recent years.

Chapter 3.

Experimental Methods

This chapter will concentrate on the fundamental process of spintronic device fabrication, especially the fabrication of MTJ devices. Additionally, it will explore the employment of an ultrafast electrical or optical setup in this study to modulate the exchange bias. Familiarity with these device structures and measurement techniques is crucial for comprehending the experiments and results presented in the following chapters.

3.1 Fabrication process of spintronic devices

3.1.1 Magnetron sputtering

Magnetron sputtering, a technique of Physical Vapor Deposition (PVD) for thin film deposition[83], was invented by Chapin in 1974. The process begins with the generation of plasma by applying a high voltage between a cathode (typically positioned behind the sputtering target) and an anode (usually connected to the chamber as ground). Electrons present in the sputtering gas are accelerated away from the cathode, colliding with nearby sputtering gas atoms. These collisions create electrostatic repulsion, causing the electrons to be collided with the sputtering gas atoms and leading to ionization. The positively charged sputtering gas atoms are then drawn towards the negatively charged cathode, resulting in high-energy collisions with the target surface. Each collision dislodges atoms from the target surface, propelling them into the vacuum environment with sufficient kinetic energy to reach the substrate surface. To increase the deposition rate, sputtering gases are generally chosen from high molecular weight gases like argon (Ar), krypton (Kr), or xenon (Xe) to maximize high-energy collisions. If a reactive sputtering process is desired, gases such as oxygen (O₂) or nitrogen (N₂) can also be introduced into the chamber during film growth. As shown in Fig. 3.1, a notable advantage of sputter deposition is that it does not require melting and evaporation of the target material, making it suitable for materials with high melting points. Sputtered films also exhibit superior adhesion to the substrate compared to vaporized films. Additionally, magnetron sputtering equipment can accommodate multiple targets in its cavity without frequent maintenance, making it ideal for ultra-high vacuum applications. Furthermore, the sputtering can be compatible with reactive gases and enable top to down sputtering, whereas evaporation must be conducted from the bottom.

The production of magnetic disks for HDD was one of the earliest and most significant commercial applications of magnetron sputtering, which remains crucial to this day. Another important application is the preparation of magnetic multilayers for MRAM, which necessitates ultra-high vacuum magnetron sputtering equipment. In this thesis, all magnetic film samples were prepared using magnetron sputtering. Moreover, magnetron sputtering also finds wide-

ranging usage in semiconductor manufacturing, optical coating, photovoltaic solar energy, carbide bit coating, and various other applications.

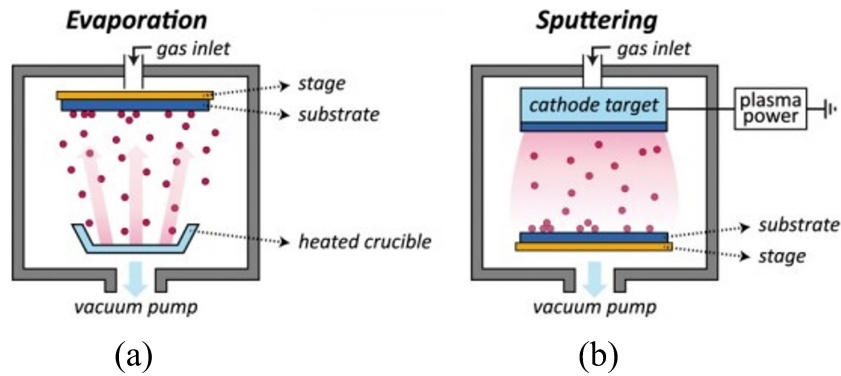


Fig. 3.1 Schematic diagram of (a) thermal evaporation deposition and (b) magnetron sputtering deposition[83].

3.1.2 Photolithography

Lithography, derived from the Greek words for stone (Lithos) and writing (Gráphein), was invented by Aloys Senefelder in 1796. As shown in Fig. 3.2, he discovered that a properly inked and chemically treated Bavarian limestone could be used to transfer an engraved image onto paper. Through the chemical treatment, the image and non-image areas of the stone became oil-absorbent (hydrophobic) and water-absorbent (hydrophilic) respectively. This allowed the image area to attract ink while repelling water, while the non-image area attracted water and repelled ink. In 1950, Jack Kilby from Texas Instruments and Robert Noyce from Fairchild Semiconductor introduced photolithography to the production of integrated circuits. In 1961, Fairchild Semiconductor introduced the first commercially available integrated circuit chip, utilizing the photolithography process to fabricate a significant number of transistors on a silicon wafer[84].

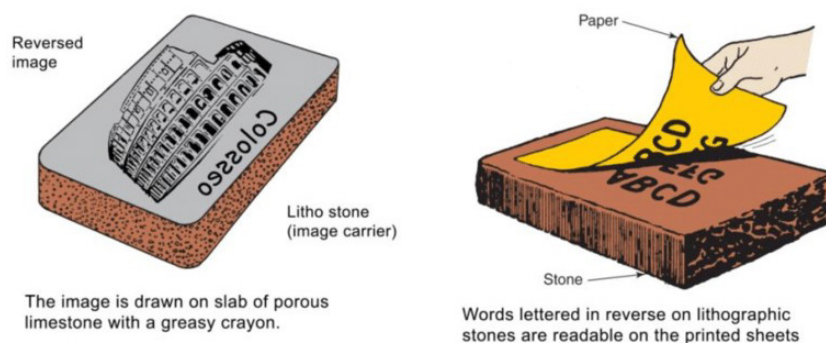


Fig. 3.2 Lithography process invented by Aloys Senefelder[84].

Photolithography is the primary process used in the IC industry for pattern transfer from the photomask to the silicon wafer, enabling the creation of complex multilayer integrated circuits through precise alignment and exposure. Photolithography equipment can be classified into three types: contact exposure, proximity exposure, and projection exposure, with the latter

gaining prominence due to issues with mask contamination and wear in contact exposure, as well as resolution limitations in proximity exposure. As substrate sizes like silicon wafers and LED panels have increased, whole-chip projection exposure has evolved into block repeat exposure (Stepper) and block scanning exposure (Scanner). The optical resolution in projection exposure is determined by the Rayleigh formula, where $CD = k_1/(\lambda/NA)$. To achieve smaller patterns, it is necessary to increase the numerical aperture, decrease the wavelength, and reduce the process difficulty k_1 . High-pressure mercury lamps have been chosen as reliable light sources for their differential spectral lines, such as the G, H, and I line corresponding to the 436 nm, 405 nm, and 365 nm spectral lines of mercury lamps. However, with the need for device miniaturization, deep ultraviolet lithography (DUV) using krypton fluoride (KrF) at 248 nm and argon fluoride (ArF) at 193 nm excimer lasers has been developed and widely adopted. Extreme ultraviolet lithography (EUV) has also emerged, utilizing laser-excited tin droplets to generate extreme ultraviolet light with a wavelength reduced to 13 nm, enabling further device scaling down[85]. Additionally, electron beam lithography (EBL) is often employed for pre-verifying smaller size pattern.

In this thesis, the preparation of MTJ devices involves the fabrication of micrometers and hundreds of nanometer devices primarily using contact exposure or I-line stepper lithography. Sub-hundred-nanometer devices are mainly prepared using DUV lithography and EBL. There are two types of photoresists: positive and negative, as depicted in Fig. 3.3. Positive photoresists become activated after exposure to the light-sensitive components of the photoresist and are subsequently removed during development. Negative photoresists, on the contrary, form a polymer that becomes insoluble in the developer after exposure. The complete photolithography process typically involves (1) spin-coating the photoresist, (2) pre-baking, (3) exposure, (4) post-baking, (5) development, and (6) hard-baking.

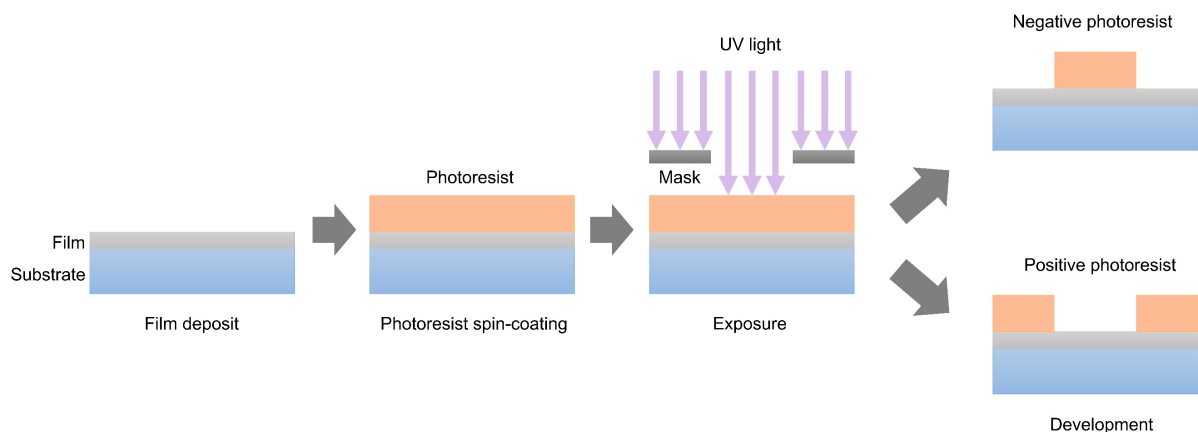


Fig. 3.3 Basic lithography process.

3.1.3 Etching

The etching process, typically carried out after photolithography, involves the use of a corrosive liquid or plasma to remove thin films or materials uncovered by the photoresist. Wet etching has been the predominant method for low-cost integrated circuit fabrication since 1960. However, as device patterns became smaller, its isotropic etching characteristics posed challenges for high-density graphics. Additionally, the surface tension of the liquid hindered the entry of the etching solvent into the pattern groove created by the photoresist, leading to reduced etching efficiency. To address these limitations, dry etching with superior anisotropy has become essential for producing small-sized devices. Fig. 3.4 illustrates the characteristics of anisotropic and isotropic etching. Generally, processes based on chemical reactions exhibit isotropic etching, while those relying on physical bombardment tend to favor anisotropic etching[86].

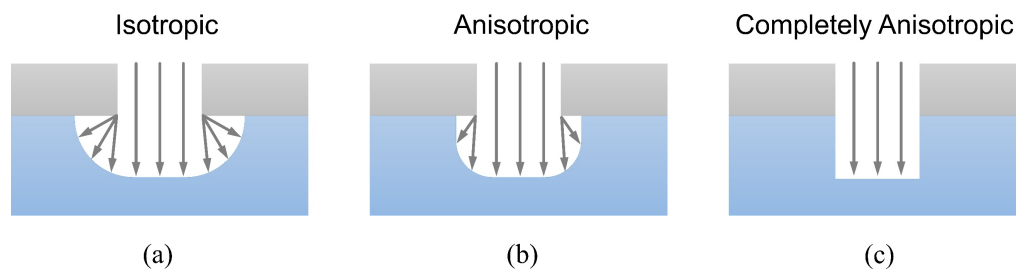


Fig. 3.4 Comparison of anisotropic etching and isotropic etching.

Dry etching typically uses plasma, which is excited by microwaves into charged or electrically neutral reactive particles after the etching gas mixture is passed into the chamber. The plasma reacts chemically or physically to bombard the exposed material to be etched, forming volatile etch products that eventually diffuse into the gas and are pumped out of the chamber by a vacuum pump. In 1974, reactive ion etching (RIE) was first proposed, through the wafer coupled with the parallel plate capacitive, the resulting plasma can obtain a certain direction of motion, to achieve a certain anisotropic etching. To further improve the anisotropy of etching, inductively coupled plasma (ICP) and capacitively coupled plasma (CCP) have further enhanced the efficiency of plasma generation, and at the same time, a bias electrical field can be applied to enhance the anisotropic etching, as shown in Fig. 3.5(a)(b). The main parameters of interest in etching include etch rate, selectivity ratio, depth-to-width ratio, and so on. This type of equipment was originally commercialized by Lam research. In the MTJ fabrication process, ion beam etching (IBE), which can flexibly adjust the etching angle, can better modify the sidewall morphology of cylindrical MTJ devices (Fig. 3.5(c)). Therefore, ICP is usually used as the main etching for MTJ, and then IBE is used to optimize the sidewall morphology.

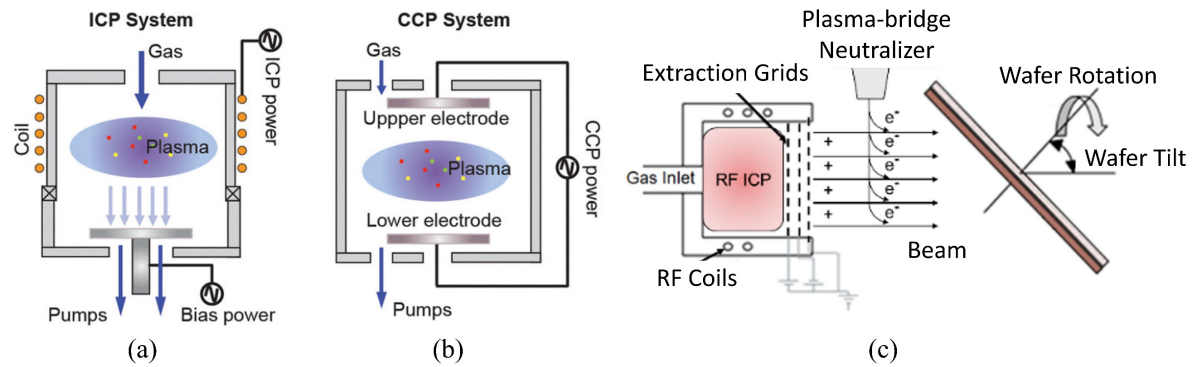


Fig. 3.5 Schematic diagram of the principle of (a) inductively coupled plasma (ICP) etching, (b) capacitively coupled plasma (CCP) etching and (c) ion beam etching (IBE)[86].

3.1.4 Dielectric deposition

Dielectrics are primarily utilized in integrated circuits to provide insulation and isolation for devices and interconnects. The commonly employed materials for this purpose are silicon oxide (SiO) and silicon nitride (SiN), with the deposition technique mainly being chemical vapor deposition (CVD)[87], as shown in Fig.3.6(a). In the front-end-of-line (FEOL) process, addressing the insulation issue of gate leakage is crucial, necessitating the use of a high- k material for the dielectric at the gate. For device sizes ranging from 130nm to 45nm, silicon nitride obtained by nitriding-grown silicon oxide is a widely employed high- k dielectric solution. However, as the gate size continues to decrease, materials with higher k values like hafnium oxide become necessary. Conversely, in the back-end-of-line (BEOL) process, the primary objective is to reduce the RC delay in the transmission line. Therefore, the deposition of low- k dielectrics is required for the BEOL dielectric. Examples of such low- k dielectrics include fluorine-doped silicon oxide, carbon-doped silicon oxide, porous silicon oxide, and other similar materials. To achieve a dense and uniform dielectric layer in the FEOL process, atomic layer deposition (ALD) is commonly employed. On the other hand, the more efficient plasma-enhanced CVD (PECVD) is typically used in the FEOL process, as shown in Fig. 3.6(b). For the fabrication of MTJ devices, which is a back-end process, PECVD is usually utilized to deposit SiN as the dielectric protection. In cases where the spintronic sensors are sensitive to temperature, inductively coupled plasma CVD (ICPCVD) can also be employed for low-temperature dielectric deposition.

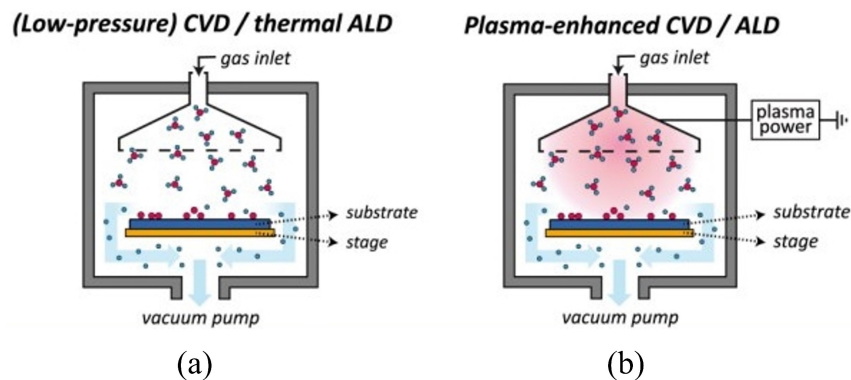


Fig. 3.6 Schematic diagram of (a) chemical vapor deposition (CVD) and (b) plasma-enhanced chemical vapor deposition (PECVD) [87].

3.1.5 Devices fabrication

This thesis focuses on SOT three-terminal MTJ devices, which typically have a top-pinned structure, with the free layer located at the bottom of the film stack and in contacts with the bottom writing electrode. During the MTJ etching process, the advantage of the top pinning structure is that the metal layer below the MgO barrier layer is very thin. This allows for interruption of the etching when a drop in the MgO signal is detected by the endpoint detection equipment, reducing the detrimental effects of sidewall redeposition on MTJ performance loss. However, the utilization of top-pinned MTJ presents a drawback in terms of small etching window and the inability to modify the MTJ sidewall through IBE etching. The specific steps of three-terminal MTJ device fabrication are as follows:

1. The initial step in photolithography involves creating the desired MTJ pattern, which is commonly a circular or elliptical island pattern as depicted in Fig. 3.7. The MTJ exposure demands the highest resolution in the entire fabrication process. There are several widely employed methods for achieving this, including I-line (for patterns > 250 nm), DUV (for patterns > 100 nm), and EBL (for patterns > 10 nm).

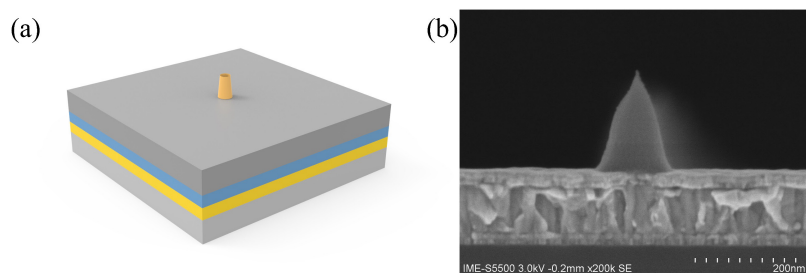


Fig. 3.7 (a) Schematic of MTJ lithography and (b) SEM image.

2. To achieve smaller dimensions for the MTJ, it is usually to deposit a metal hard mask onto the magnetic film stack. This serves two purposes: to precisely transfer the pattern from the photolithography and to correct or shrink dimensions during the etching process, enhancing device performance and integration density. Fig. 3.8 illustrates the appearance of the metal hard mask microstructure after the etching process following lithography.

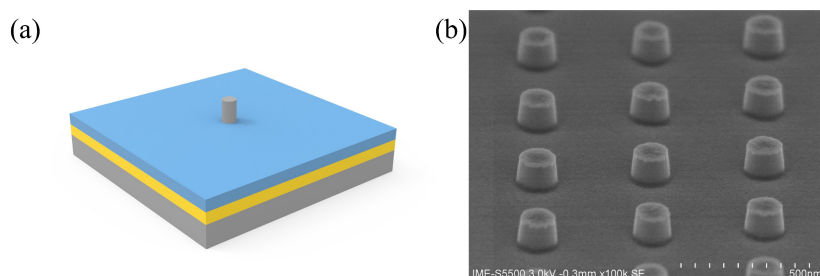


Fig. 3.8 (a) Schematic of MTJ hard mask etching and (b) SEM image.

- The etching process for the MTJ typically involves a sequential layer-by-layer approach to accurately transfer the pattern. Once the metal hard mask etching is completed, equipment like ICP or IBE is commonly used for the MTJ etching. Fig. 3.9 depicts the morphology of the MTJ device after the magnetic layer etching.

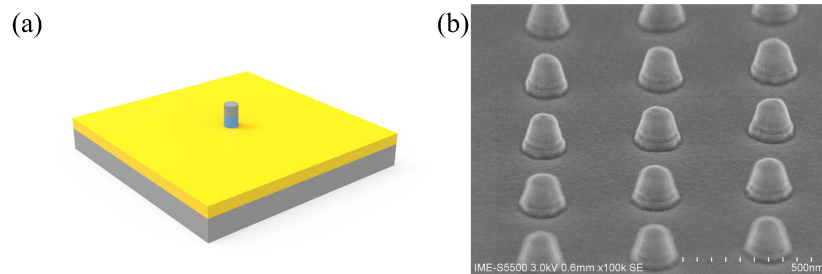


Fig. 3.9 (a) Schematic of MTJ stack etching and (b) SEM image.

- After the MTJ etching, a dielectric protective layer is usually applied. Typically, a 20-50 nm layer of SiN is deposited using methods like PECVD to prevent oxidation and corrosion of the MTJ sidewalls. Fig. 3.10 displays the surface topography after the deposition of SiN.

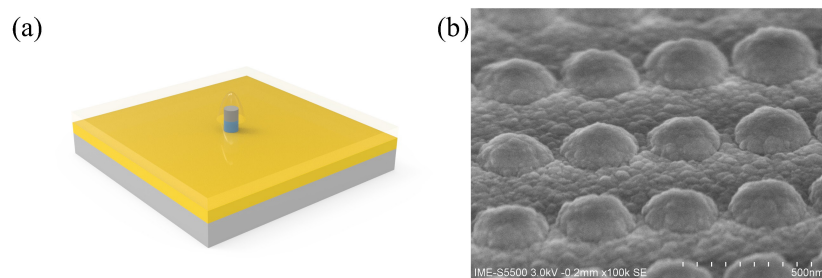


Fig. 3.10 (a) Schematic of SiN dielectric deposition after MTJ etching and (b) SEM image.

- Once the MTJ etch and dielectric deposition are completed, the next step involves patterning the SOT bottom electrode. Fig. 3.11 illustrates the surface morphology of the bottom electrode after etching, where the square pattern represents the structure of the bottom electrode (dummy pattern), and the dot in the center is the covered MTJ structure.

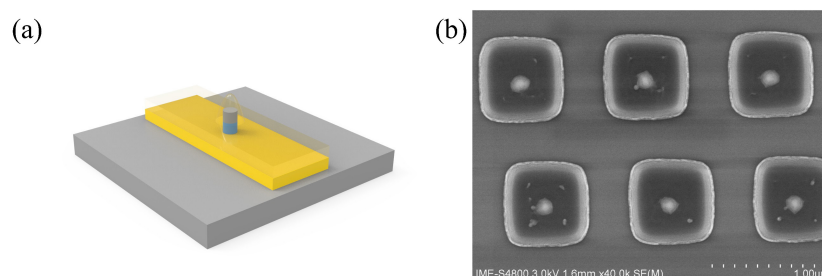


Fig. 3.11 (a) Schematic of SOT bottom electrode etching and (b) SEM image.

- To provide comprehensive protection for both the SOT electrode and MTJ, a SiO₂ dielectric

layer is deposited using PECVD. Fig. 3.12 demonstrates the cross-sectional structure of the SiO₂ dielectric following its deposition.

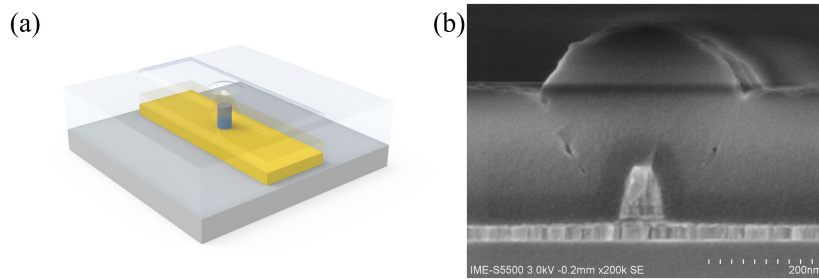


Fig. 3.12 (a) Schematic of SiO₂ media deposition and (b) SEM image.

7. For achieving a flat surface and further interconnection, chemical mechanical polishing (CMP) was applied. Fig. 3.13 showcases the cross-sectional structure after the flattening process and the top SiN dielectric layer is exposed.

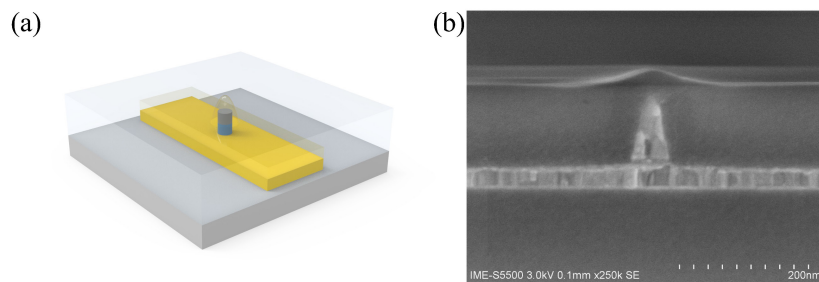


Fig. 3.13 (a) Schematic of CMP flattening and (b) SEM image.

8. The SiO₂/SiN selective etching was utilized to remove the SiN and achieve the MTJ top via self-aligned etching. Fig. 3.14 demonstrates the surface topography after removing the SiN and exposing the MTJ top metal hard mask.

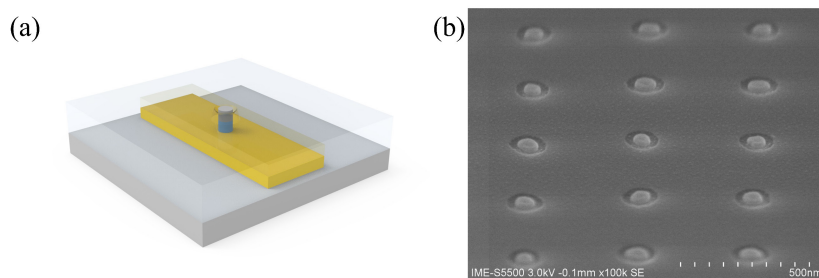


Fig. 3.14 (a) Schematic and (b) SEM image of MTJ hard mask exposed by selective etching.

9. The interconnecting vias of the SOT bottom electrode are accomplished through the lithography of the bottom electrode interconnecting vias, followed by the removal of SiO and SiN using ICP etching. Fig. 3.15 shows the structure and morphology of the bottom electrode interconnect after the etching process.

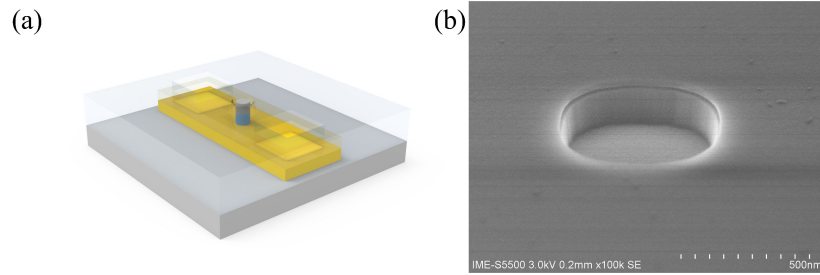


Fig. 3.15 (a) Schematic of bottom electrode through-hole etching and (b) SEM image.

10. For the formation of the top contact electrode, it is common to deposit multilayer metals like Ti/Au or Ti/Al-Cu using evaporation or sputtering. The patterning of the top electrode is typically achieved through lift-off or etching methods. Fig. 3.16 depicts the surface morphology of the top electrode.

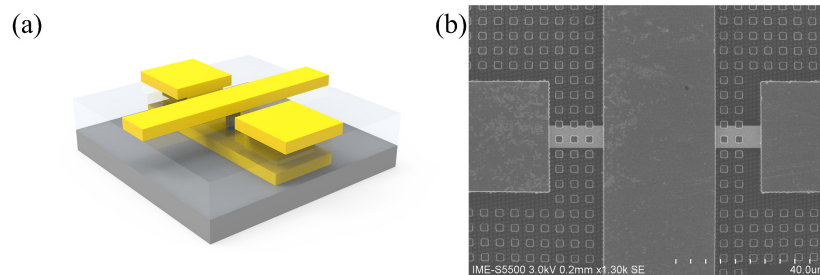


Fig. 3.16 (a) Schematic of top electrode deposition and (b) SEM image.

3.2 Electrical characterization of spintronic devices

3.2.1 DC measurement

The typical measurement setup for spintronic devices consists of a magnetic field system (such as electromagnets or superconducting coils), a movable sample stage, electrical interconnections (like probes or wire bonding), and a source measurement equipment. To ensure test repeatability and convenience, it is common to utilize a control program like LabView to automate the entire system. As an example, let's consider the magnetic probe station. It can be divided into two types: the vertical magnetic field probe station and the in-plane magnetic field probe station, as shown in Fig. 3.17. These divisions cater to the in-plane magnetic anisotropy and perpendicular magnetic anisotropy requirements of spintronic devices, as well as specific tests that necessitate an assisted magnetic field in a particular direction. Connecting the device to the source measure equipment is typically achieved using a precise probe holder and different types of probes. The sample stage usually allows for four-axis XYZR displacement to facilitate the positioning of the target device under a microscope.

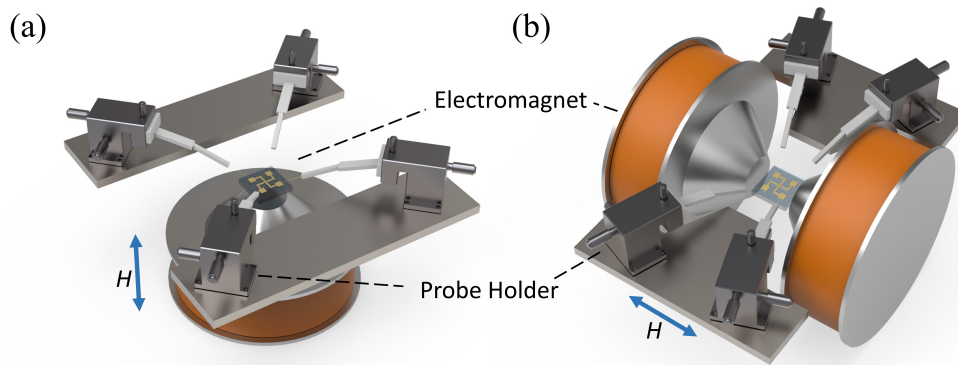


Fig. 3.17 (a) Perpendicular magnetic field probe station. (b) In-plane magnetic field probe station.

DC testing is commonly employed for characterizing various Hall effects, and magnetoresistance of GMR or MTJ devices. Due to the heat generated by the current in DC measurement, it is often to use the short-pulse source or low-temperature chamber for heat-sensitive experiments.

3.2.2 Short-pulse and time-domain measurement

Ultrashort pulses and time-domain measurement using high-speed oscilloscopes are widely utilized in technologies like broadband communications and radar. As highly efficient writing methods such as STT and SOT have evolved in spintronic devices, the writing speed has significantly improved, reaching the sub-nanosecond range. To understand the switching dynamics of spintronic devices, we primarily focus on their time-domain characteristics. Extensive research has been conducted on studying the time-resolved switching dynamics of STT devices, providing valuable insights into the timescale and reliability of the process. This research also serves as a foundation for the measurement of SOT three-terminal devices.

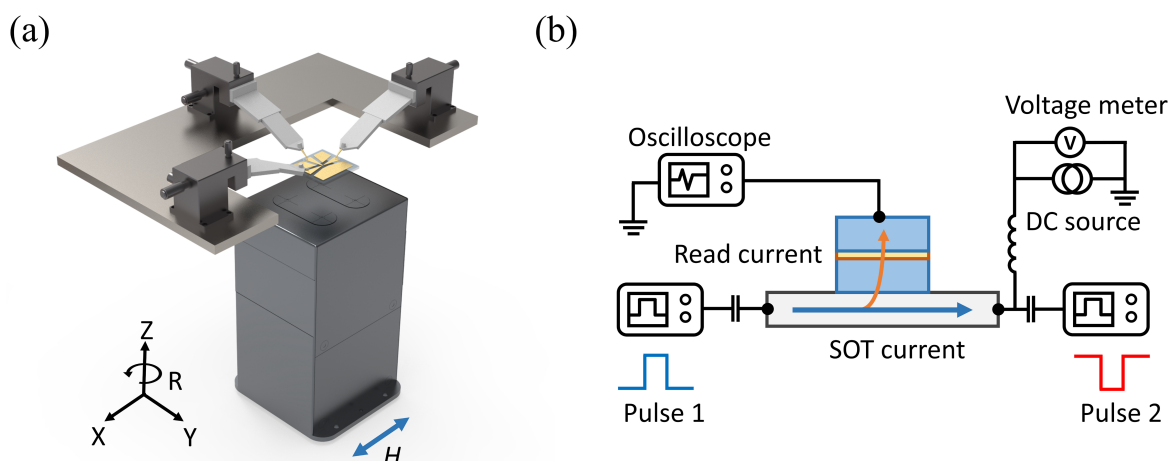


Fig. 3.18 (a) The magnetic field probe station with a U-shaped electromagnet. (b) Schematic diagram of ultrashort pulse and time-domain setup.

The measurement setup is based on the magnetic field probe station, as depicted in Fig. 3.18(a). The U-shaped electromagnet can apply a three-dimensional magnetic field of up to 300 mT to the device, covering the requirements for measuring the MTJ device. Fig. 3.18(b) presents the schematic of the setup, which enables ultrafast write/read operations and captures the time-domain switching dynamics of the devices. To initialize and write the magnetoresistance of the three-terminal MTJ device, the split-pulse technique with positive and negative pulse signals is used to maximize the dynamic range of the measurements and minimize noise in the read current[88]. Additionally, as the device is typically written with a certain degree of randomness, an ordinary pulse generator cannot satisfy the arbitrary editing of positive and negative polarities. Therefore, the system incorporates the Keysight M8190 arbitrary waveform generator, capable of producing ultra-fast pulses with a rising edge of less than 100 ps and a pulse width of 200 ps. It supports two independent output channels. However, the maximum output amplitude of the arbitrary waveform generator is only 1.5 V, which does not meet the requirements of the devices. To address this, a wide bandwidth pulse amplifier is added to each output, amplifying both high-frequency signals above 20 GHz and low-frequency signals around 10 kHz with nearly equal gain. The amplified pulse signal remains undistorted. In the time-domain signal acquisition section, the system employs a Keysight DSOV334 oscilloscope with a bandwidth of 33 GHz, enabling accurate measurement of signal variations on the order of 10 ps. While high bandwidth oscilloscopes are capable of capturing very fast signals, the high noise level hinders precise reading of the magnetoresistance state. Hence, the system incorporates a Keithley 6221 current source and a Keithley 2182 precision voltmeter, connected to the test system via a T-bias connector, to measure the magnetoresistance of the MTJ before and after writing.

3.3 Magneto-optical measurement

The magneto-optical effect refers to the alteration in light intensity or polarization due to the magnetism of a magnetic sample when it interacts with the sample through reflection or transmission. This effect has been instrumental in the early exploration of electromagnetism, confirming the electromagnetic theory of light, as well as classical and quantum theories concerning matter and phenomena like electron spin motion and spin-orbit coupling. In 1845, Michael Faraday discovered that the polarization angle of linearly polarized light rotates when it passes through a magnetic field aligned with the direction of propagation[88]. This breaking experiment unveiled the connection between magnetic fields and light. Furthermore, the magneto-optic Kerr effect (MOKE)[90], which is the magneto-optical effect observed in reflections, has been extensively employed in the detection of material magnetization. MOKE offers a convenient method to measure the magnetic thin film in large samples without physically contacting them, even exceeding the sensitivity of superconducting quantum interferometer devices (SQUID).

3.3.1 Magneto-optic Kerr effect (MOKE)

The magneto-optical Kerr effect pertains to the modification in polarization angle and reflected intensity when a magnetized surface reflects a beam of light. Depending on the magnetization, the incident and reflected light can be categorized into three types: polar, longitudinal, and transversal magneto-optical Kerr effects, as illustrated in Fig. 3.19.

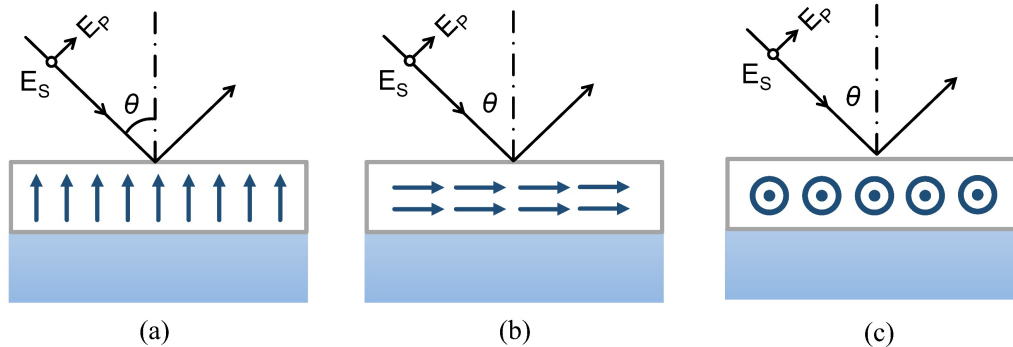


Fig. 3.19 Schematic of (a) polar, (b) longitudinal, (c) transverse magneto-optical Kerr effect.

Fig. 3.20 shows the MOKE setup for measuring the hysteresis loop of a magnetic sample. Initially, laser light is emitted from a light source and passes through a polarizer to become a linear polarized laser. This laser is then modulated by a photoelastic modulator (PEM), whose vibration axis aligns with the optical platform. The magnetized sample reflects the laser light, which subsequently traverses a detector positioned at a 45° angle to the polarizer's transmission direction. Finally, the light enters a photodetector for conversion into an electrical signal. The PEM operates at a frequency of 50 kHz, serving as the reference frequency for the lock-in amplifier. The signal from the photodetector is captured into the lock-in amplifier. By varying the external magnetic field with an electromagnet, we can measure the hysteresis loops of the magnetic sample. When studying ferrimagnetic alloys, we can solely detect the magnetization strength of the magnetic element. The overall magnetization strength is influenced by both the magnetic and rare earth elements. The net magnetization should be measured using a vibrating sample magnetometer (VSM).

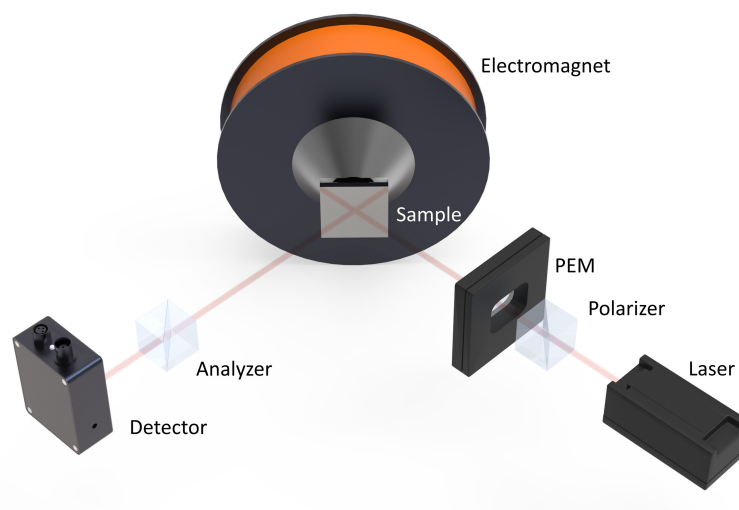


Fig. 3.20 Basic structure of MOKE hysteresis loop measurement setup

3.3.2 All-optical switching and MOKE microscope

To easily observe the magnetization state of magnetic material samples when exposed to the femtosecond laser, we combined the modulated optical path of the femtosecond laser with the optical path of the magneto-optical Kerr microscope. The specific structure of this combination is illustrated in Fig. 3.21. In the all-optical switching experiment, we need to control the laser fluence in order to determine the switching window and explore the dependence characteristics. Additionally, we need to control the number of laser pulses to verify the repeatability of the switching for magnetic samples. This includes observing whether repetitive switching can be achieved and examining the magnetization state after a number of laser pulses. Furthermore, in polarization-related experiments, we need to control the circular polarization state of the laser, either left-rotation or right-rotation. Therefore, we utilize several components in the femtosecond laser modulation. A pulse picker is used to control the number of laser pulses, a half-wave plate is employed to control the laser power, a quarter-wave plate is utilized to control the laser polarization, and finally, a focusing lens is used to concentrate the laser beam.

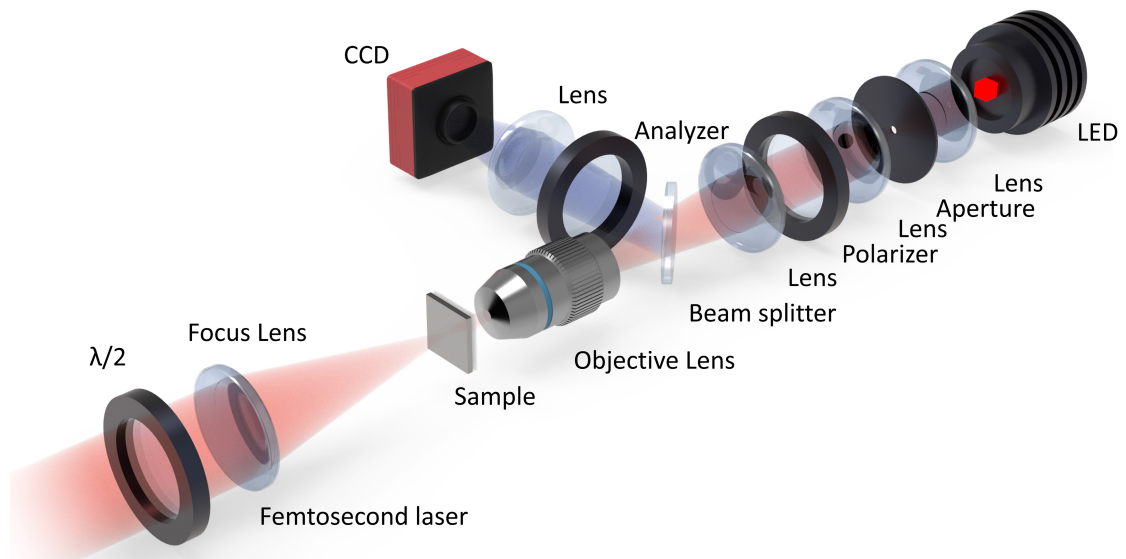


Fig. 3.21 Femtosecond laser-based all-optical switching and MOKE microscopy.

The magneto-optical Kerr microscope utilizes a red LED with a wavelength of 630 nm as the light source. The light passes through a lens set and a diaphragm, which collimates it. It then goes through a polarizer to become linear polarized light. This linear polarized light is subsequently illuminated through the beam splitter and microscope head onto the magnetic sample. When the reflected light from the magnetic sample is observed, it acquires a certain Kerr angle and elliptical polarization depending on the magnetization state of the sample. The reflected light returns through the objective lens passes through the beam splitter again, and then goes through the deflector to reach the CCD camera. To improve the image quality, the polarizer and deflector need close to the vertical polarization direction to prevent light without a Kerr angle entering into the camera. However, the contrast of the original magneto-optical Kerr image obtained by the camera is generally low. To obtain a clearer and sharper image of

the magnetized sample, we usually subtract the images taken before and after the magnetization switching.

For convenient observation of the magnetization state after laser irradiation, we typically use the transmission configuration depicted in Fig. 3.21. This means that the laser irradiation and the MOKE microscope are coaxial but not on the same side. This configuration simplifies the collimation of the optical path and allows for the calculation of laser power and energy. However, it requires the sample substrate to be transparent. In cases where opaque samples need to be tested or when investigating the effect of an applied magnetic field on the all-optical switching, a reflective configuration is used. In this configuration, the laser and the MOKE microscope are situated on opposite sides and axis, resulting in an elliptical irradiated area due to the non-perpendicular incidence of the laser. For exchange-biased samples, the all-optical switching characteristics without a magnetic field are examined using the transmitted configuration, while the switching characteristics in the presence of an external field are studied using the reflected configuration.

3.3.3 Time-resolved MOKE

The conventional process of magnetization dynamics in quasi-equilibrium is relatively slow, as it is limited by the motion of magnetic domain walls and the time it takes for spin-lattice relaxation, which occurs on the nanosecond scale. On the other hand, external excitations generated by femtosecond lasers, such as laser pulses, magnetic field pulses, or current pulses, have much shorter characteristic times compared to spin-lattice relaxation time and precession time. These ultrashort excitations allow us to study the magnetization dynamics under nonequilibrium conditions. To analyze the ultrafast magnetization dynamics in magnetic materials in detail, the commonly used method is the time-resolved magneto-optical Kerr test (TR-MOKE) based on the pump-probe technique. The pump-probe technique, proposed by George Porter in 1950, utilizes the time delay created by the optical range difference between the pump light and the probe light to measure the dynamic process of the sample from non-equilibrium relaxation to equilibrium[91]. Unlike electrical time-domain tests that capture a single response, TR-MOKE requires a highly reproducible dynamic process in the sample under test. Therefore, a constant or pulsed magnetic field is typically applied to reset the sample's magnetization state during the magnetization dynamic measurement.

Fig. 3.22 illustrates the TR-MOKE setup, where a femtosecond laser emitting at a wavelength of 800 nm is used. The laser, which emits continuous pulses at a repetition rate of 5 kHz, is split into two beams using a beam splitter. One beam passes through a mechanical delay line to generate a time difference and stimulate the magnetization dynamics of the non-equilibrium state (referred to as the pump light), while the other beam passes through a β -phase barium borate crystal (BBO) and converts wavelength up to 400 nm for probing the magnetization state (referred to as the probe light). The power of the pump and probe light is controlled using a

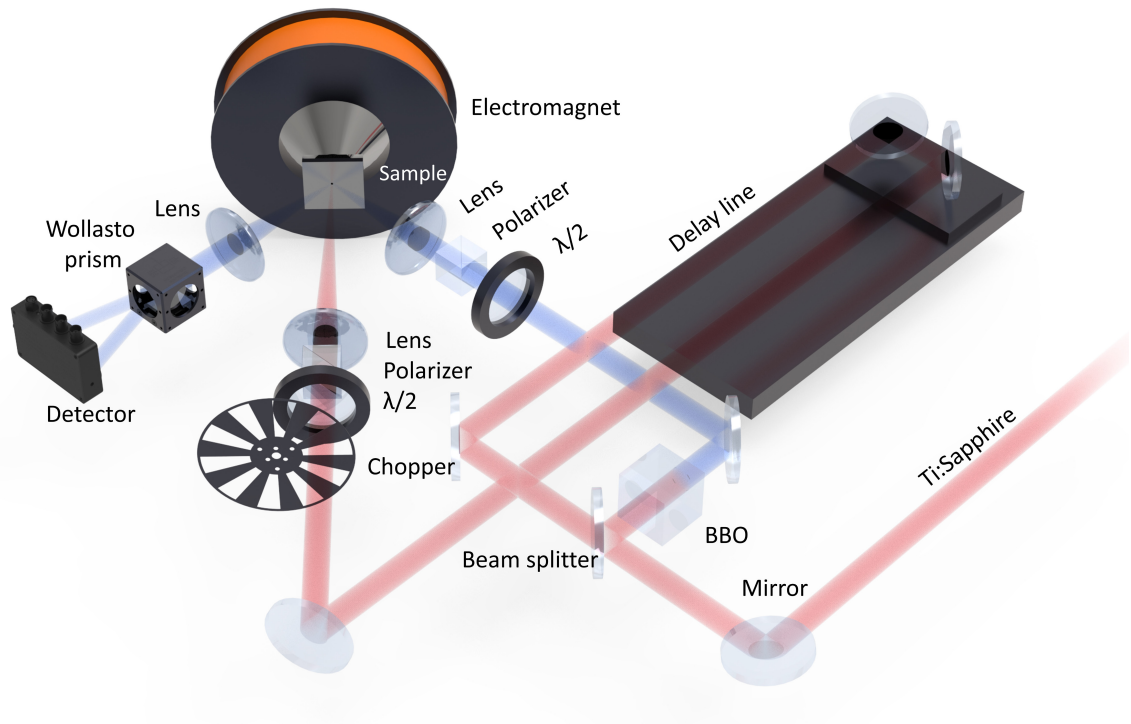


Fig. 3.22 Time-resolved MOKE setup

half-wave wavelength plate and a polarizer. The power of the probe light is determined by the linear response window of the balanced photodiode, while the power of the pump light varies depending on the sample being observed. Both beams of light are directed to the sample through a focusing lens, with the pump spot being approximately 10 times larger than the probe spot. This ensures that the area detected by the probe light is within the relatively uniform irradiation range of the pump light. The detection light, after being reflected by the sample, is collimated by a lens and split by a Wollaston prism onto a balanced photodiode. The Wollaston prism divides the detection light into two beams with orthogonal bias directions, and the half-wave plate is adjusted to balance the signal on the photodiode. The signals from the two diodes are then subtracted to obtain the output. If the half-wave plate is correctly set, the signal difference should only be noise when the magnetic sample does not cause a Kerr turn. However, if a Kerr corner is present in the detected light, there will be a change in the relative intensity of the balanced photodiode signal, indicating a valid Kerr corner signal. However, these signals are typically small in practical tests, and signal modulation and lock-in amplifiers are employed to increase the signal-to-noise ratio. Modulation can be performed on various laser characteristics, such as polarization, frequency, phase, spatial distribution, and intensity. In the case of TR-MOKE, intensity modulation of the laser is achieved using a chopper. By periodically truncating the pump light, the balanced photodiode signal oscillates at the frequency of the chopper between zero and the measured signal (proportional to the Kerr angle). The output signal is obtained by extracting the first harmonic using a lock-in amplifier.

During the test, the hysteresis loop in the quasi-equilibrium magnetization state is first measured without the presence of pump light by setting the chopper in the probe light path.

Additionally, hysteresis loops at different delay time points can be obtained with pump light excitation. However, to accurately measure the magnetization dynamics, a chopper is usually used to block the pump light. This ensures that the change in the magnetization intensity signal detected by the balanced photodiode is not affected by pump light interference or a decrease in magnetization intensity. To eliminate signals that are not related to magnetization dynamics, such as thermal perturbations, it is common to perform two measurements with opposite magnetization directions and calculate the difference between them.

3.4 Summary

In this chapter, we present a comprehensive overview of the fabrication process of the three-terminal MTJ devices. We cover topics such as film growth, patterning techniques, and characterization methods. Additionally, we discuss the electrical DC and ultra-short pulse time-domain measurement of MTJ devices. Lastly, we delve into the fundamental magneto-optical test methods and provide an in-depth explanation of the ultrafast magnetic measurement platform that utilizes femtosecond lasers.

Chapter 4.

Double Exchange Bias Magnetic Tunneling Junction (MTJ)

In this chapter, we design and optimize the double exchange bias MTJ stack, which is the precondition of the exchange bias manipulation. First, we introduce the structure of the double exchange biased MTJ stack and the function of each layer in detail. Then, we focus on the static magnetic properties and structure optimization of the AFM/FM storage layer. The design objective of the storage layer and the driven layer is to obtain sufficient exchange bias field and writing efficiency. We study the IrMn thickness, seed layer thickness and insert layer thickness dependence. Finally, we demonstrate the blocking temperature of the exchange-biased storage layer and find the optimal annealing condition for the full stacks.

4.1 Double exchange biased MTJ stack design

The double exchange biased spin-valve structures can be easily found in MRAMs and spintronic sensors. In the TA-MRAM shown in Fig. 4.1(a), both the storage layer and reference layer are pinned by an antiferromagnetic layer[68]. However, due to the thermally assisted writing procedure, the blocking temperature of the pinning antiferromagnetic layer must be higher than the storage layer, which is achieved through antiferromagnetic materials and thickness engineering. This allows for maintaining the stability of the reference layer and facilitates modification of the storage ferromagnetic layer and exchange bias field. In spintronic sensors, it is typically necessary to align the easy magnetization axis of the sensing layer

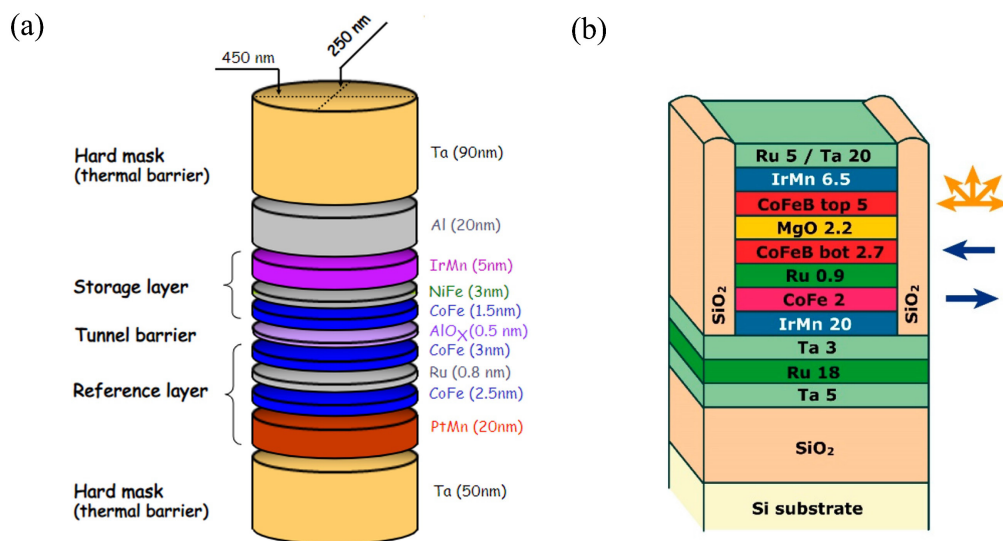


Fig. 4.1 (a) Double exchange bias structure for thermally assisted magnetic random memory[68]. (b) Double pinned TMR sensor[92].

orthogonal to the reference layer to obtain a linear magnetoresistive response to the external field[92]. The double-pinned structure shown in Fig. 4.1(b), this structure employs antiferromagnetic layers with different blocking temperatures to fix the sensing layer and the reference layer separately, which is achieved by annealing the device with two different temperatures and applying an orthogonal external field. As a result, with the advancements in SOT-MRAM technology and the discovery of SOT for manipulating antiferromagnetic exchange bias, combining in-plane SOT-MRAM with antiferromagnetic exchange bias can address the issues of device scaling down in in-plane SOT-MRAM and the field-free switching issue in perpendicular SOT-MRAM. Additionally, this combination can also utilize the unidirectional anisotropy of the exchange bias to achieve high thermal stability and resistance to external magnetic field interference.

Unlike TA-MRAM and double-pinned TMR sensors, the material selection and structural design of the SOT bottom electrode need to be considered to achieve high spin efficiency and sufficiently exchange bias field, simultaneously. In a SOT-MRAM, the SOT-driven electrode and the storage layer need to be placed at the bottom of the MTJ for writing. Therefore, the first step is to create a top-pinned double exchange biased MTJ stack structure with in-plane magnetic anisotropy. As depicted in Fig. 4.2(a), the detailed structure of the film stack is as follows: Sub./Ta (1.0)/Pt (8.0)/Ir₂₀Mn₈₀ (6.0)/Co₂₀Fe₆₀B₂₀ (1.9)/MgO (1.1)/Co₂₀Fe₆₀B₂₀ (2.4)/Ru (0.8)/CoFe₃₀ (2.0)/Ir₂₀Mn₈₀ (7.5)/Ru (2.0)/Ta (3.0)/Ru (10.0) (nm). The film stack

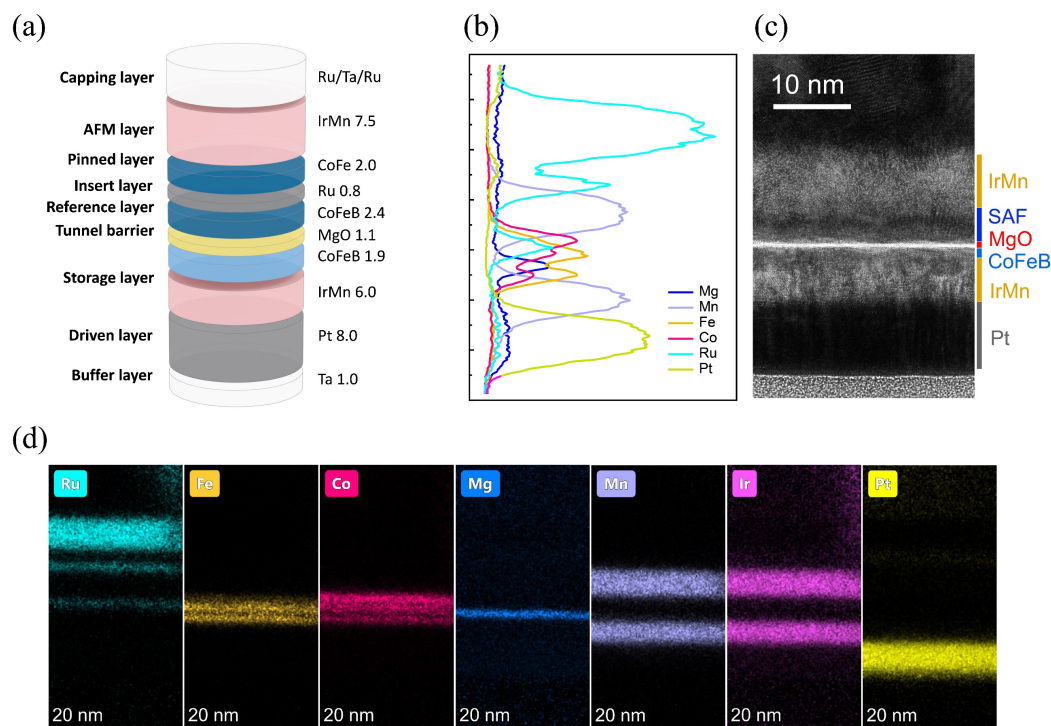


Fig. 4.2 (a) Top-pinned double exchange biased stack structure. (b) Individual-element EDX maps for the stacks. (c) The TEM image of the stack. (d) The transmission electron microscopy image of the details of the film stack, IrMn layer and Pt bottom electrode.

consists of the buffer layer, seed layer, antiferromagnet/ferromagnet storage layer, tunnel barrier, reference layer with synthetic antiferromagnetic structure, antiferromagnetic pinning layer, and the capping layer, in that order from the bottom to the top. TEM images and X-ray energy dispersion spectra (EDX) and elemental distributions of the stack are shown in Fig. 4.2(b-d).

The materials for the buffer layer near the substrate are typically Ta, as the Ta can improve the flatness and quality of the grown layers[93]. Commonly, when verifying a designed MTJ stack, it is usually to grow a thicker buffer layer at the bottom. The thicker buffer layer helps eliminate the influence of different substrates and allows for non-destructive measurements, such as current in plane tunneling (CIPT), to obtain parameters like TMR and RA. This facilitates iterative and efficient optimization.

The seed layer for the antiferromagnetic layer, like IrMn and PtMn, is usually selected from metals such as Cu, Pt, Ru, NiFe, CoFe, and NiFeCr. These metals provide (111) crystalline texture for IrMn and PtMn. Later, we will discuss the impact of seed layer thickness on the exchange bias.

The storage layer consists of a coupled antiferromagnetic IrMn and a ferromagnetic layer CoFeB. The Ir₂₀Mn₈₀ can generate a large exchange bias field even at a thin thickness (~4 nm), making it suitable for further manipulation. The CoFeB ferromagnetic layer is pinned by IrMn and builds a "sandwich" MTJ structure of CoFeB/MgO/CoFeB, which can use the TMR effect to indirectly read the antiferromagnetic state.

The reference layer, CoFeB, and the pinned layer, CoFe, are antiferromagnetic coupled through a spacer layer of metals like Ru and Ir. Such kind of synthetic antiferromagnetic structure provide enhanced stability of the reference layer and minimizes the influence of stray fields on the free layer.

The antiferromagnetic pinned layer needs to provide a stronger exchange bias and higher blocking temperature. It is usually made thicker Ir₂₀Mn₈₀ (>7 nm) or PtMn (>15 nm). Above the antiferromagnetic pinned layer is the capping layer, typically made of Pt, Ru, Ta, etc. The capping layer induces a better crystalline structure in the antiferromagnetic layer during annealing and protects against oxidation and corrosion.

By using a transverse MOKE, the stepped hysteresis loop can be obtained, as shown in Fig. 4.3. Specifically, the middle part of the loop represents the ferromagnetic storage layer CoFeB, the top loop represents the reference layer CoFeB, and the bottom loop represents the pinned layer CoFe. From the inset of Fig. 4.3, the minor loop of the ferromagnetic storage layer CoFeB is fully shifted to the left side of the magnetic field axis with the bottom pinned IrMn. Furthermore, the thicker IrMn at the top induces a stronger exchange bias with CoFe. The reference layer CoFeB is antiferromagnetic coupled with the pinned layer CoFe through Ru spacer, causing the right shift of the minor loop.

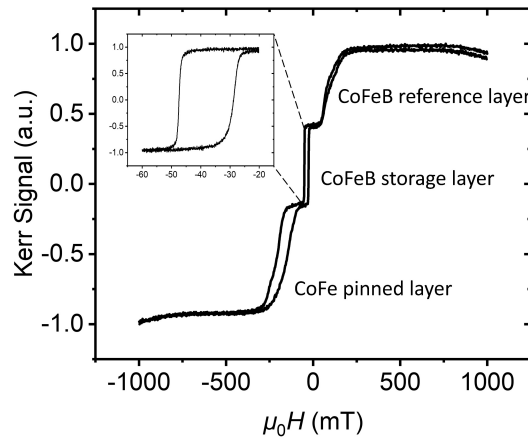


Fig. 4.3 MOKE hysteresis loop of top-pinned double exchange bias MTJ stack.

4.2 Antiferromagnetic layer thickness dependence

The exchange bias is affected by several factors, not only the materials and thickness for the ferromagnetic layers, antiferromagnetic layers, and seed layers, but also the annealing conditions (temperature and field). The pinning layer only requires high stability and a strong exchange bias. The storage layer involves meeting the basic requirement that the exchange bias field is larger than the coercivity and requires more flexible manipulation while finding a balance between the efficiency of data writing and the stability of data storage.

To study the antiferromagnet thickness on the exchange bias field and coercivity, we prepared a structure with a Sub./Ta (1.0)/Ru (2.0)/IrMn (t_{IrMn})/CoFeB (1.6)/MgO (1.6)/Ta (3.0)/Ru (2.0) (nm) as shown in Fig. 4.4(a). The IrMn antiferromagnetic layer was a wedge with a thickness ranging from 2 to 8 nm. By analyzing the MOKE hysteresis loops (Fig. 4.4(b)) and the variation of the exchange bias field and coercivity (Fig. 4.4(c)) with different IrMn thicknesses, we observed that the exchange bias increases rapidly beyond 2.5 nm and approaches maximum at 4 nm. The coercive field shows a clear peak near the thickness of ~ 3 nm, where the exchange

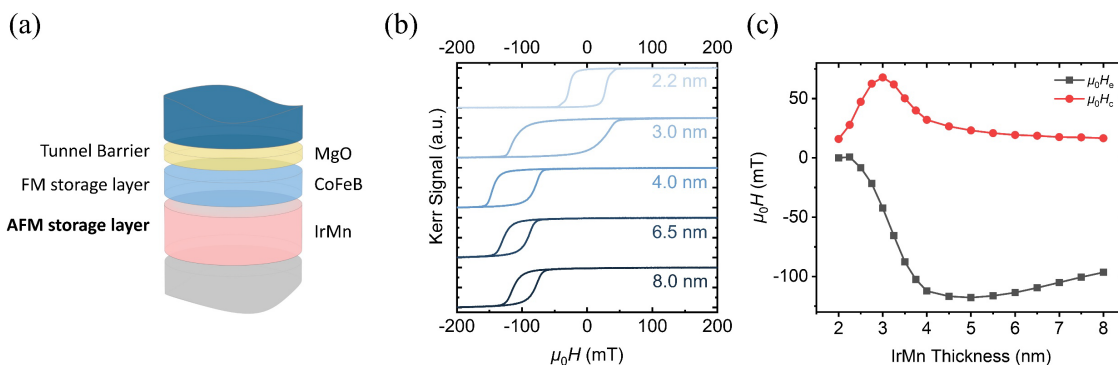


Fig. 4.4 (a) Exchange-biased bilayer structure with a wedge AFM layer. (b) Hysteresis loops for various IrMn layer thicknesses (c) The exchange bias field $\mu_0 H_e$ increases with the thickness of the IrMn, and the coercivity $\mu_0 H_c$ have a peak when exchange bias begins to increase.

bias starts to appear and rapidly increases. The requirement of the exchange bias field is larger than the coercivity is satisfied when IrMn thickness is larger than 3.5 nm.

In Chapter 2, we discussed the fundamental phenomenon and theoretical development of exchange bias. Meiklejohn and Bean proposed a macrospin model, suggesting that the exchange bias field is inversely proportional to the thickness of the ferromagnetic layer[48]. Mauri[54] and Malozemoff[55] addressed the issue of the exchange bias theoretical calculations is much larger than the experiment, focusing on the antiferromagnetic domain wall and the random field induced by interface roughness and defects, respectively. However, they did not further explain the variation of the exchange bias field and coercivity with antiferromagnet thickness and temperature.

In 2002, Nowak et al. proposed the magnetic domain state model, which extensively investigated the antiferromagnet thickness and temperature dependence[94][95]. They employed the Monte Carlo method to analyze the exchange bias system with a finite temperature. Their model considered structural defects induced pinned spin randomly distributed in the antiferromagnetic interface. When the antiferromagnetic layer is below the critical thickness, the magnetization state of the antiferromagnetic domains can rotate with the ferromagnetic layer. As the antiferromagnet thickness over the critical thickness, these domains become stable rapidly, resulting in exchange bias. When the antiferromagnet thickness continues to increase and surpasses the maximum domain wall thickness of the antiferromagnet, the exchange bias gradually saturates. The increase in the coercivity is attributed to the rotatable interfacial antiferromagnetic spins, mainly influenced by the antiferromagnetic uniaxial anisotropy, and transferred to the ferromagnetic layer through interfacial exchange coupling. The peak in the coercive field can be explained by the gradual enhancement of the antiferromagnetic uniaxial anisotropy with increasing thickness.

4.3 IrMn seed layer thickness dependence

IrMn is a sheet antiferromagnet with a disordered fcc phase[96]. To achieve a high unidirectional anisotropy constant K_{AF} , an ordered $L1_2$ -IrMn structure is necessary, with an Ir concentration typically ranging from 22 to 32%. The (111) crystalline texture of IrMn parallel to the interface is also required to obtain a large exchange bias. Pakala et al. experimentally demonstrated the importance of a crystalline texture of IrMn in obtaining a strong exchange bias field in both top-pinned and bottom-pinned spin valves[97]. Therefore, careful selection and thickness control of the seed layer of IrMn is critical during deposition. Commonly used seed layer materials, such as Pt, Ru, Cu, NiFe, NiCr, and NiFeCr, have similar lattice constants with IrMn and provide the (111) texture. For more flexibility in choosing the bottom electrode materials, the ultrathin was isolated and the seed layer was investigated. The stack of Sub./Ta (5.0)/ Ru (0.1-0.9)/IrMn (5)/CoFe (2.0)/Ru (2.0) (nm) and Sub./Ta (5.0)/ Pt (0.1-0.9)/IrMn (5)/CoFeB (1.6)/ MgO (1.6)/Ta (3.0)/Ru (2.0) (nm) structure was prepared, as shown in Fig. 4.5(a). In Fig. 4.5(b), it can be observed that the exchange bias field increases slowly when the seed layer is smaller than 0.5 nm, where the exchange bias mostly comes from interface

roughness and defects. Additionally, the initial exchange bias of the Ru sample is due to the crystalline CoFe can improve the crystallization of IrMn at the interface compared with amorphous CoFeB. When the seed layer exceeds 0.7 nm, the exchange bias field increases rapidly, and a fully shifted hysteresis loop can be achieved when the seed layer is close to 1 nm. The peak of the exchange bias field (Fig. 4.5 (b)) and coercive field (Fig. 4.5 (c)) represents the transition of IrMn from amorphous to polycrystalline.

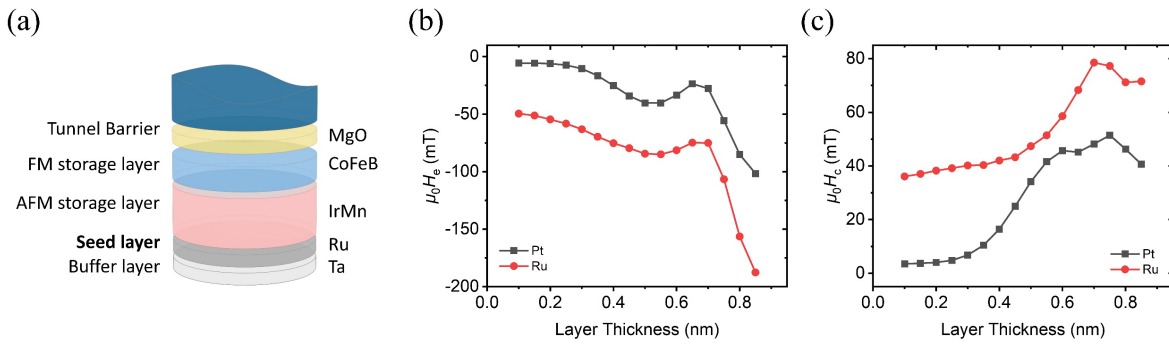


Fig. 4.5 (a) Structure of an exchange bias bilayer with an ultrathin seed layer. Exchange bias $\mu_0 H_e$ (b) and coercivity $\mu_0 H_c$ (c) with the increases thickness of the Pt and Ru seed layer.

4.4 Insert layer thickness dependence

The interfacial exchange bias can be significantly affected by an insert layer. This also can prevent the diffusion of interfacial elements at high temperatures, allowing for the desired exchange bias field. Ali et al. studied the dusting insert layer with different materials on exchange exchange-coupled interface in a spin valve[98]. When the dust layer consists of non-magnetic metals like Au, Pt, Ta, and Cu, and exceeds 0.1 nm, a significant decrease in the exchange bias can be observed. On the other hand, when the insert layer is a magnetic metal like Fe, Ni, or NiFe, the exchange bias initially increases and then decreases. Interestingly, when the rare-earth metal Gd is used, the exchange bias decreases abruptly to zero after the dust layer is inserted at over 0.5 nm. Based on the structure shown in Fig. 4.6(a) with Sub./Ta (1.0)/Ru

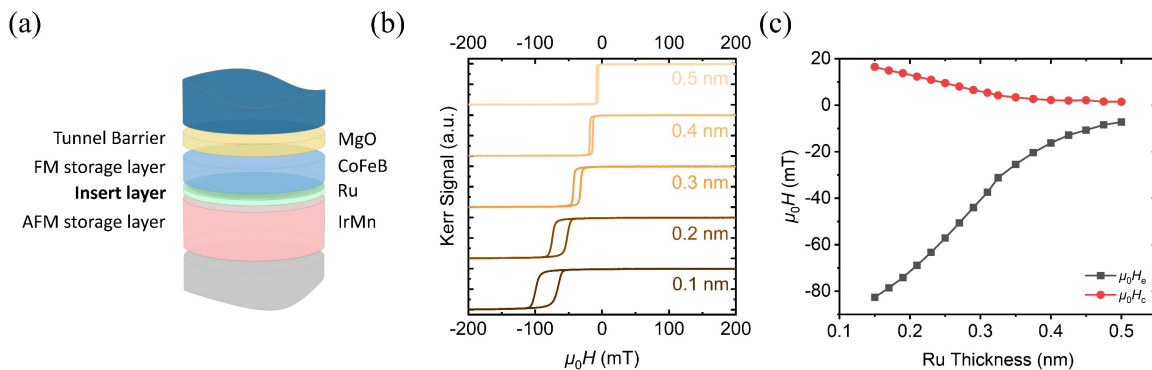


Fig. 4.6 (a) Structure of exchange-biased bilayer with a dusting insert layer. (b) Hysteresis loops for various dusting layer thicknesses. (c) Exchange bias $\mu_0 H_e$ and coercivity $\mu_0 H_c$ decreases with increasing thickness of the dusting layer.

(2.0)/IrMn (5.0)/Ru (0.1-0.5)/CoFe (2.0)/Ru (2.0) (nm), a wedge Ru layer of 0.1 to 0.5 nm was inserted at the IrMn/CoFeB interface. After annealing for 1 hour at 300 °C with a 1 T external field, hysteresis loops were observed, as shown in Fig. 4.6(b). It can be observed that the exchange bias and coercivity decrease rapidly with increasing thickness of the Ru dusting layer. In a range of 0.1 to 0.5nm of Ru dusting layer, the exchange bias field is larger than the coercive field. Additionally, to achieve a larger exchange bias, the (111) crystalline texture at the interface of IrMn and CoFeB is needed. Simultaneously, a well-defined (001) crystalline texture of CoFeB/MgO/CoFeB is required to obtain high TMR. Therefore, a balance needs to be struck between the exchange bias field and TMR during the design of the stack.

4.5 The temperature dependence of exchange bias

The exchange bias is highly temperature-dependent, and the exchange bias field will reduce to zero when reaches the blocking temperature. To determine the blocking temperature of the storage layer in our MTJ stacks, we measure the hysteresis loops with rising temperature. The results are presented in Fig. 4.7(a). As the temperature increases to 520 K, the exchange bias field of the IrMn/CoFeB storage layer gradually decreases to zero. At 500 K, the exchange bias field decreases to 1.5 mT, indicating a blocking temperature of approximately 500 K. The exchange bias field of the pinned layer minor loops also reduced to zero around 500 K. Therefore, it is necessary to replace the pinning layer with an antiferromagnet like PtMn, which has a higher blocking temperature. Fig. 4.7(b) illustrates the exchange bias and coercivity with increasing temperature. It can be observed that the coercivity shows a similar peak when close to the blocking temperature. In the grains model proposed by Stiles and McMichael[99], two factors contribute to the coercivity in an exchange bias system: one due to inhomogeneous reversal and the other to irreversible transitions in the antiferromagnetic grains. The increase in coercivity near or even above the antiferromagnetic blocking temperature primarily arises from the unstable rotations due to hysteresis losses in the antiferromagnetic grains. This also suggests that the exchange coupling between antiferromagnet and ferromagnet still exists at high temperatures.

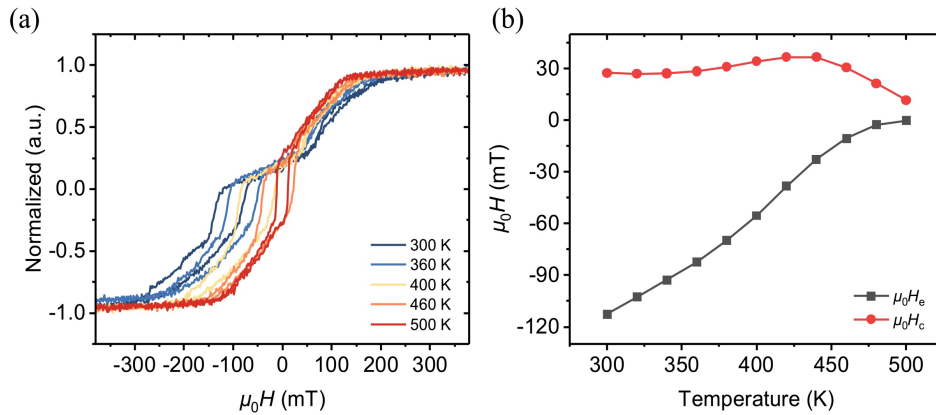


Fig. 4.7 The hysteresis loops at (a) rising temperatures (b) the exchange bias $\mu_0 H_e$ decreases to zero around 500 K, while the coercivity $\mu_0 H_c$ increase close to blocking temperature.

4.6 The field annealing optimization

The field annealing is crucial for achieving an ideal exchange bias field and high TMR in our double exchange bias MTJ stack[100]. We are using annealing temperatures at 270°C, 300°C, and 350°C for 1 hour in a 1 T external field. The hysteresis loops after annealing are depicted in Fig. 4.8(a-c). In Fig. 4.8(d)(e), it can be observed that the exchange bias of the pinned layer reaches its maximum at 300°C, while the exchange bias field of the bottom storage layer gradually increases with the annealing temperature and reaches its maximum at 350°C. Additionally, the exchange bias of the storage layer satisfies the requirement of being larger than the coercivity at all annealing temperatures. The difference in the trend of the top and bottom exchange bias field with temperature can be explained by several possibilities. One is that the exchange bias at the top and bottom interfaces of IrMn is influenced by the different deposition conditions. Another possibility is the elemental diffusion difference during the heat treatment of the top and bottom interfaces.

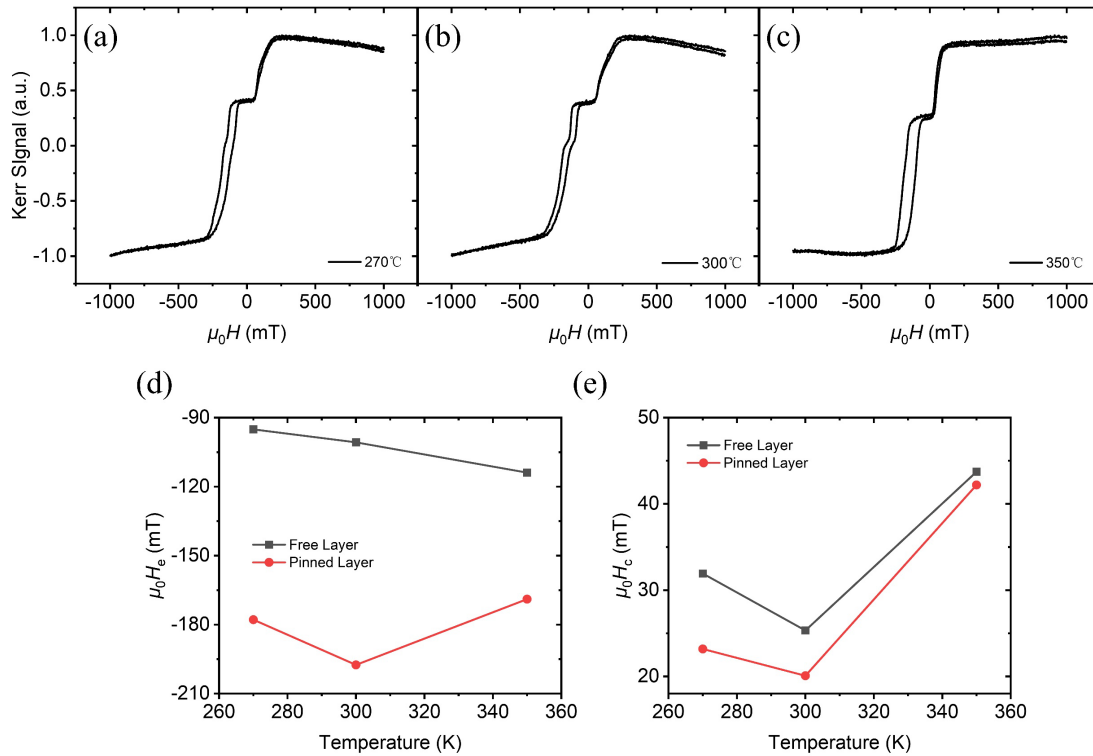


Fig. 4.8 The hysteresis loops after magnetic field annealing at (a) 270°C, (b) 300°C (c), 350°C. (d) (e) Exchange bias field and coercivity at various annealing temperatures.

4.7 Summary

This chapter focused on double exchange bias MTJ stack design and optimization. In order to achieve efficient driven layer and flexible exchange bias manipulation, the exchange bias field and coercivity of the AFM/FM storage layer are controlled by antiferromagnetic layer thickness, seed layer thickness, insertion layer thickness, and annealing temperature. Through the ultrathin seed layer, it provides great convenience for our device design of the driven electrode, not only the HM/AFM structure can be used, but also the AFM itself can be directly used as the driven electrode without too much shunt by the seed layer when applying the writing current. Based on the above results, we have essentially achieved the fundamental performance of the top-pinned double exchange bias MTJ stack, which involves the realization of the exchange bias field larger than the coercivity of the AFM/FM storage layer and a stable reference structure.

Chapter 5.

Electrical Manipulation of Exchange Bias

In this chapter, we demonstrate the electrical exchange bias manipulation and detection of antiferromagnetic order in three-terminal MTJ devices. The antiferromagnetism has been indirectly detected through a coupled CoFeB ferromagnetic layer by the TMR. We then realize the field-free switching of the antiferromagnet with current pulses down to 0.8 ns by injecting currents into the bottom electrode. The sub-nanosecond switching results, together with macrospin modeling, indicate a SOT-induced switching mechanism. Furthermore, our proposed exchange-biased MRAM, whose data bit is stored in the antiferromagnets rather than ferromagnets, provides a magnetic field-free and scalable scheme for a new type of memory.

5.1 Field-free switching of exchange bias

Fig. 5.1(a) shows the schematic of the MTJ devices. The film stacks are composed of SiO Sub./Ta (1.0)/Pt (8.0)/Ir₂₀Mn₈₀ (6.0)/W (0.1)/Co₂₀Fe₆₀B₂₀ (1.9)/MgO (1.1)/Co₂₀Fe₆₀B₂₀ (2.4)/Ru (0.8)/CoFe₃₀ (2.0)/Ir₂₀Mn₈₀ (7.5)/Ru (2.0)/Ta (3.0)/Ru (10.0) (nm). Two antiferromagnetic IrMn layers were used to fix the CoFeB ferromagnetic layer and the synthetic antiferromagnet structure CoFeB/Ru/CoFe, respectively. Electrical currents were injected into the bottom electrode Pt to switch the IrMn/CoFeB storage layer. In our work, we focus on the manipulation and detection of the bottom IrMn layer and the magnetic state of the top IrMn layer remains unchanged during the writing process. Unless specified, we shall abbreviate bottom IrMn to IrMn hereafter.

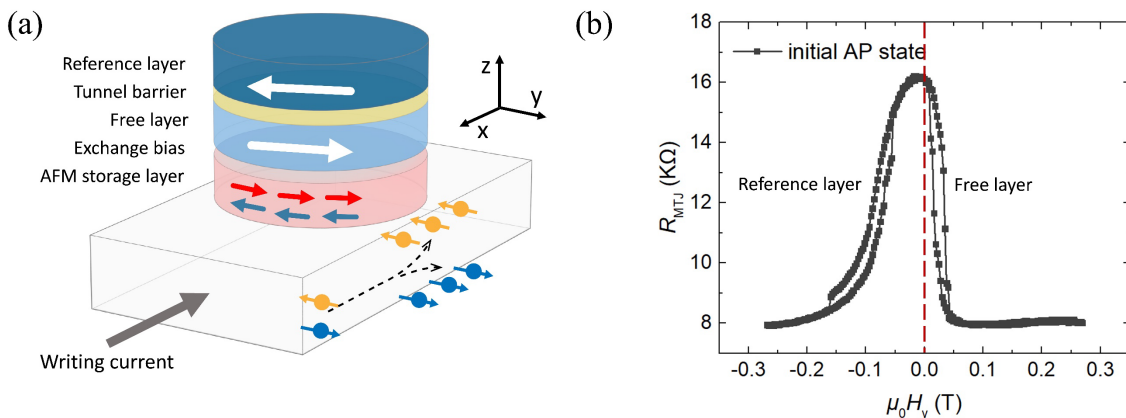


Fig. 5.1 (a) Schematic of the three-terminal MTJ. The bottom IrMn is electrically manipulated by the current injected into the writing channel and detected by the MTJ. (b) The magnetoresistance curve of the double exchange bias MTJ devices.

The deposited stacks were annealed at 300°C for one hour in an external field of 1 T along the $-y$ direction. Then, the field-cooling procedure was performed from 300°C to room temperature at the same field. After the field-cooling, the stacks were then patterned into

circular nanopillars with diameters D range from 40 to 200 nm on the Pt bottom electrode. The top electrode was used for the MTJ readout. Fig. 5.1(b) shows the magnetoresistance loop of a device with $D = 150$ nm when sweeping magnetic fields along the y direction. Because $\mu_0 H_e > \mu_0 H_c$ can still be satisfied, the hysteresis loops of the CoFeB storage layer and CoFeB pinned layer are fully biased to the $+y$ and $-y$ axes, respectively. We observed no training effect of the exchange bias in the patterned devices, indicating a low intermixing at the IrMn/CoFeB interface and thus good stability of our devices.

As shown in Fig. 5.2(a), we define the state of the bottom IrMn layer as n^- after annealing. Because the exchange bias fields (52.5 mT and 201.3 mT) are stronger than the coercive fields $\mu_0 H_c$ (10.3 mT and 31.6 mT) at both interfaces, the magnetization of the CoFeB storage layer and CoFe pinned layer are both initialized along the $-y$ direction. The CoFeB reference layer subsequently points along the $+y$ direction due to its antiferromagnetic coupling to the CoFe layer via Ru. Therefore, our MTJ stacks present an antiparallel (AP) configuration after annealing, which corresponds to the n^- state.

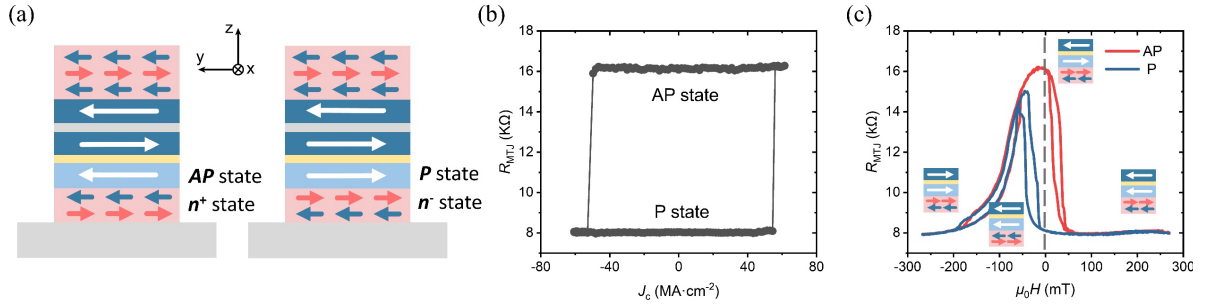


Fig. 5.2 (a) Schematic of the two states of the bottom IrMn layer, i.e., n^- and n^+ states, which corresponds to the AP and P MTJ states, respectively. (b) The current-induced magnetoresistance state switching. (c) Magnetoresistance curves measured when the bottom IrMn layer is at the n^- or n^+ state.

We then realized field-free switching of the devices at room temperature by injecting DC currents I into the Pt electrode, as shown in Fig. 5.2(b). The “field-free” here refers to no external magnetic field being applied, as typically required in perpendicular SOT devices. The resistance variation of the MTJ at zero fields, with a $D = 150$ nm, is consistent with the magnetoresistance loop in Fig. 5.2(c). When the MTJ was reversed to the P state (the low-resistance state) by currents, we recorded the magnetoresistance loop (blue line in Fig. 5.2(c)). The exchange bias has been reversed to -51.3 mT by the current as well, indicating a full reversal of the antiferromagnetic spin at the IrMn/CoFeB interface. In contrast, the hysteresis loop for the CoFeB reference layer remains unchanged. The state of the IrMn layer is accordingly defined as n^+ , consistent with the P state of the MTJ. Note that the defined states of the IrMn layer, either n^+ or n^- , refer to the states of interfacial pinned spins that are strongly coupled to IrMn bulk order[101]. Due to the IrMn/CoFeB bilayer shows a blocking temperature of ~ 500 K in Fig. 4.7. Consequently, the antiferromagnetic pinned spins are expected to remain stable when sweeping external fields at room temperature, which, therefore, are responsible for the observed exchange bias.

We can see that the exchange bias field at the IrMn/CoFeB interface, which is larger than the CoFeB coercive field, yields the imprint of the IrMn state on the CoFeB storage layer, thus on the MTJ resistance. Based on the magnetoresistance loop in Fig. 5.2(c), the high resistance of $R_H = 9.5 \text{ k}\Omega$ and low resistance of $R_L = 5.1 \text{ k}\Omega$ is observed at zero fields, indicating a TMR ratio of 86.2% and a resistance variation of 4.4 k Ω . Previous reports realized the direct detection of antiferromagnets by AMR or AHE. However, the AMR ratio is typically below 1% and the resistance variations for AMR and AHE are about 10 m Ω ~ 40 m Ω [102][103] and 50 m Ω [104], respectively, thus limiting the integration of antiferromagnetic devices. As a stark contrast, our devices allow for the indirect but sensitive detection of the antiferromagnetic order by TMR.

5.2 The endurance and magnetic field immunity

The introduction of antiferromagnets in MTJs can offer unique possibilities to develop high-performance spintronic memories. As has been widely investigated, the current schemes for SOT-MRAM, with MTJs being perpendicular[40] or in-plane[108][109], are hard to satisfy simultaneously the good scalability and field-free data writing. By adopting a hybrid exchange-biased storage in three-terminal MTJs, our exchange-biased MRAM (EB-MRAM) meets these demands. The conventional SOT-MRAM are based on uniaxial ferromagnets, whose states can be altered by external magnetic fields (Fig. 5.3(a)). In contrast, the states of our proposed EB-MRAM devices can only be temporarily changed by external fields. This is because the data bit is stored in the antiferromagnets rather than ferromagnets and the strong unidirectional anisotropy at the AFM/FM interface results in only one energy-minimum state at zero fields (Fig. 5.3(b)). Therefore, our EB-MRAM devices, with diameters down to 40 nm, can recover their original state even after applying and then removing external magnetic fields of 2 T (Fig. 5.3(c)). This field immunity promises good scalability of our devices towards the 10 nm advanced node.

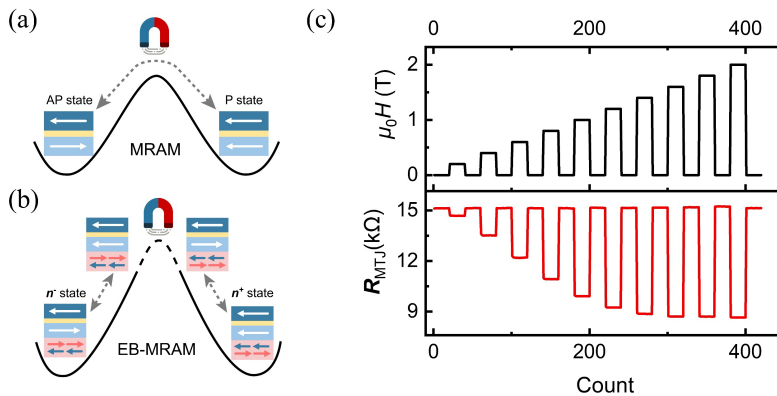


Fig. 5.3 Magnetic field immunity and power consumption estimation. (a) Schematic of typical uniaxial MRAM devices. External magnetic fields can alter the MTJ between the two energy-minimum states, i.e., the AP and P states. (b) Schematic of our unidirectional EB-MRAM devices, which can recover their original states after the removal of external magnetic fields. (c) Magnetic field immunity verification of our EB-MRAM devices.

Furthermore, we can realize reproducible field-free switching of our devices, and no electromigration was found in 2×10^{11} write attempts (Fig. 5.4(a)(b)). Note that the storage layer design is a revisit to TA-MRAM but our EB-MRAM having a distinct device structure possesses largely improved performance. To be specific, the TA-MRAM has a complex writing procedure, including heating, writing, and cooling, and the heating current should pass through the MTJs. Consequently, both switching speed and device endurance are limited. Whereas, in our EB-MRAM, the writing currents pass only through the bottom electrode, contributing to a better endurance and speed than the TA-MRAM. We calculated the power consumption of our devices by $j_c^2 \rho_{Pt} l w d \tau$, where ρ_{Pt} is the resistivity of Pt; l , w , and d are the length, width, and thickness of the Pt bottom electrode, assumed to be 100 nm, 100 nm, and 8 nm, respectively. The power consumption is estimated to be 0.25 pJ/bit at a 1 ns switching speed, which is comparable to the 0.4 pJ/bit for state-of-the-art perpendicular SOT-MRAM but with the merit of data writing.

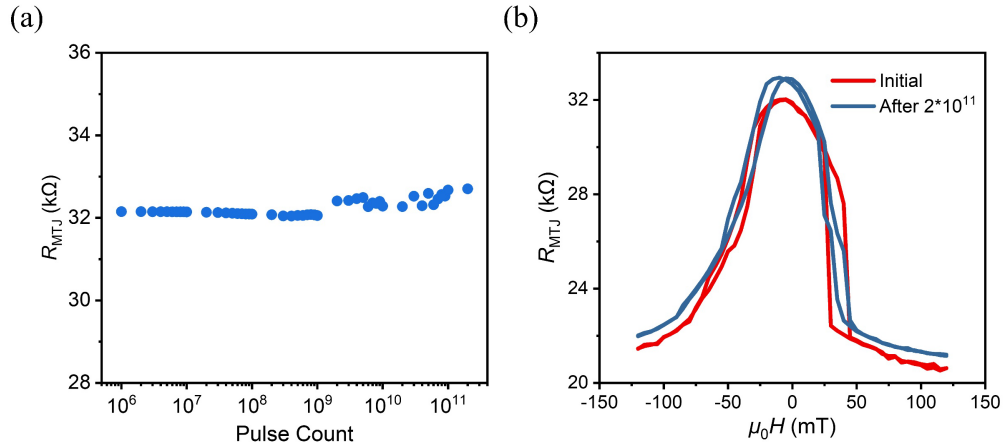


Fig. 5.4 Endurance test in an 86 nm Pt device. (a) Resistance at AP state during the 2×10^{11} write attempts. (b) Hysteresis loop recorded before and after the endurance test.

5.3 Thermal-assisted and Oersted field-induced switching

Following the achievement of fundamental read and write operations for the exchange biased device, we proceeded to investigate the writing mechanism. In zero magnetic field, we also observed similar current-induced exchange bias switching phenomena in devices featuring 8 nm Cu, Ru, and W bottom electrodes. The corresponding current-induced switching curves and hysteresis loops are shown in Fig. 5.5. Notably, our observations indicate: (1) the exchange-biased device exhibits a higher switching current density compared to conventional SOT-MRAM devices; (2) the spin current generating from the Pt bottom electrode is absorbed by IrMn layer, impeding its transmission through the 6 nm IrMn layer and precluding its impact on the CoFeB storage layer; (3) the switching polarity aligns with the current-induced Oersted field. All these phenomena make us suspect that the DC current induced exchange bias switching is similar to TA-MRAM.

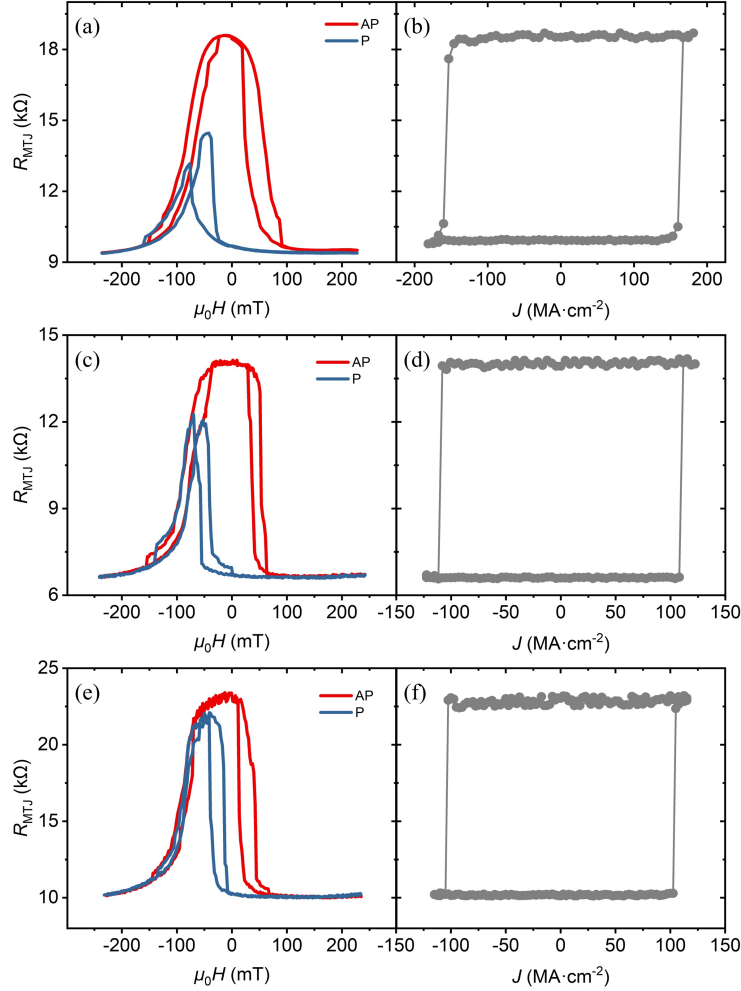


Fig. 5.5 (a)(c)(e) Hysteresis loops before/after the switching and (b)(d)(f) current-induced switching in Cu, Ru, and W bottom electrode devices.

When the current-induced temperature exceeds the blocking temperature, the exchange bias of the storage layer becomes zero. To experimentally obtain the exchange bias field $\mu_0 H_e$ and coercive field $\mu_0 H_c$ at different driving currents, we need to measure the hysteresis loop. However, we note that this is only plausible when the applied current density is relatively low. Otherwise, the devices will be broken down because of the strong Joule heating effect. Fig. 5.6(a) shows the measured hysteresis loop of the CoFeB storage layer when different currents were applied. The exchange bias field $\mu_0 H_e$ and coercive field $\mu_0 H_c$ are summarized in Fig. 5.6(b). Comparing Fig. 4.7(b) and Fig. 5.6(b), we can determine the device temperature is close to the blocking temperature. Additionally, we can observe the coercive field strongly reduced when closed to the switching threshold. The Oersted field generated by the Pt can be estimated by $\mu_0 H_{Oe} = \mu_0 j_{Pt} d_{Pt} / 2$. We can see that at the critical current density of $54.14 \text{ MA}\cdot\text{cm}^{-2}$, the $\mu_0 H_e$ becomes negligible while $\mu_0 H_c$ is 1.7 mT . At this current density, the Oersted field is calculated as $\mu_0 H_{Oe} = 2.7 \text{ mT} > \mu_0 H_c$. Therefore, the thermal-assisted and Oersted field-induced exchange bias switching can be demonstrated in the DC current regime.

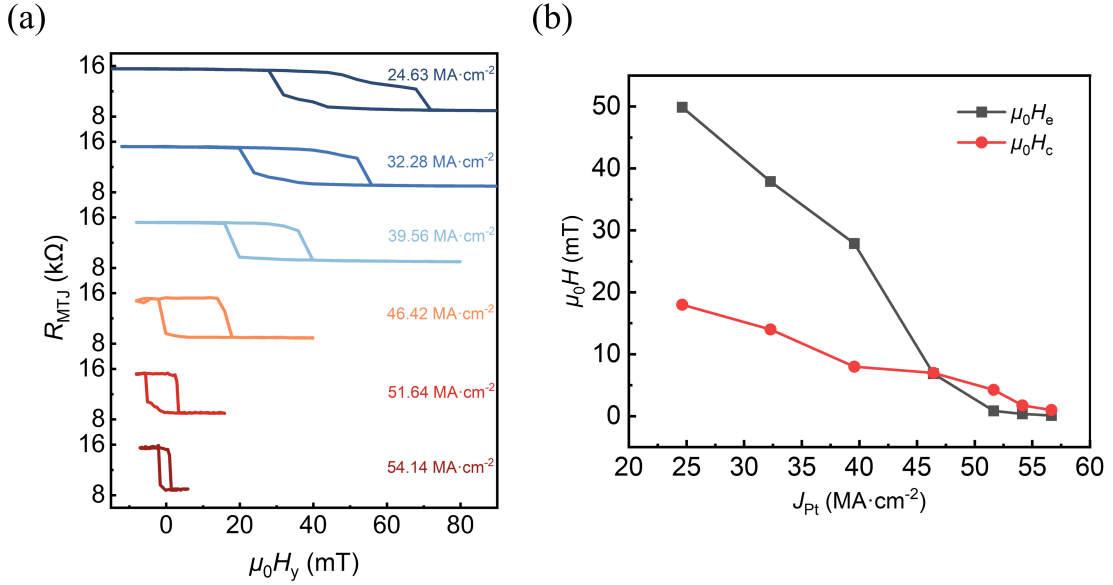


Fig. 5.6 Comparison of the Oersted field and the coercivity field upon injecting currents. (a) Hysteresis loop when different current density is applied. (b) Extracted exchange bias and coercivity field as a function with current density. (c) Influence of external field along y axis on switching.

5.4 The short-pulse measurement and sub-nanosecond dynamics

The three-terminal MTJ devices with a large TMR readout signal provide an effective method to study the electrical manipulation of antiferromagnets. Although we realized the switching of antiferromagnetism at the IrMn/CoFeB interface, the underlying mechanism remains unclear. The switching polarity in our DC experiments is consistent with the direction of the Oersted field generated in the Pt bottom electrode. This result suggests thermally assisted switching (TAS), that is, the applied current heats the IrMn/CoFeB storage layer above its blocking temperature while the Oersted field switches the CoFeB layer, which then induces IrMn switching. Under this scenario, the switching of the exchange bias reveals the switching of the IrMn bulk order. Recent theories and experiments suggest that the SOT can switch the antiferromagnet. In our MTJ devices, the spin current generated by the Pt bottom electrode is absorbed by the IrMn layer, which may influence the switching of IrMn.

To discern whether SOT contributes to the observed phenomena, we performed short-pulse experiments. Fig. 5.7(a) shows the schematic of our measurement setup with two-channel pulse injection. Two phase-matched pulses generated by an arbitrary waveform generator with a 0.2 ns rise time were injected into the Pt bottom electrode. The two inputs V_1 and V_2 were of equal amplitude but opposite signs while the oscilloscope was grounded, which ensures a negligible potential difference across the MgO barrier. After each write pulse, we injected a small current into the MTJ to measure its resistance. The magnetization dynamics during pulse injection could be captured by the oscilloscope when a voltage bias was applied across the MTJ [40], i.e., $V_1 + V_2 \neq 0$.

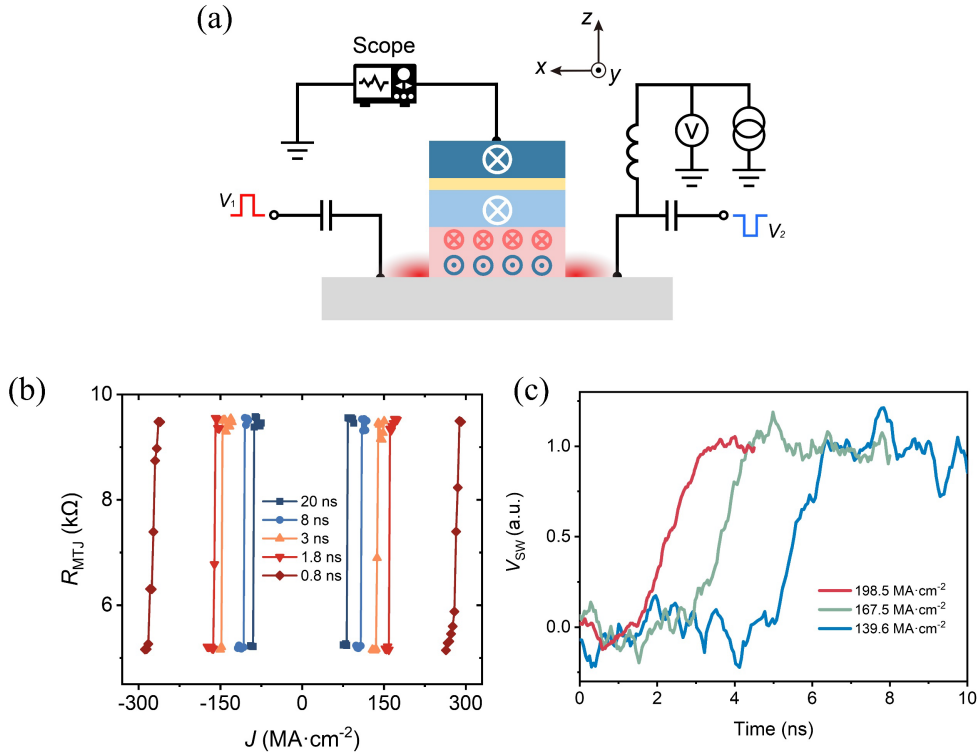


Fig. 5.7 Subnanosecond switching and single-shot dynamics. (a) Schematic of the experimental setup for short-pulse measurements. (b) Field-free current-induced switching loops of the MTJ (150 nm diameter) with pulse widths between 0.8 ns and 10 ns. (c) Averaged single-shot dynamics of the MTJ at different applied current densities. The incubation time is defined as the time to reach $V_{\text{sw}} = 5\%$, while the transition time is derived from the time interval between $V_{\text{sw}} = 5\%$ and $V_{\text{sw}} = 95\%$.

We realized the field-free switching with the pulse width τ down to 0.8 ns (Fig. 5.7(b)). This subnanosecond switching is a clue towards the SOT contribution due to the difficulty of achieving a substantial temperature increase in such a short period. The switching polarity is also consistent with the Oersted field direction, which will be discussed in detail in the next section. We also performed time-resolved measurements of magnetization switching. A fixed bias voltage of 1 V was applied between the MTJ and oscilloscope to capture the real-time dynamics. The voltage applied to the Pt bottom electrode ($V_1 - V_2$) ensures a switching probability $P_{\text{sw}} = 1$. Fig. 5.7(c) shows the switching dynamics of the normalized voltage signal V_{sw} averaged over 10 single-shot switching events. A two-step switching process that involves an incubation time and transition time can be observed. With increasing current density, both incubation time and transition time show significant reduction rates of 80% and 57%, respectively. In essence, the signal V_{sw} reflects the dynamics of the CoFeB storage layer. Because the CoFeB layer is strongly coupled to the IrMn layer at the beginning, the CoFeB magnetization should remain almost static until it is decoupled from IrMn; this decoupling process contributes to the incubation time. This is also the reason why the effect of external fields on incubation time is found to be limited while the effect on transition time is more pronounced.

5.5 Exchange bias switching mechanism

To further distinguish the contribution of SOT and Joule heating, we analyzed the critical switching current density J_c as the pulse width τ varied from 0.8 ns to 40 ns, as shown in Fig. 5.8(a). Each point was calculated based on 100 set-reset events, and the critical current density was retrieved at $P_{sw} = 0.5$. We first considered the TAS model of MTJs within a given pulse[68]:

$$T = T_0 + \frac{1}{K} \cdot J_c^2 \cdot (1 - e^{-\frac{\tau}{\tau_0}}) \quad (5.1)$$

where T is the device temperature, T_0 is the room temperature, τ_0 is the characteristic heating time, and K is the proportionality constant between J_c^2 and the temperature increase of the system. Therefore, improving heat generation efficiency or reducing heat dissipation can reduce the J_c . Setting T as the blocking temperature T_b , Eq. (5.1) is equivalent to:

$$J_c^2 = K(T_b - T_0) \cdot (1 - e^{-\frac{\tau}{\tau_0}})^{-1} \quad (5.2)$$

As shown via the red and black curves in Fig.5.8(a), Eq. (5.2) fits well with our experimental data when $\tau \geq 5$ ns, but an apparent deviation can be observed in the sub-nanosecond regime. Specifically, compared to those of the TAS model, the measured J_c values show a decrease of 13.1% at 3 ns and 35.9% at 0.8 ns for the MTJ with a $D = 150$ nm. No obvious size dependence is observed when the diameter of the MTJs is varied from 77 nm to 700 nm, which is attributed to the multidomain switching behavior in such a dimension scale and indicates that devices with larger sizes can still be used for distinguishing the SOT contribution. We then replaced the Pt bottom electrode with Cu, which is considered to have a negligible spin Hall angle. The Cu devices of a 700 nm diameter show magnetoresistance properties similar to those of Pt devices, with $\mu_0 H_e > \mu_0 H_c$. Additionally, the switching of antiferromagnetism down to 2.2 ns is

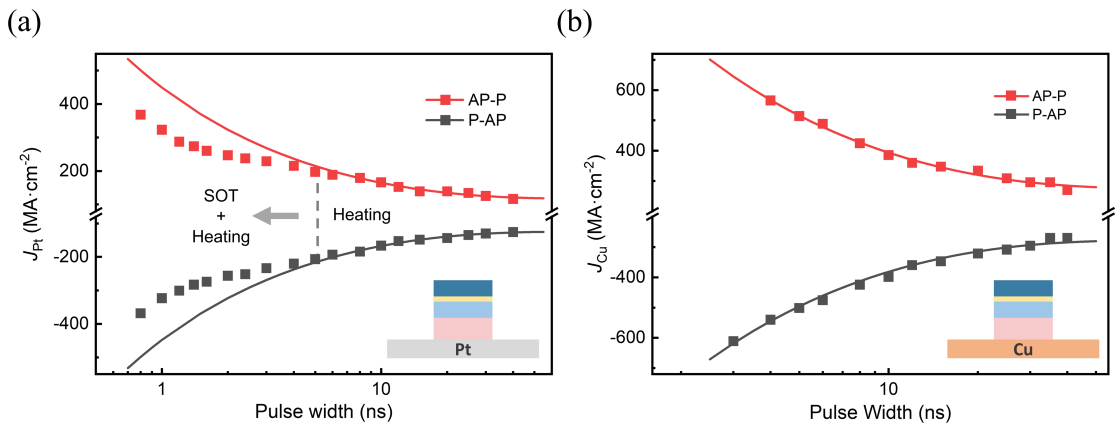


Fig. 5.8 Contribution of SOT to device switching under short pulses in devices with Pt bottom electrodes (a) or Cu bottom electrodes (b), with critical switching current density J_c as a function of pulse width. The solid line shows the fit of the experimental data to the model using the thermal-assisted model, and Pt differs more from the TAS model at short pulses compared to the Cu electrode.

achieved in the Cu devices (reaching the voltage limit 18 V of our setup) but shows good agreement with the TAS model over the whole tested timescale (Fig. 5.8(b)), which is in stark contrast with the Pt devices.

The comparison between the Pt and Cu devices, and the significant decrease in J_c from the TAS model in the Pt devices serve as evidence for the SOT contribution. The spin Hall angle of Pt was measured as 0.09 by spin-torque ferromagnetic resonance technique (ST-FMR). Consequently, the switching of our Pt devices is dominated by the TAS mechanism when the pulse width $\tau \geq 5$ ns but is completed by the interplay of SOT and heating when τ is further reduced, possibly due to the increase in the SOT magnitude and the difficulty of heating devices above the T_b within a short pulse.

Here we performed macrospin simulations to provide a more general picture of SOT-driven switching of antiferromagnets in Pt/AFM/FM trilayer. The schematic is shown in Fig. 5.9. We considered a colinear antiferromagnet that was simplified as four successive layers, with layers 1 and 3 belonging to sublattice A and layers 2 and 4 belonging to sublattice B. The FM layer was strongly exchanged and coupled to layer 1, with $\mu_0 H_e = 50$ mT and $\mu_0 H_c = 15$ mT. We define the Néel order of the AFM layer as $\mathbf{n} = (\mathbf{m}_1 - \mathbf{m}_2)/2$, where \mathbf{m}_i denotes the magnetization of layer i in the AFM. The system was initialized to the \mathbf{n}^- state, i.e., layer 1 points along $-y$ direction while layer 2 points along $+y$ direction. SOT was only applied in layer 3 and layer 4 because of the limited spin diffusion length in our experiments. Finally, the Oersted field generated by the Pt layer was included to switch the FM layer.

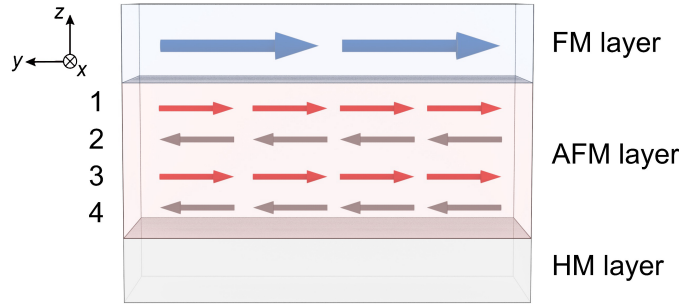


Fig. 5.9 Schematic of the simulated Pt/AFM/FM trilayer.

Macrospin simulations were performed by solving the Landau–Lifshitz–Gilbert (LLG) equation:

$$\frac{d\mathbf{m}_i}{dt} = -\gamma\mu_0(\mathbf{m}_i \times \mathbf{H}_{eff,i}) + \alpha \left(\mathbf{m}_i \times \frac{d\mathbf{m}_i}{dt} \right) + \gamma\mu_0 H_{SOT}(\mathbf{m}_i \times \boldsymbol{\sigma} \times \mathbf{m}_i) \quad (5.3)$$

where the subscript $i = 1, 2, 3, 4$ or FM denotes layer i of the AFM layer or FM layer. \mathbf{m}_i and $\mathbf{H}_{eff,i}$ are the reduced magnetization and effective field, respectively. In our simulations, we set $\mathbf{H}_{eff,FM} = H_c m_{y,FM} \hat{y} + H_e \mathbf{m}_1 + H_{Oe} \hat{y}$, where H_c denotes the coercive field of FM layer, H_e is the exchange bias field and $H_{Oe} \approx J_{pt} \cdot d_{pt}/2$ is the Oersted field generated by the Pt bottom electrode with a Pt thickness d_{pt} . Correspondingly, for layer 1 in the AFM, $\mathbf{H}_{eff,1} = H_k m_{y,1} \hat{y} + H_0 \mathbf{m}_{FM} - H_{ex} \mathbf{m}_2$, where H_k is the uniaxial anisotropy field of the AFM, H_0

denotes the exchange coupling layer 1 feels and $-H_{ex}$ is the Heisenberg exchange field between adjacent layers in the AFM. For layer 2 ~ layer 4, $\mathbf{H}_{eff,2} = H_k m_{y,2} \hat{\mathbf{y}} - \frac{1}{2} H_{ex} \mathbf{m}_1 - \frac{1}{2} H_{ex} \mathbf{m}_3$, $\mathbf{H}_{eff,3} = H_k m_{y,3} \hat{\mathbf{y}} - \frac{1}{2} H_{ex} \mathbf{m}_2 - \frac{1}{2} H_{ex} \mathbf{m}_4$ and $\mathbf{H}_{eff,4} = H_k m_{y,4} \hat{\mathbf{y}} - H_{ex} \mathbf{m}_3$. $H_{SOT} = \frac{\hbar \theta_{SH} J_{Pt}}{2et\mu_0 m_s}$ is the field strength of the damping like SOT, which is only applied in layer 3 and layer 4, with \hbar , θ_{SH} , J_{HM} , e , t and m_s representing the reduced Planck constant, spin Hall angle, current density in the heavy metal electrode, elementary charge, spin penetrating depth in the AFM and saturation magnetic moment of the AFM atom per unit cell volume, respectively. Additionally, α is the Gilbert damping constant, μ_0 is the vacuum permeability and γ is the gyromagnetic ratio. In our simulations, we set $\mu_0 H_K = 0.2$ T, $\mu_0 H_e = 50$ mT, $\mu_0 H_c = 10$ mT, $\mu_0 H_0 = 10$ mT, $\mu_0 H_{ex} = 100$ T, $\theta_{SH} = 0.09$, $t = 2$ nm, $m_s = 2 \times 10^5$ A·m⁻¹, $\alpha = 0.01$, $J_{Pt} = 400$ MA·m⁻², $d_{Pt} = 8$ nm, and $\boldsymbol{\sigma} = (0, 1, 0)$. Moreover, $\mu_0 H_c$ was set to 15 mT at zero currents but set to 2 mT at J_{Pt} because of the observed reduction in the coercive field when applying the write currents in our experiments. All the simulations were performed at $T = 0$ K.

First, we set the system to the \mathbf{n}^- state, as shown in Fig. 5.10(a). Upon applying SOT currents, the damping-like SOT generated by Pt drives the high-frequency precession of AFM bulk order, which results in the decoupling between the AFM layer and the FM layer (Fig. 5.10(b)). Then, the FM magnetization can be reversed by the Oersted field generated by the Pt layer (Fig. 5.10(c)). After removing the SOT currents, the interfacial exchange coupling will give a preferred state of both the bulk order and the interfacial antiferromagnetism and a reversed exchange bias is also established (Fig. 5.10(d)).

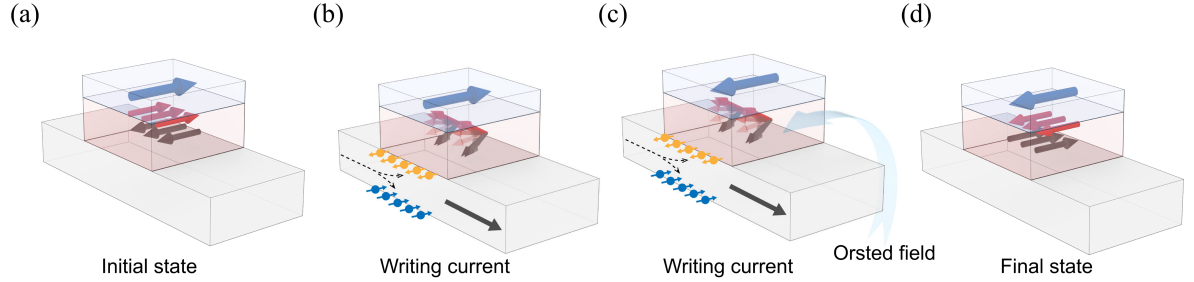


Fig. 5.10 Schematics of the SOT-dominated switching mechanism. (a) Initial state, i.e., \mathbf{n}^- state. (b) SOT drives high-frequency precession of AFM order. (c) The FM layer is reversed by Oersted field generated by the Pt layer. (d) After removing SOT currents, the AFM order relaxes to the new state, the \mathbf{n}^+ state, due to exchange coupling with the adjacent FM layer.

We attribute the significant reduction of $\mu_0 H_{EB}$ to the different timescale of spin dynamics in the FM and the AFM layer. As shown in Fig. 5.11(a), the Néel order of the AFM layer will precess with a period of only 2.6 ps during the application of SOT currents, which is inaccessible for the FM layer. As such, the FM layer decouples from the IrMn layer. The small exchange bias of -5 mT is rationed from the slight canting of both sublattices in the AFM layer towards the spin polarization direction, i.e., $(0,1,0)$ in our simulations. Then, the generated

Oersted field, estimated as $\mu_0 H_{Oe} \approx \frac{1}{2} \mu_0 J_{pt} \cdot d_{pt} = 20 \text{ mT}$, can switch the CoFeB magnetization. In the experiments, the Joule heating will further result in a reduction of coercive field of CoFeB. Therefore, for the simulations of switching, we set $\mu_0 H_c = 2 \text{ mT}$ after $t = 0.2 \text{ ns}$ to account for the coercive field reduction.

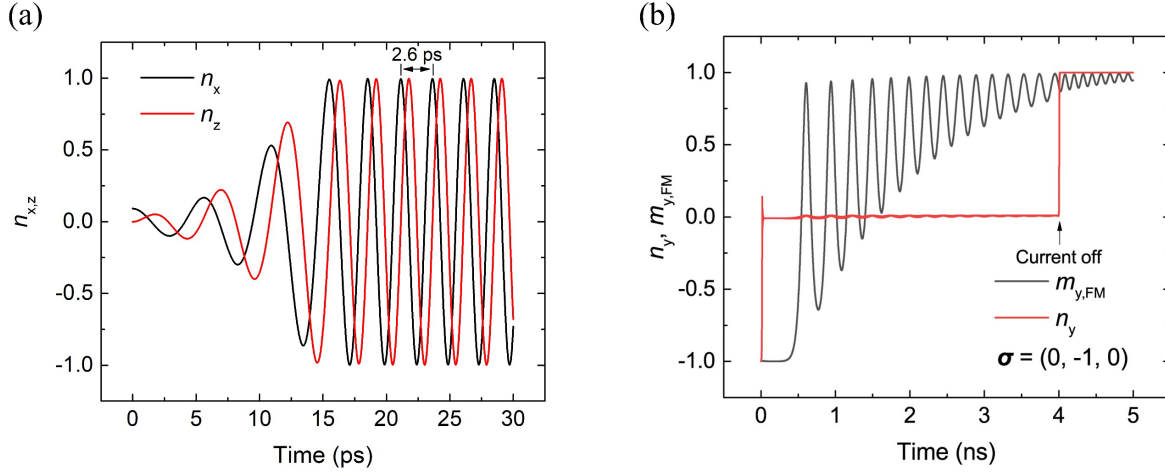


Fig. 5.11 (a) Time evolution of the x and z components of the Néel order \mathbf{n} . (b) Time evolution of the y component of FM magnetization and AFM Néel order.

We then show that the deterministic switching of the Néel order \mathbf{n} can be realized if we include the interfacial exchange coupling. Fig. 5.11(b) shows the time evolution of the AFM and the FM layer when applying a SOT current of 4 ns and then relaxing for 1 ns. Because of the precession frequency of antiferromagnets being much higher than the FM layer, the FM layer decouples from the AFM layer and then is switched by the Oersted field. Note that the large difference in the spin dynamics between the AFM and the FM layer indicates that layer 1, which is interfaced with the FM layer, will always feel an exchange coupling field $\mathbf{H} = H_0 \mathbf{m}_{FM}$, where \mathbf{m}_{FM} is the reduced magnetization of the FM layer and H_0 is the magnitude. Consequently, the layer 1 (sublattice A) tends to align along the $+y$ direction after the current is removed because the FM layer has been reversed to the $+y$ direction by the Oersted field, while sublattice B simultaneously relaxes to the opposite direction. Therefore, both the AFM interfacial antiferromagnetism and FM magnetization realize deterministic switching to the \mathbf{n}^+ state. Our simulations clearly indicate that the switching polarity of Néel order is determined by the FM magnetization, which can then be altered by Oersted fields or external magnetic fields. This explains why the switching polarity of our devices can be reversed by external magnetic fields.

5.6 Exchange biased devices with tungsten (W) insert layer

In Chapter 4, we explored the the nonmagnetic insert layer's thickness dependence on the interface of an exchange-coupled antiferromagnetic/ferromagnetic bilayer. Our results show a significant decrease in both the exchange bias field and coercive field as the thickness of the nonmagnetic spacer layer increased. Furthermore, the CoFeB storage layer switching mechanism of the Pt bottom electrode devices' remains the current-induced Oersted field. While keeping the hysteresis loop fully shifted to one side, our investigation indicates that reducing the exchange bias and coercive field provides a benefit in terms of reducing power consumption during the write process. The device, as illustrated in Fig. 5.12(a), comprises the following stack: SiO Sub./Ta (1.0)/Pt (8.0)/Ir₂₀Mn₈₀ (6.0)/W (*t_w*)/Co₂₀Fe₆₀B₂₀ (1.9)/MgO (1.6)/Co₂₀Fe₆₀B₂₀ (2.4)/Ru (0.8)/CoFe₃₀ (2.0)/Ir₂₀Mn₈₀ (7.5)/Ru (2.0)/Ta (3.0)/Ru (10.0) (nm), where *t_w* varies in 0, 0.1, and 0.2 nm. The hysteresis loops of the CoFeB storage layer, depicted in Fig. 5.12(b), further support our observation that the exchange bias field and coercive field of the CoFeB storage layer exhibit a rapid decrease with an increasing thickness of the W insert layer.

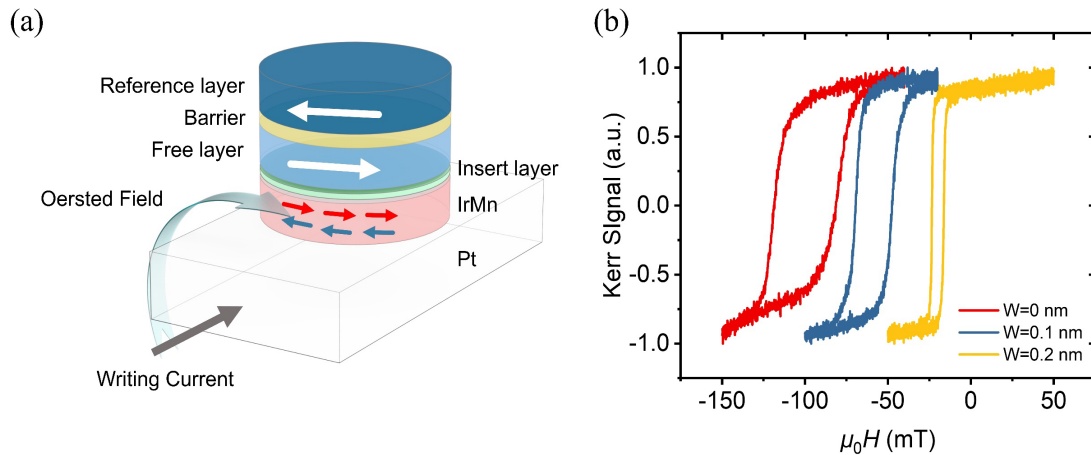


Fig. 5.12 (a) Schematic of the exchange bias device with W insert layer. (b) Hysteresis loop of the CoFeB storage layer with 0, 0.1 and 0.2 nm W insert layer.

Fig 5.13(a) illustrates current-induced switching with varying W insert layer thicknesses at a pulse width of 100 ns. Notably, the 0.2 nm W insert layer exhibits a higher TMR compared to the device without spacer layer. This enhancement is attributed to the W insert layer's effective prevention of interfacial element diffusion during high-temperature annealing, thereby contributing to improved performance in the MTJ device. Additionally, the device with a W spacer layer experiences a significant reduction in the critical switching current density. To delve deeper into this, we investigated the dependency of the critical switching current density on pulse width during AP-P switching for devices with different W insert layer thicknesses, as depicted in Fig. 5.13(b). The results indicate a notable decrease in the critical switching current density within the 20 ns to 1 ms pulse width range with an increase in the W insert layer thickness. Consequently, the W insert layer not only proves advantageous in diminishing the critical switching current density to enhance the MTJ device performance but also validates the switching mechanism driven by the Oersted field.

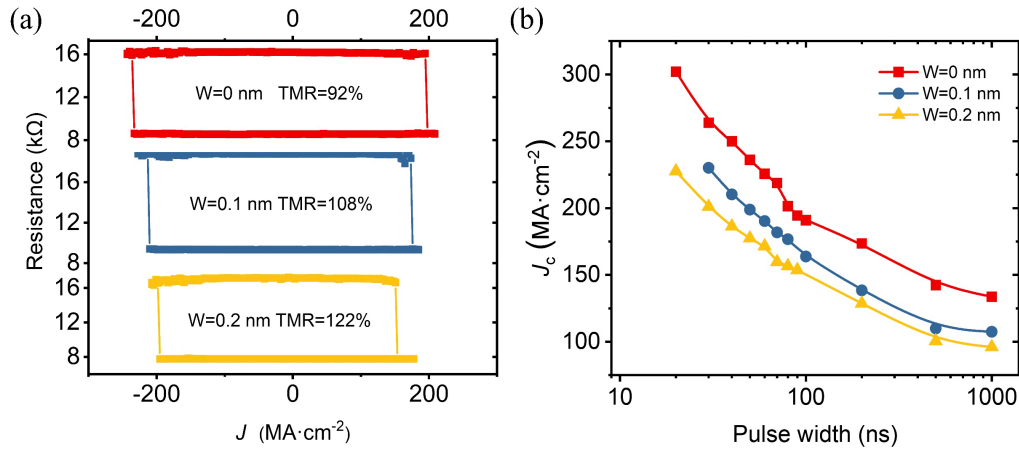


Fig. 5.13 (a) The current-induced switching with various insert layer thickness. (b) The critical switching current density J_c as a function of pulse width with various insert layer thickness.

5.7 Exchange bias switching in IrMn bottom electrode devices

In Pt bottom electrode devices, the primary factor affecting switching efficiency is the ferromagnetic layer's switching. Minimizing power consumption remains challenging, as the current density for generating Oersted field proves difficult to further reduce, even when considering the joined effects with SOT in a short pulse range. To directly utilize the SOT effect in storage layer switching, we propose a novel device structure, which uses IrMn directly as the bottom electrode with an ultrathin seed layer, achieved through the optimization of seed layer thickness and antiferromagnetic thickness. The stacks' structure is SiO Sub./Ta (1.0)/Ru (1.0)/Ir₂₀Mn₈₀ (4.0)/Co₂₀Fe₆₀B₂₀ (1.9)/MgO (1.6)/Co₂₀Fe₆₀B₂₀ (2.4)/Ru (0.8)/CoFe₃₀ (2.0)/Ir₂₀Mn₈₀ (7.5)/Ru (2.0)/Ta (3.0)/Ru (10.0) (nm). In this configuration, the IrMn bottom electrode serves not only to provide exchange bias but also enhances the switching efficiency of the ferromagnetic layer through the intrinsic SOT effect of IrMn itself. Comparisons were

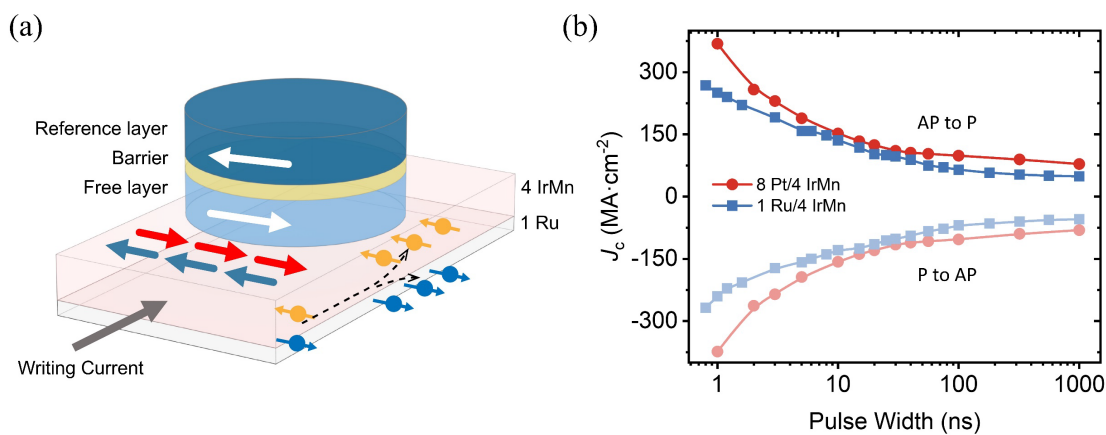


Fig. 5.14 (a) Schematic of the exchange bias device with W insert layer. (b) The critical switching current density J_c as a function of pulse width in Ta (1.0)/Ru (1.0)/IrMn (4.0) and Ta (1.0)/Pt (8.0) bottom electrode.

made with devices having Ta (1.0)/Pt (8.0) and Ta (1.0)/Ru (1.0)/IrMn (4.0) bottom electrode structures with the same 4 nm IrMn thickness. The critical switching current densities at various pulse widths are presented in Fig. 5.14(b), revealing that devices with IrMn-bottomed electrodes exhibit lower critical switching current densities across the entire pulse width range.

Furthermore, we devised a wedged CoFeB storage layer with thickness variations ranging from 1 to 2 nm to optimize SOT writing efficiency. In Fig. 5.15(a), the switching characteristics of the CoFeB storage layer are depicted at pulse widths of 10 ns for thicknesses of 1.2, 1.5, and 1.9 nm. Notably, the critical switching current density and device TMR decrease with a reduction in CoFeB thickness. Additionally, we assessed the critical current density during AP-P switching across pulse widths ranging from 10 ns to 1 ms, as shown in Fig. 5.15(b). The smallest critical switching current density was observed at the critical thickness (1.2 nm), marking the transition of the CoFeB storage layer from in-plane magnetic anisotropy to perpendicular magnetic anisotropy.

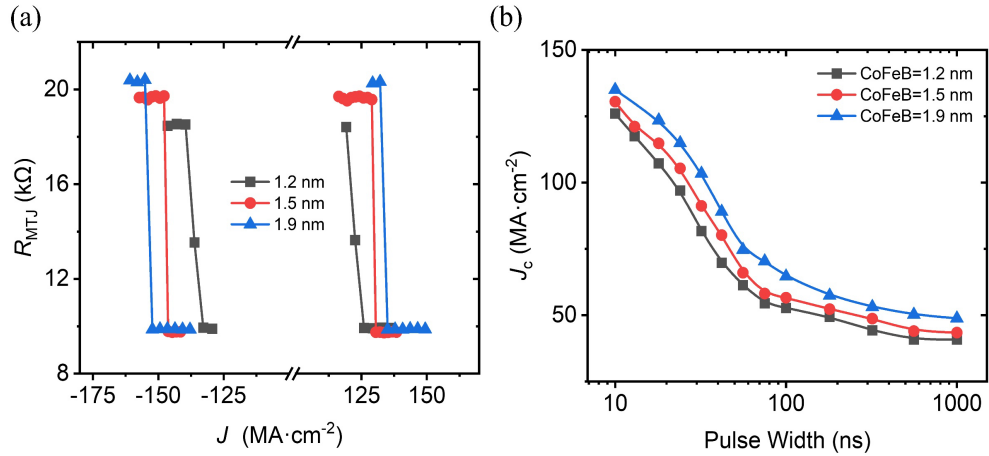


Fig. 5.15 (a) The current-induced switching with various CoFeB thickness. (b) The critical switching current density J_c as a function of pulse width with various CoFeB thickness.

For further study the switching mechanism, the macro-spin simulation based on the AFM/FM bilayer system is applied. Fig. 5.16(a) show the basic model of the simulation, the IrMn layer was simplified as a bilayer co-linear antiferromagnet, with layer 1 and layer 2 representing sublattice A and sublattice B, respectively. The FM layer exhibited strong exchange coupling with AFM layer 1, and SOT acted on both AFM and FM layers simultaneously. The parameters included $\mu_0 H_K = 0.2$ T, $\mu_0 H_{\text{ex}} = 100$ T, $\theta_{\text{SH}} = 0.1$, $t_{\text{IrMn}} = 4$ nm, and $m_s = 3 \times 10^5$ $\text{A}\cdot\text{m}^{-1}$ for AFM layer, and $\mu_0 H_{\text{EB}} = 20$ mT, $\mu_0 H_c = 5$ mT, $t_{\text{CoFeB}} = 1.9$ nm, $m_{\text{eff}} = 0.4$ T, and $m_s = 1.2 \times 10^6$ $\text{A}\cdot\text{m}^{-1}$ for FM layer. Applying a drive current of $J_{\text{SOT}} = 300$ $\text{MA}\cdot\text{m}^{-2}$, Fig. 5.16(b) illustrates the time evolution of the AFM and FM layers over 3 ns, with SOT current applied from 0 to 2 ns. The FM layer is switched to the $+y$ direction by SOT, and after current removal, sublattice A tends to align along the $+y$ direction due to exchange coupling, while sublattice B is oriented in the opposite direction, achieving a deterministic switch to the n^+ state. Conversely, when only 0.25 ns of SOT current is applied (Fig. 5.16(c)), the FM layer maintains on $-y$ direction, resulting in a switch back to the $-y$ direction upon SOT removal. Thus, neither AFM nor FM undergoes a complete switch.

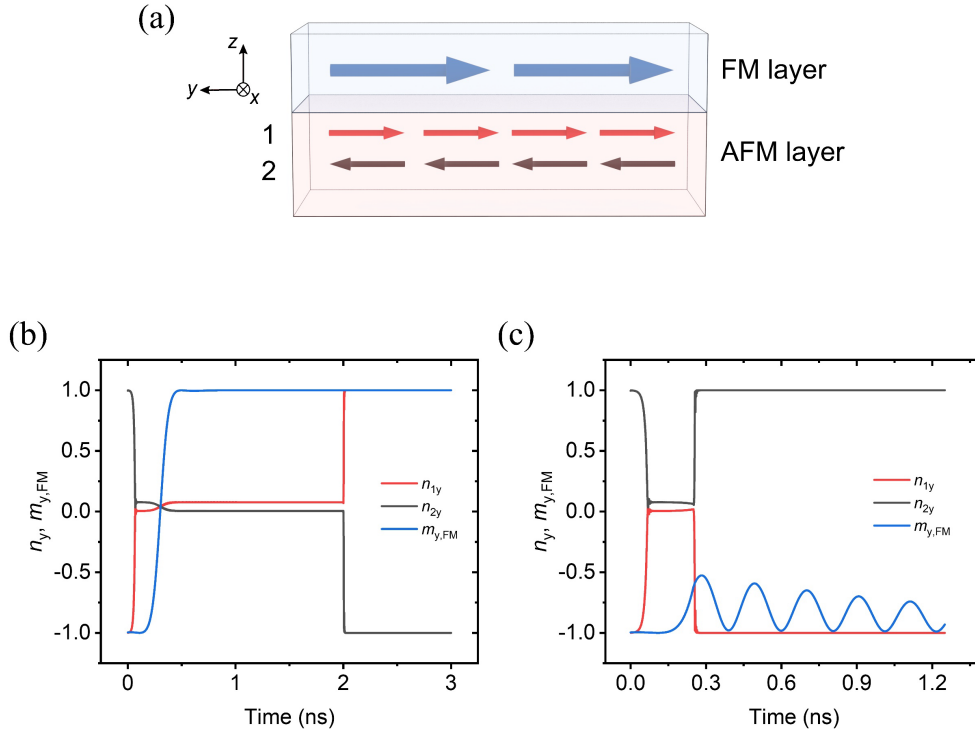


Fig. 5.16 (a) Schematic of the simulated AFM/FM bilayer. (b) Time evolution of the y component of FM magnetization and AFM Néel order. (a) SOT current pulse $\tau = 2.5$ ns. (b) $\tau = 0.25$ ns.

5.8 Summary

Manipulating antiferromagnets by damping-like SOT in HM/AFM heterostructures is an emerging research topic. Because not only the AFM order but also the temperature gradient-induced Seebeck effect in patterned devices can contribute to the AMR or Hall signals, conclusive evidence of SOT-driven AFM switching is currently in demand. In addition, it has been recently demonstrated that thermal excitations, together with temperature gradient-induced strain, can achieve switching of the AFM order[74]. In this work, we detect the state of antiferromagnets indirectly by the TMR, which has a desirable readout signal and with no obvious electromigration effect over 2×10^{11} write attempts, much more robust than the AMR or AHE. The thermoelastic switching mechanism can be ruled out because of the current polarity-dependent switching realized in our experiments. The short-duration pulse tests down to 0.8 ns help us distinguish the contributions of Joule heating and SOT. Our experiments and simulations indicate an SOT origin of the observed sub-nanosecond switching, where the bulk AFM order is driven by the damping-like SOT and its switching polarity is determined by the exchange coupling effect. Furthermore, our proposed three-terminal EB-MRAM devices achieve scalable and efficient storage with high endurance and field immunity. Our work advances both the fundamental and application aspects of antiferromagnets and offers a field-free and scalable scheme towards energy-efficient and high-density electronic devices.

Chapter 6.

Manipulating Exchange Bias by a Single Femtosecond Laser Pulse

During the further investigation of all-optical switching, it was discovered that there are two distinct mechanisms for this phenomenon in GdFeCo alloys. One mechanism, known as AO-HDS, requires multiple circularly polarized light pulses. On the other hand, the other mechanism, all-optical helicity independent switching (AO-HIS), only requires a single linear polarized pulse to realize magnetization switching[112], as shown in Fig. 6.1(a)(b). Radu et al. used time-resolved XMCD to observe the ultrafast switching dynamics of GdFeCo[113]. In their observations (Fig. 6.1(c)(d)), they noticed a rapid decrease in the net magnetization strength of the two sublattices. The net magnetization strength of Fe experienced a significant decay within 300 fs, while Gd demagnetized over a period of up to 1.5 ps. Below 10 ps, the

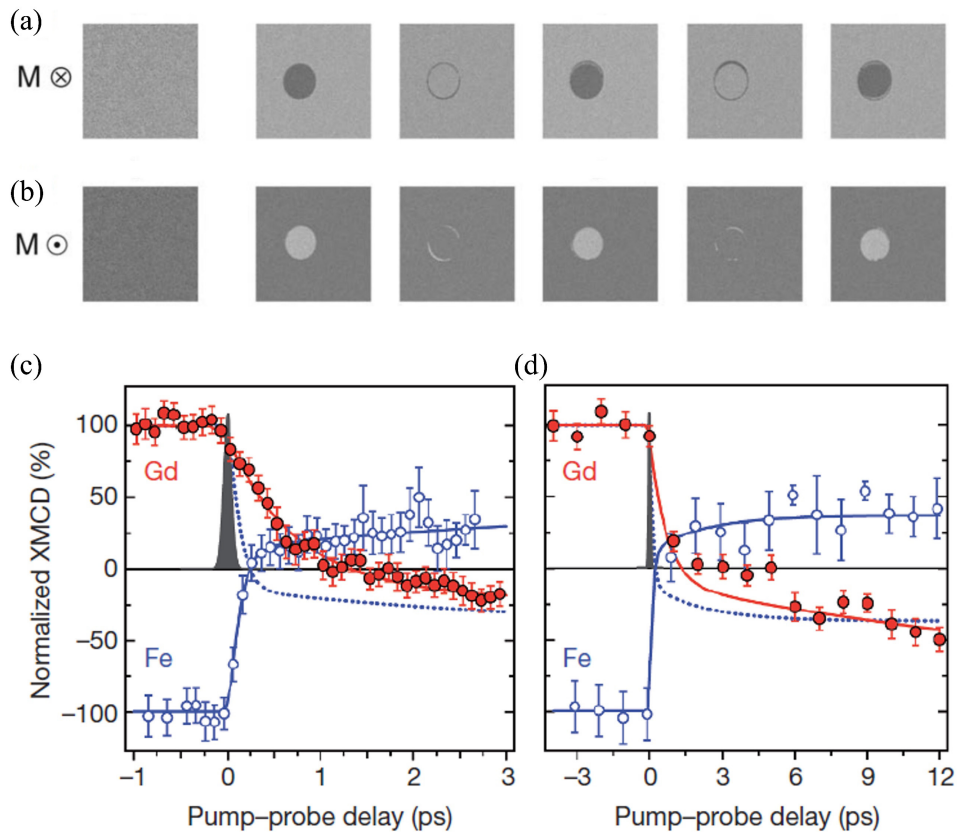


Fig. 6.1 (a) (b) All-optical helicity-independent switching in GdFeCo alloy[112]. (c) Elementally resolved dynamics of Fe and Gd magnetic moments measured with time resolved XMCD measurement. Fe (hollow circle) and Gd (solid circle) magnetic moments in the first 3 ps; (d) but transient kinetics measured over a 12 ps. Measurements were performed at a sample temperature of 83 K, with a laser irradiance of 4.4 mJ/cm^2 and a time resolution of 100 fs[113].

switching dynamics of the Gd and Fe sublattices showed notable differences. Surprisingly, during the timescales where their magnetic moments passed zero, the net moments of Fe and Gd aligned parallel along the z-axis, despite the presence of antiferromagnetic couplings in both spins. This intermediate state, with characteristics similar to ferromagnetism, arises from the inherent differences in the dynamics of the transition and rare-earth metal sublattices. Specifically, the transition metal achieves the demagnetization state faster compared to the rare-earth component. When the Gd spin is reversed, the exchange interaction between Gd and Fe can switch the Fe spin.

The implementation of AO-HIS holds the potential to further reduce the switching time of interface exchange bias. In this chapter, we successfully achieve the manipulation of exchange bias using a single femtosecond laser pulse in an IrMn/CoGd (AFM/FiM) perpendicular exchange bias bilayer structure, as depicted in Fig. 6.2. We thoroughly investigate the influence of laser fluence, pulse numbers, and antiferromagnetic layer thickness on the switching of exchange bias. Through time-resolved measurements, we confirm that the exchange bias can be switched within 100 ps. Atomistic simulations further reveal that the antiferromagnetism of IrMn is demagnetized within a timescale of 100 fs and rapidly recovers after the switching of CoGd. This ultrafast dynamics of the IrMn antiferromagnet under a single femtosecond laser not only significantly reduces the switching time of the exchange bias but also demonstrates the unique characteristics of the antiferromagnetic grains.

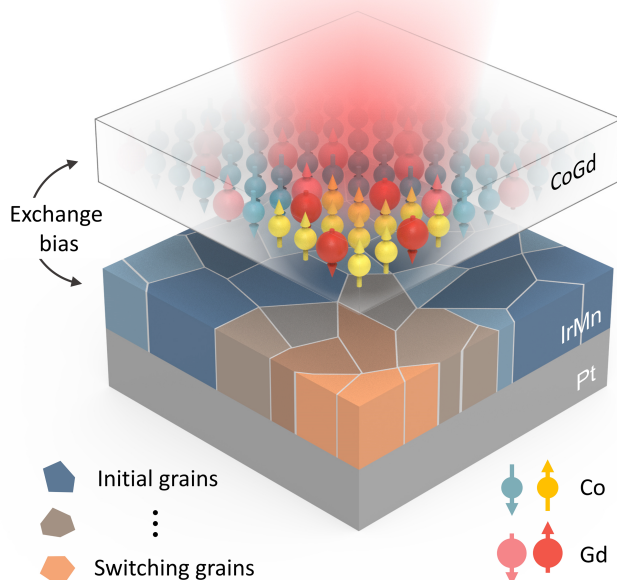


Fig. 6.2 Schematic diagram of the IrMn/CoGd exchange coupling system, which consists of a CoGd amorphous ferrimagnetic layer and an IrMn antiferromagnetic layer with a polycrystalline grains structure and utilizes the AO-HIS of CoGd with a single femtosecond laser for the ultrafast manipulation of the interfacial exchange bias and antiferromagnetic spin.

6.1 IrMn/CoGd perpendicular exchange bias bilayer

Fig. 6.3(a) shows the stack of the IrMn/CoGd perpendicular exchange bias bilayer structure. The multilayer film was grown on a glass substrate using a vacuum magnetron sputtering. The stack of the film is Glass/Ta (5.0)/Pt (5.0)/Ir₂₀Mn₈₀ (t_{IrMn})/Co₇₇Gd₂₃ (4.0)/Pt (5.0) (nm), where the thickness of IrMn varies from 2 to 10 nm. After the thin-film deposition, the samples were annealed at 60 mT and 200 °C to obtain the initial exchange bias. The TEM image in Fig. 6.3(b) reveals that the Ta and CoGd layers are amorphous, while the Pt and IrMn layers are well-crystallized. Magnetic properties of the IrMn-based exchange bias system were generally correlated with the IrMn (111) texture. Therefore, the choice of seed layers for the IrMn layer becomes crucial. The crystallographic structure of the samples after annealing was analyzed by the X-ray diffraction (XRD) technique shown in Fig. 6.3(c). Two XRD peaks can be obtained: the higher one belongs to the (111)-oriented Pt seed layer, and the other is (111)-oriented IrMn. The intensity of the IrMn (111) peak depends on the IrMn thickness.

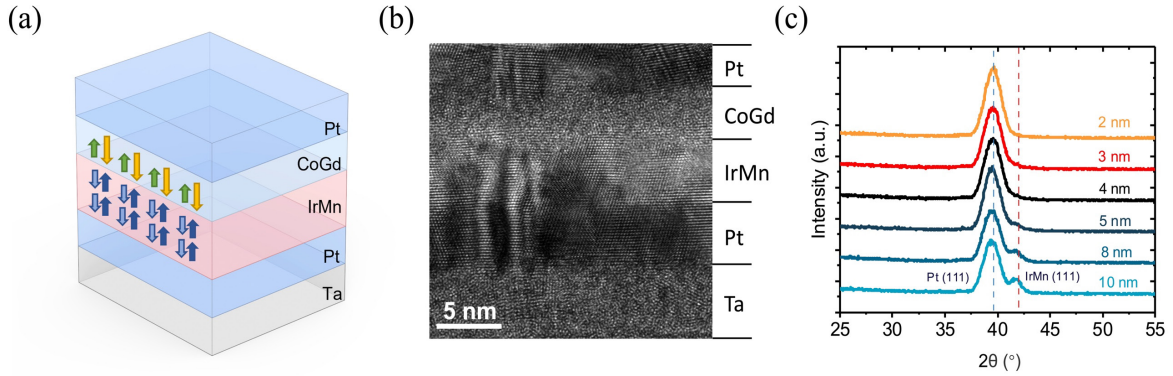


Fig. 6.3 (a) Film structure of IrMn/CoGd exchange coupled system; (b) IrMn/CoGd TEM image, the IrMn on the Pt seed layer forms a good crystallization, while the CoGd still maintains the amorphous state after the annealing; (c) The (111) texture peak of IrMn layer and Pt seed layer was carried out by θ - 2θ XRD scans of the bilayer stacks for different IrMn thicknesses (t_{IrMn} from 2 to 10 nm).

The perpendicular magnetic anisotropy and exchange bias of the IrMn/CoGd bilayer are confirmed by the polar MOKE measurements (Fig. 6.4(a)). The extracted exchange bias field $\mu_0 H_e$ and coercivity $\mu_0 H_c$ as a function of the IrMn thickness are presented in Fig. 6.4(b). The evolution of $\mu_0 H_e$ with t_{IrMn} is similar to that reported in the literature[114]. A noticeable exchange bias field can be observed for an IrMn thickness of $t_{\text{IrMn}}=2$ nm, reaching a maximum at $t_{\text{IrMn}}=4$ nm with $J_{ex} = 0.16$ mJ/m² and decreases when t_{IrMn} is further increased. The coercivity $\mu_0 H_c$ decreases with increasing t_{IrMn} .

In the CoGd alloy, the magnetization of the Gd sublattice is antiferromagnetically exchange coupled to the magnetization of the Co sublattice. The net magnetization of the alloy is given by the contribution of both sublattices and reaches zero at the compensation point. The film

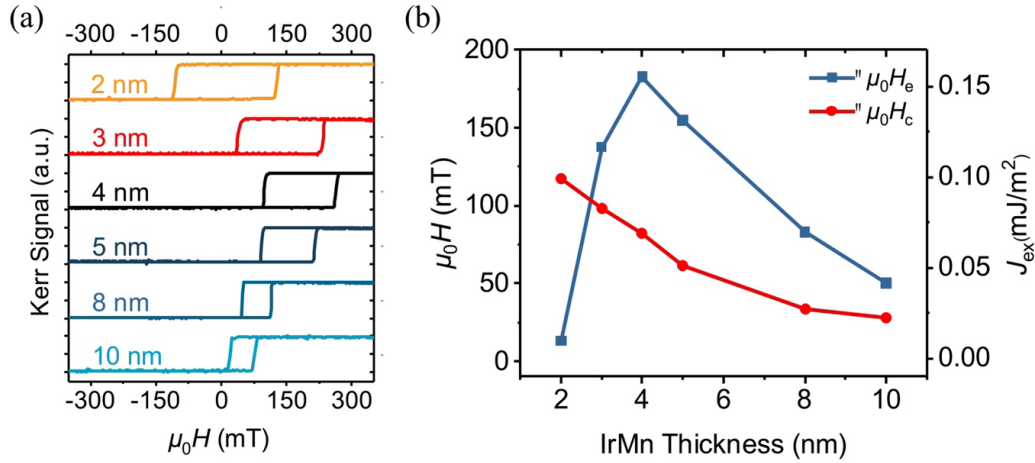


Fig. 6.4 (a) Hysteresis loops obtained on the annealed stacks for different IrMn thickness (t_{IrMn} from 2 to 10 nm) measured by polar MOKE. (b) Exchange bias field $\mu_0 H_e$, effective exchange coupling constant J_{ex} and coercivity $\mu_0 H_c$ as a function of the IrMn thickness (t_{IrMn}).

stack of Sub/Ta (5.0)/Pt (5.0)/Ir₂₀Mn₈₀ (4.0)/Co_{100-y}Gd_y (4.0)/Pt (5.0) (nm) with $y = 23$ to 32% was grown by DC magnetron sputtering on glass substrates. We have characterized IrMn(4.0)/Co_{100-y}Gd_y(4.0) samples with various concentrations. The hysteresis loops are measured by polar MOKE (Fig. 6.5(a)). The summarized coercivity $\mu_0 H_c$ and exchange bias field $\mu_0 H_e$ are shown in Fig. 6.5(b). According to the static hysteresis loops with a changed sign, we can note that the magnetization compensation point is between $y = 30\%$ and 32% at room temperature (300 K). The well crystallization of IrMn and the low M_s of near-compensated CoGd alloy leads to a strong exchange bias field compared to conventional IrMn/FM bilayers. In addition, under the same field annealing conditions, the exchange bias field is opposite near the compensation point, which indicates that the interfacial AFM pinned spin is aligned with the magnetization of the Co moment.

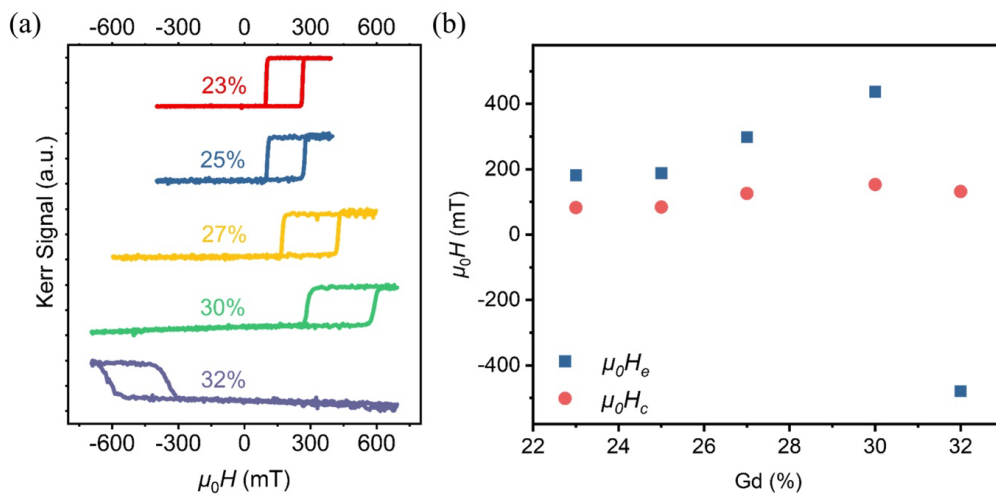


Fig. 6.5 (a) The hysteresis loops with various Gd concentrations (from 23% to 32%). (b) Evolution of exchange bias field $\mu_0 H_e$ and coercivity $\mu_0 H_c$ as a function of Gd concentration.

We have studied the magnetic properties of the IrMn/CoGd bilayer structure at various temperatures. The magnetization of Co and Gd sublattices vary with temperature, consequently altering the net magnetic moment exhibited by CoGd to the external environment. The temperature at which the net magnetic moment becomes zero is referred to as the temperature compensation point of CoGd. In our study, the IrMn/CoGd samples are deposited with Gd concentrations of 23%, 27%, 30%, and 32%. By employing SQUID-VSM, we extracted the coercivity and exchange bias fields at different temperatures from the obtained hysteresis loops, as shown in Fig. 6.6. Taking the Gd 23% sample as an example, both the coercive field and the exchange bias field increase as the temperature approaches the temperature compensation point (approximately 140 K), similar to approaching the component compensation point. Additionally, it is evident that the exchange bias field changes direction on either side of the temperature compensation point. This reversal is attributed to the switching of the net CoGd magnetic moment across the compensation point, while the IrMn interface remains stable[115]. For samples with Gd concentrations of 27%, 30%, and 32%, we similarly determined their temperature compensation points to be approximately 210 K, 250 K, and 320 K, respectively.

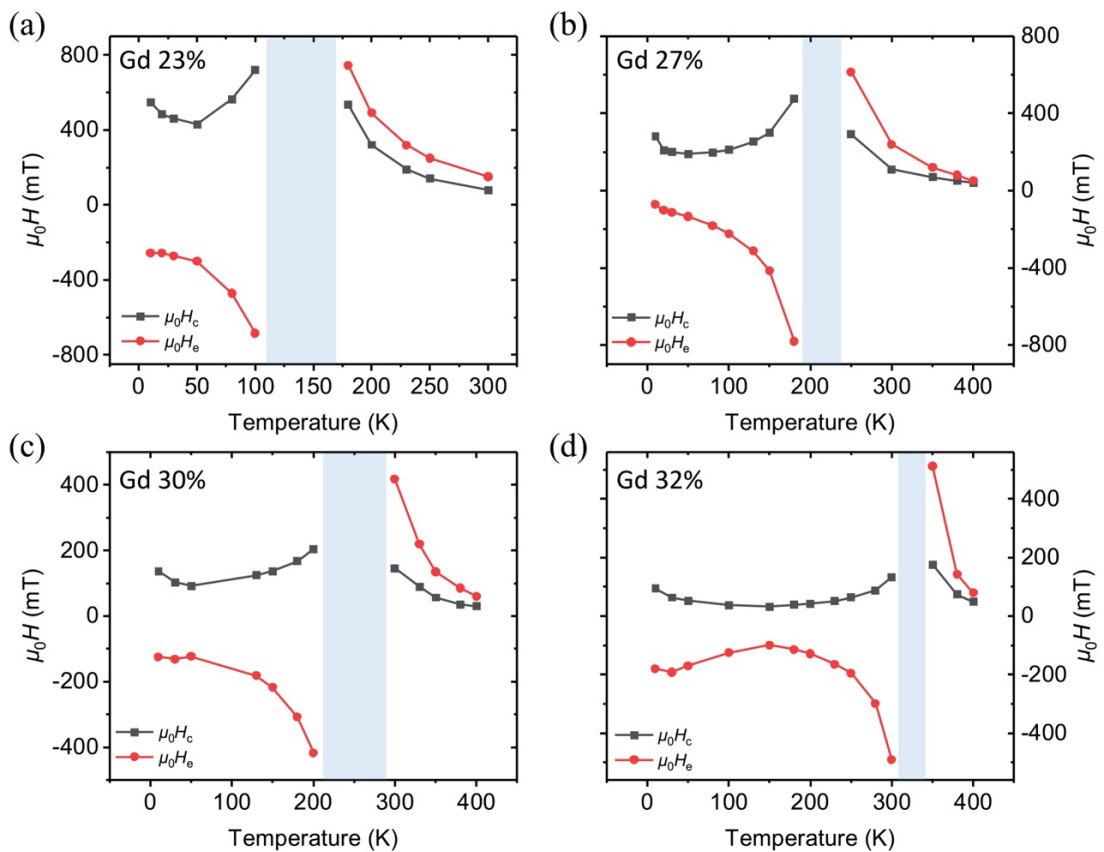


Fig. 6.6 Variation of exchange bias field and coercive field with temperature in IrMn/CoGd samples with Gd concentration of (a) 23%, (b) 27%, (c) 30%, and (d) 32%, and the temperature compensation points of the corresponding samples can be obtained by the sign of the exchange bias field and the magnitude of the coercive field as ~140 K, ~200 K, ~250 K, and ~300 K, respectively.

6.2 Single-shot laser-induced exchange bias switching

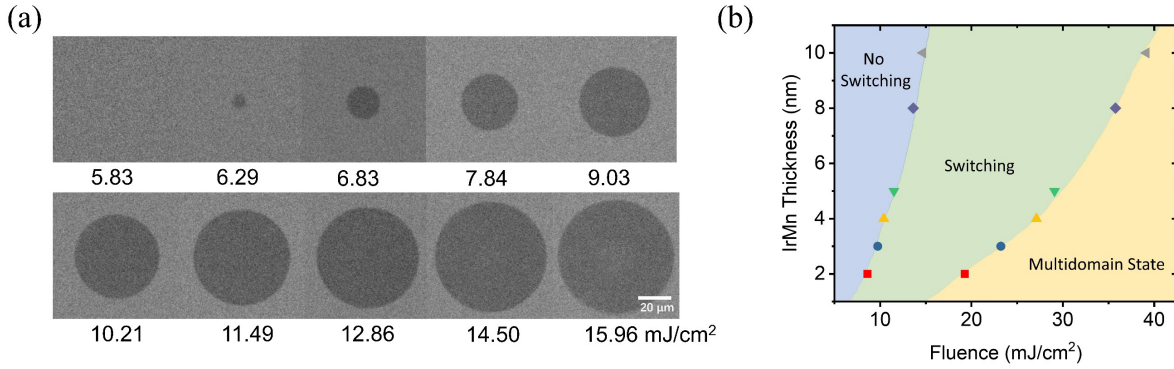


Fig. 6.7 (a) The Kerr images of the AO-HIS with various laser fluence in IrMn (2.0)/Co₇₇Gd₂₃ (4.0). The switching threshold is 5.83 mJ/cm² and the demagnetization fluence is 14.5 mJ/cm². (b) The AO-HIS state diagram of laser fluence in IrMn (t_{IrMn})/Co₇₇Gd₂₃ (4.0) with various IrMn thicknesses.

The AO-HIS is highly sensitive to the concentration of ferrimagnet, and different capping or buffer layers affect the compensation point[116]. Therefore, keeping the same interface conditions in our AFM/FiM multilayers is essential. For reference, we used the IrMn (2.0)/Co₇₇Gd₂₃ (4.0) sample with near-zero exchange bias to perform the AO-HIS. The Kerr images obtained at various laser fluences are presented in Fig. 6.7(a). Additionally, we have summarized the switching region (ranging from the switching threshold to the multidomain state) of the laser fluence at different IrMn thicknesses, as shown in Fig. 6.7(b). We observed that the switching region of the fluence becomes larger with increasing IrMn thickness, which is related to the different laser energy absorption configurations.

We selected the IrMn (5.0)/Co₇₇Gd₂₃ (4.0) sample for the detailed all-optical switching and exchange bias switching experiments. Because 5 nm IrMn exhibited a high exchange bias field and a relatively low coercivity. The laser pulse used in the experiment had a pulse width of 40 fs and a laser fluence of 17 mJ/cm², which is shining on the CoGd side (Fig. 6.8(a)). By

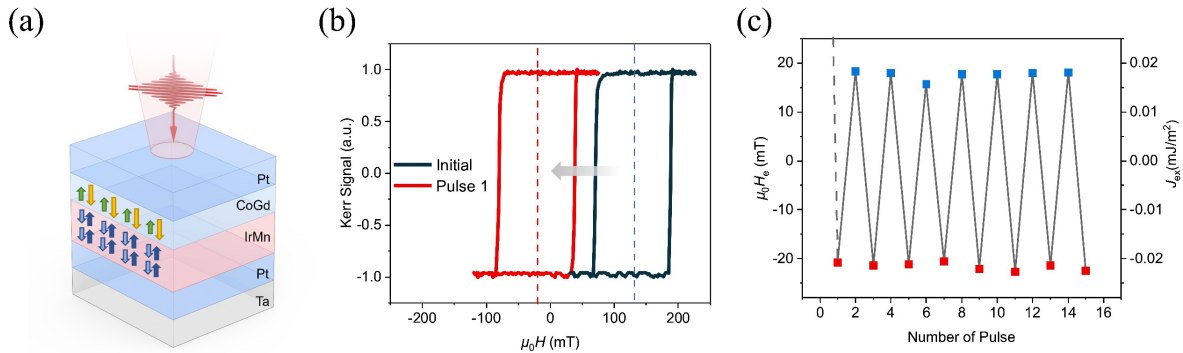


Fig. 6.8 Evolution of the exchange bias using a single femtosecond laser pulse. (a) Sketch of the film stack and the laser incident beam. (b) Hysteresis loop of IrMn(5.0)/Co₇₇Gd₂₃(4.0) before and after exposure to a single linearly polarized laser pulse with a pulse duration of 40 fs and a fluence of 17 mJ/cm² (c) Modulation of the exchange bias field as a function of the number of pulses with a pulse duration of 40 fs and a laser fluence of 17 mJ/cm².

analyzing the hysteresis loops before and after laser irradiation (Fig. 6.8(b)), it was observed that the exchange bias switched from an initial value of 154 mT to -26 mT as the CoGd switching. The result indicated a significant reduction of the exchange bias field compared to the initial state after annealing. However, with continuous excitation of the laser pulse (Fig. 6.8(c)), the exchange bias field could repeatedly switch between ± 20 mT. This repetitive exchange bias switch suggests that the ultrafast interfacial antiferromagnetic spin dynamics can be realized through exchange coupling with CoGd.

Fig. 6.9(a) shows the AO-HIS Kerr images of IrMn (5.0)/Co₇₇Gd₂₃ (4.0) bilayer with various laser fluences. The light grey region is the unswitched area with an initial exchange bias. The black circle is the switched region shined by a single femtosecond laser pulse. We can note that the switching threshold is 11.9 mJ/cm² and become a multidomain state over 29.4 mJ/cm². The switching of CoGd and exchange bias are closely related to the temperature gradient induced by Gaussian-distributed laser fluence. Fig. 6.9(b)(c) shows the evolution of the exchange bias field and the coercive field of IrMn (5.0)/Co₇₇Gd₂₃ (4.0) bilayer as a function of the distance from the spot center for various laser fluences. Before switching, the exchange bias rapidly reduces in the spot center; over the switching threshold of 11.25 mJ/cm², the exchange bias sign changes.

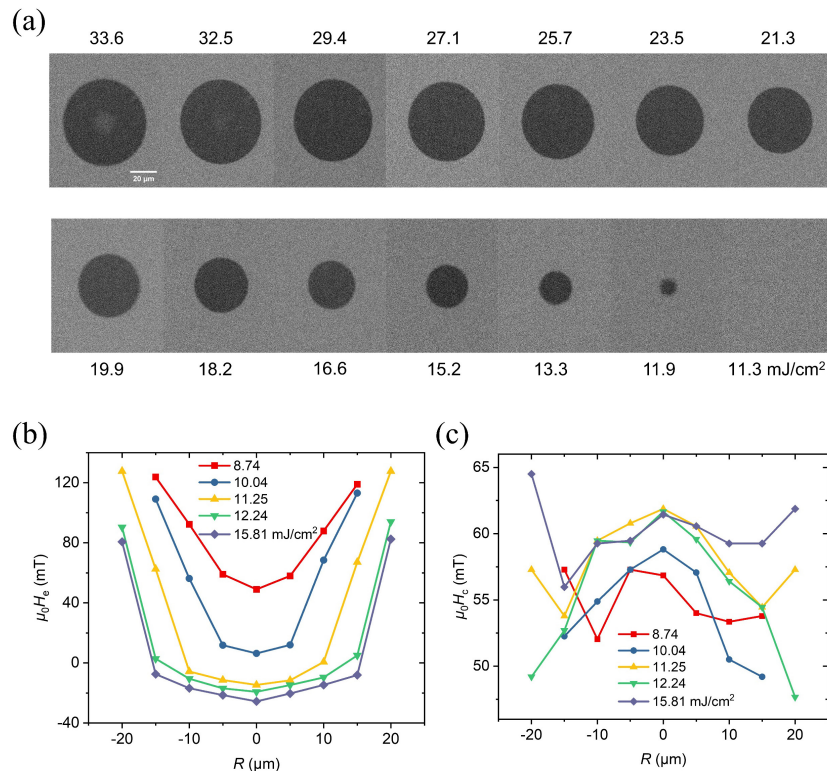


Fig. 6.9 (a) Kerr images of IrMn (5.0)/Co₇₇Gd₂₃ (4.0) after shine to a single linearly polarized laser pulse with various fluences ranging from 11.3 to 33.6 mJ/cm². (c)(d) Exchange bias field $\mu_0 H_e$ and coercivity $\mu_0 H_c$ as a function of the position (R) from the centre of the laser spot at various laser fluences.

We then investigated the laser fluence and IrMn thicknesses dependences of the induced exchange bias modification. As shown in Fig. 6.10(a), independently of the IrMn thickness for t_{IrMn} between 4 and 10 nm, a rapid reduction of $\mu_0 H_e$ is observed at low fluences (related $\mu_0 H_c$ is shown in Fig. 6.10(b)). It then reverses and increases for medium fluence excitation before saturating or even decreases towards zero at high fluence. First of all, the change of the $\mu_0 H_e$ sign can be closely related to the AO-HIS of CoGd magnetization by a single pulse (dashed line in Fig. 6.10(a)). Indeed, the switching of the CoGd is a precondition for reversing the interfacial magnetization that imprints the interfacial spin configuration in the IrMn during cooling. Second, starting from the positive exchange bias obtained using thermal annealing under an applied magnetic field, the intensity of the maximum negative exchange bias observed after one pulse is always smaller. Depending on the IrMn thickness, 13% to 33% of the initial exchange bias field can be obtained with t_{IrMn} decreasing from 10 to 4 nm respectively, as shown in Fig. 6.10(a) inset. The two-temperature model included in the atomistic simulations explains the ultrafast dynamics process for the IrMn/CoGd system. The simulation results show that, after the laser heats the sample, the temperature of the nanoscale IrMn grains exceeds the Néel temperature (around 700 K) and switches according to the AO-HIS of the CoGd layer. After the lattice temperature cools down to below the blocking temperature, the incomplete exchange bias reversal indicates that under such an ultrafast switching process, the recovery of the AFM order is not fully deterministic and thus does not allow the spin structure to rearrange fully. The thicker the IrMn layer is, the smaller the amplitude of the reversed exchange bias field is. Both situations arise due to the weaker effective exchange coupling on the antiferromagnet it is harder to orient the IrMn grains.

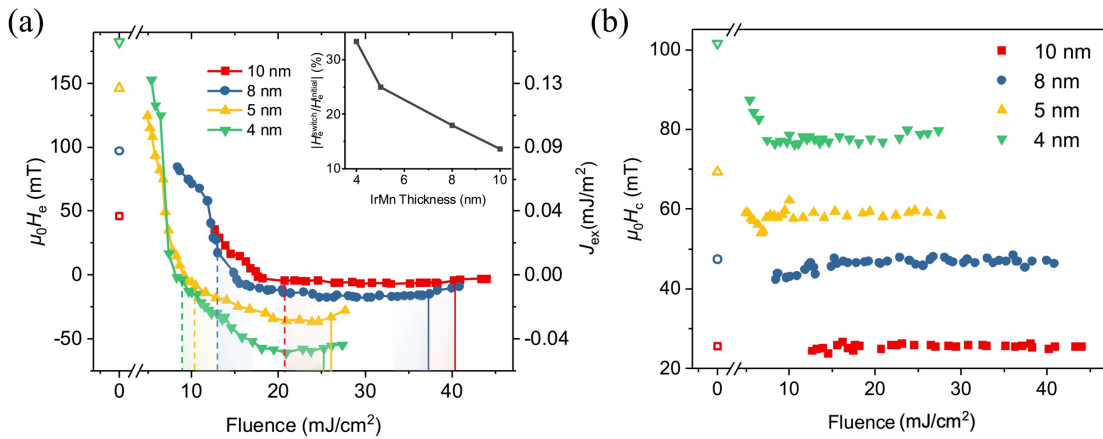


Fig. 6.10 (a)(b) Evolution of $\mu_0 H_e$ and $\mu_0 H_c$ after one single laser pulse as a function of the laser fluence. The dashed line indicates the CoGd switching threshold, and the solid line indicates the demagnetization threshold. The hollow symbols at 0 mJ/cm^2 indicate the initial $\mu_0 H_e$ of each IrMn thickness.

6.3 Exchange bias manipulation with multi-pulses

To allow the spin structure to rearrange thermally, we induced heating using low fluence laser pulses, with fluences much lower than the threshold fluences needed to reverse the CoGd

magnetization. After the CoGd switching with a single laser pulse of 17 mJ/cm^2 on the IrMn(5.0)/Co₇₇Gd₂₃(4.0) sample, low fluence laser pulses of 8.2 mJ/cm^2 were applied on the switched region. As the pulse number increases, regardless of whether CoGd magnetization and exchange bias field are in parallel (P) or antiparallel (AP) states, the exchange bias recovers to $\pm 76 \text{ mT}$ along the CoGd magnetization direction as illustrated in Fig. 6.11(a) (related coercivity $\mu_0 H_c$ is illustrated in Fig. 6.11(b)). The same behavior is observed for the 8 nm IrMn sample (Fig. 6.11(c)(d)). The prolonged heating generated by low fluence multi-pulses allows the AFM layer spins to further reorder and increase $\mu_0 H_e$. However, this process still does not allow reaching the initial exchange bias because the cooling time after the laser pulse is around 500 ps compared to the long annealing time and applied field, both of which allow the development of a larger exchange bias field through relaxation over energy barriers at equilibrium.

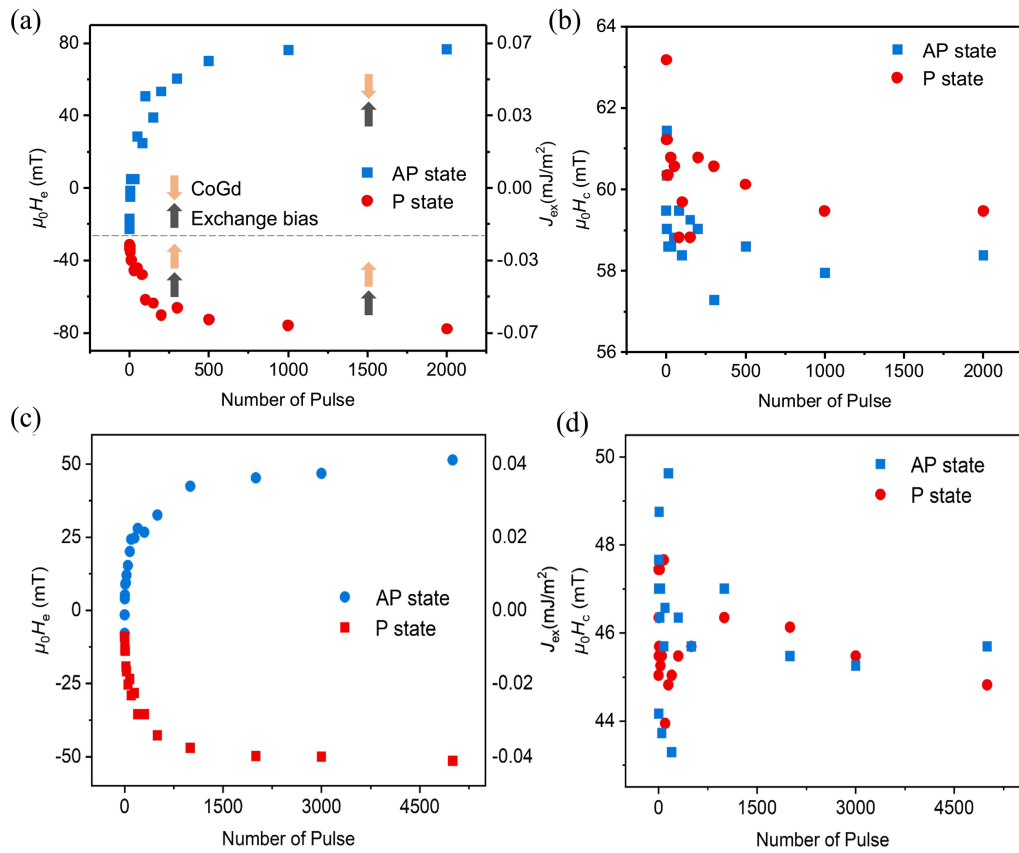


Fig. 6.11 After the exchange bias switching was achieved using a high-fluence single-pulse laser, the same position was irradiated with a low-fluence laser of 8.2 mJ/cm^2 (4 nm IrMn) and 12.4 mJ/cm^2 (8 nm IrMn) at different numbers of pulses, (a)(c) the exchange bias of 4 and 8 nm IrMn samples increases with the number of the pulses and (b)(d) the coercivity of 4 and 8 nm samples decreases with the increase of the number of pulses.

However, the multi-pulses and longtime heating still do not allow for reaching the initial exchange bias. Then, we focused on the laser fluence of the multi-pulse. We applied 2000 pulses with various laser fluences, which shone on the initial annealing state and the AP or P state after single-shot switching, respectively. The corresponding results of the exchange bias field and coercive field are depicted in Fig. 6.12. We observed that from the initial state after annealing,

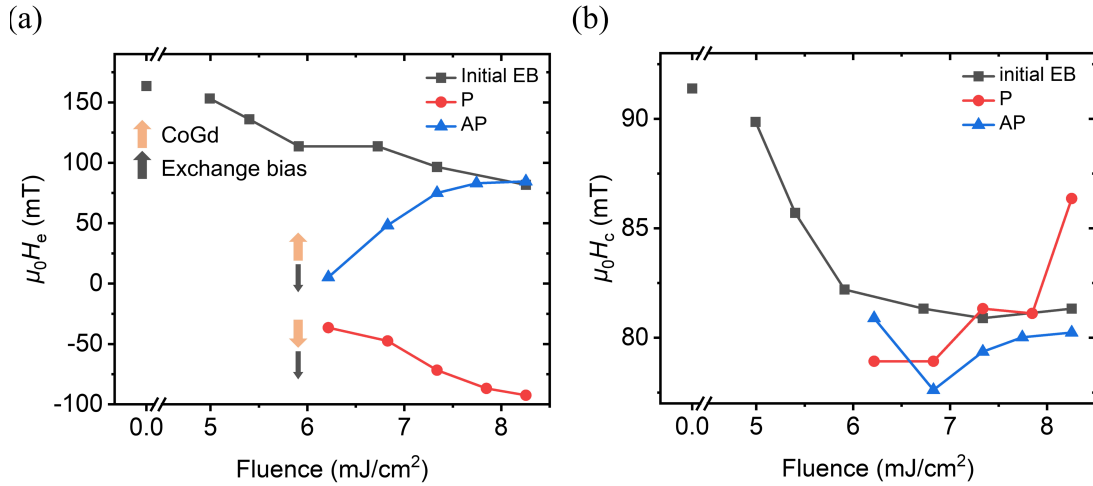


Fig. 6.12 Evolution of $\mu_0 H_e$ (a) and $\mu_0 H_c$ (b) after 2000 pulses as a function of the laser fluence, which shining on the initial annealing state and the AP or P state after single-shot switching with 15.5 mJ/cm², respectively.

the exchange bias field gradually reduced as the laser fluence increased. Conversely, in AP and P states after a single laser pulse, the exchange bias field progressively increases and eventually stabilizes at ± 76 mT, which indicates that rising laser fluence of the multi-pulse laser significantly accelerates the recovery of the substantially weakened exchange bias field. It's worth noting that at the laser fluence of 8.2 mJ/cm², the same exchange bias field is achieved in all three scenarios, which indicates that the final exchange bias field is only influenced by the heating and cooling processes induced by the multi-pulse laser.

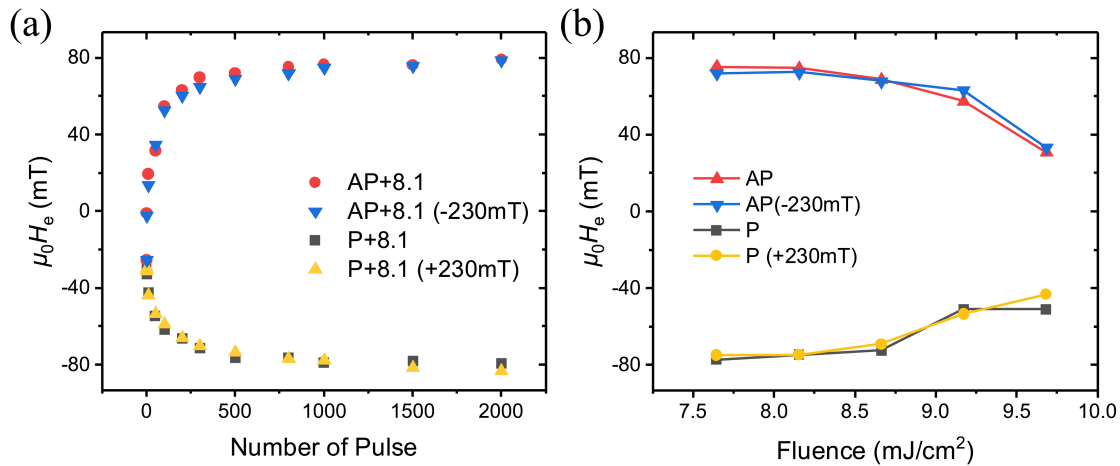


Fig. 6.13 (a) Evolution of $\mu_0 H_e$ as a function of the laser pulse numbers with or without applied external field. (b) Evolution of $\mu_0 H_e$ after 2000 pulses as a function of the laser fluence with or without applied external field.

In order to further simulate the field annealing process, we applied a magnetic field when shining the multi-pulse laser. As depicted in Fig. 6.13(a), regardless of the presence or absence of an applied magnetic field, the exchange bias field recovered to ± 76 mT with the increased

pulse numbers exhibited similar trends from the AP or P initial states. Furthermore, in Fig. 6.13(b), as the laser fluence approached the switching threshold of CoGd, the IrMn spin at the interfaces was progressively influenced by the demagnetization of CoGd, which led to a decrease in the exchange bias field. Similarly, the external magnetic field has no impact on the exchange bias field after laser irradiation, which suggests that the exchange bias is stable with a cooling of hundreds of picoseconds compared to the long-time annealing and applied field, both of which allow the development of a larger exchange bias field through relaxation over energy barriers at equilibrium.

6.4 Timescale for exchange bias switching

Since exchange bias can be manipulated using a single femtosecond laser pulse, the next question that needs to be answered is how long it takes to modify the exchange bias field and, consequently, the IrMn magnetic configuration at the interface? Several reports have suggested that photoexcitation of the AFM/FM interface induces significant modulations in the exchange bias field on ultrashort timescales[124][126]. Detailed time-resolved studies of dynamics showed that the characteristic timescale of laser-induced exchange bias quenching in a polycrystalline Co/IrMn bilayer is 0.7 ± 0.5 ps, attributing the rapid decrease in exchange coupling to a spin disorder at the interface created by laser heating[124].

In our case, the demagnetization and switching dynamics after a 40 fs laser pulse illumination of the annealed IrMn(5.0)/Co₇₇Gd₂₃(4.0) sample have been studied as a function of time for various laser fluences (Fig. 6.14 (a)) and for different applied fields intensities (Fig. 6.14(b)). A Co demagnetization time of ~ 700 fs could be measured, which is independent of the applied field. We observe that for pump laser fluence larger than 11.7 mJ/cm², the magnetization switching is observed in CoGd alloy. The full reversal requires a typical time of ~ 5 ps. Since a constant magnetic field is applied to reset the CoGd magnetization state in the TR-MOKE

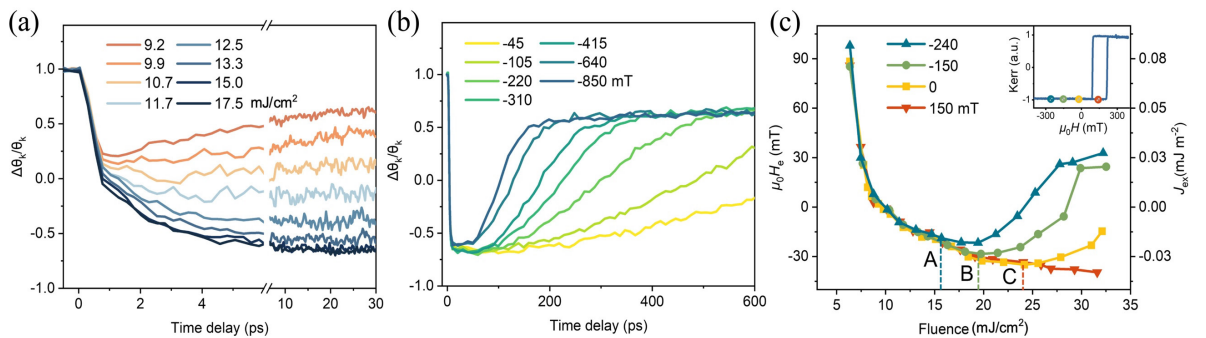


Fig. 6.14 The CoGd switching and exchange bias dynamic under an external field in IrMn (5.0)/Co₇₇Gd₂₃ (4.0). (a) CoGd dynamics as a function of time for different laser fluences under an applied field of -220 mT. The demagnetization time is ~ 700 fs and the magnetization switching time is ~ 5 ps. (b) CoGd dynamics for a laser fluence of 17.5 mJ/cm² under various external fields. (c) Evolution of $\mu_0 H_e$ after one single laser pulse as a function of the laser fluence under various external fields. The inset shows the hysteresis loop and marks the applied external field of IrMn (5.0)/Co₇₇Gd₂₃ (4.0) sample.

measurement, the exchange bias field only switched after the first laser pulse and the interfacial IrMn maintains its magnetization orientation during the sequential laser excitation. We can only obtain the magnetic dynamics of CoGd without exchange bias switching, meanwhile, the presence of IrMn does not seem to change the dynamics of the ferrimagnetic layer as it was already reported in the case of NiMn layer[126]. At long timescales, the CoGd layer switches back to its initial magnetization orientation because of the presence of an external magnetic field. Fig. 6.14(b) shows that the larger the magnetic field, the faster the CoGd switches back, which can be explained using the time evolution of a macrospin state under the applied field[127]. We can especially note that for an applied field of -220 mT, it takes ~500 ps for the magnetization to cross zero again towards positive magnetization after achieving a full reversal.

The single pulse evolution of the exchange bias has been studied as a function of the laser fluence for different applied fields as shown in Fig. 6.14(c). We note that, due to the combination of laser heating and CoGd switching back under the negative applied field, the exchange bias field begins to recover at the larger laser fluences. By comparing the CoGd dynamics at the corresponding external field in Fig. 6.14(b), we can deduce the longest timescale where the exchange bias can be set. For low fluence and up to 16 mJ/cm^2 (see point A in Fig. 6.14(c)), the exchange bias is independent of the applied field in the field range +150 mT/-240 mT. Since we can observe that at those fields, the reversed CoGd state is preserved up to 100 ps, we can conclude that exchange bias is switched and set within 100 ps. When increasing the fluence, the bilayers are more strongly affected by the applied field as can be seen in Fig. 6.14(c). For point B (18 mJ/cm^2 with -150 mT), the exchange bias is increased due to the thermal heating of the antiferromagnet above the blocking temperature and cooling in an applied field, thus resetting some of the switched grains. For fluences larger than 24 mJ/cm^2 (point C), the exchange bias field no longer increases under zero applied field and even tends towards zero as the fluence increases. At those fluences, the CoGd no longer switches but demagnetizes as suggested by the state diagram measured by Wei et al[128]. Consequently, a demagnetized state is imprinted in the IrMn at the interface, so that the exchange bias is close to zero. However, with an applied field, either positive or negative exchange bias can be reached depending on the sign of the applied field, similar to conventional exchange bias setting.

6.5 Atomistic simulation of antiferromagnetic dynamics

To gain further insight into the exchange bias switching and the dynamics of IrMn magnetic moments with a single femtosecond laser, we applied atomistic simulations with VAMPIRE software package[129][130]. A bilayer structure of IrMn/CoGd was constructed, as depicted in Fig. 6.15. The CoGd layer was designed as an amorphous alloy, while a polycrystalline grain structure was implemented for IrMn to better replicate experimental conditions. Additionally, the simulation considered interfacial elemental intermixing to simulate the diffusion of elements during annealing and at high temperatures.

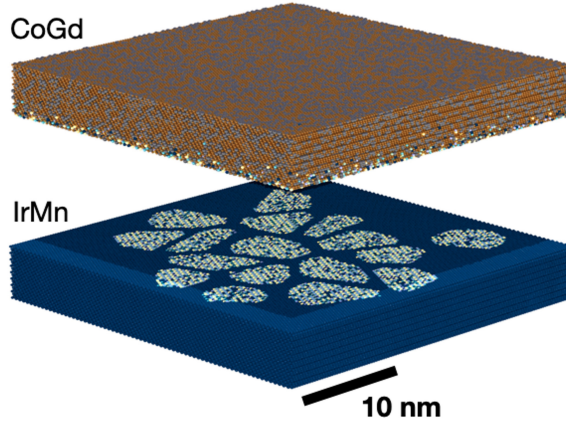


Fig. 6.15 Visualization of the simulated system $30 \times 30 \times 10$ nm showing the granular nature of the IrMn.

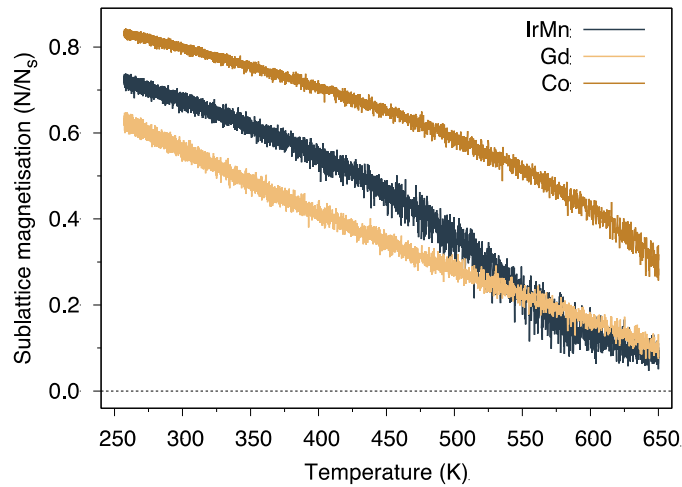
We use an atomistic spin model to simulate the equilibrium and dynamic properties of the IrMn/CoGd bilayer. The energetics of the system are described by a spin Hamiltonian of the form:

$$H = - \sum_{i < j} J_{ij} S_i \cdot S_j - \sum_i k_u S_i^z{}^2 - \sum_i k_N (S_i \cdot e_{ij})^2 - \sum_i \mu_i S_i^z B^z \quad (5.1)$$

Where $S_{i,j}$ is a unit vector describing the direction of spin i, j , J_{ij} is the exchange energy between atoms i, j , k_u is the uniaxial anisotropy on the Co and Gd sites, k_N is the Néel pair anisotropy between the Mn sites and B^z is the external applied magnetic field. The model parameters are listed in Table 1. The equilibrium properties and field cooling are simulated with an adaptive Monte Carlo metropolis model with adaptive move and dynamics are computed using the stochastic Landau-Lifshitz-Gilbert equation with Langevin dynamics. The temperature rise induced by the laser pulse is modeled by coupling the spin system to the two-temperature model augmented with a cooling term to reproduce the cooling effect of the substrate. The parameters for the atomistic simulations are listed in Table 6.1, drawn from a range of previous publications developing models of IrMn and CoGd alloys. The Mn-Gd exchange coupling is assumed to be weak, based on the Curie temperature (seen from the divergence in specific heat) of a $Gd_{30}Mn_{70}$ alloy around 30% of the bulk Gd Curie temperature, suggesting a weak effect from the Mn.

Quantity	Material	Value	Unit	Reference
NN exchange	Mn	-6.4×10^{-21}	J	[63][64]
NNN exchange	Mn	5.1×10^{-21}	J	[63][64]
Interlayer exchange	Mn-Co	1.2×10^{-21}	J	[61][62]
Interlayer exchange	Mn-Gd	2.4×10^{-22}	J	[134]
NN exchange	Co-Co	3.9×10^{-21}	J	[132][133]
NN exchange	Gd-Co	-1.25×10^{-21}	J	[132][133]
NN exchange	Gd-Gd	1.26×10^{-21}	J	[132][133]
Néel pair anisotropy	Mn	-4.22×10^{-22}	J	[61][62]
Anisotropy Constant	Co	1.865×10^{-23}	J	[132][133]
Anisotropy Constant	Gd	4.035×10^{-24}	J	[132][133]
Magnetic moment	Mn	2.6	μB	[61]
Magnetic moment	Co	1.61	μB	[132][133]
Magnetic moment	Gd	7.63	μB	[132][133]
Gilbert damping	Mn	0.02	...	[62]
Gilbert damping	Co	0.02	...	[132][133]
Gilbert damping	Gd	0.02	...	[132][133]

Table 6.1 Parameters for the atomistic simulation with associated references.

Fig. 6.16 Field cooling Monte Carlo (MC) simulation showing magnetic ordering of the system and Néel temperature of 600 K during the field-cooling procedure over 8×10^6 steps.

To initialize the system in an exchange-biased state, we perform a field-cooling procedure, starting above the blocking temperature of the IrMn $T = 650$ K and cooling to above the compensation point, just below room temperature at $T = 240$ K. A large setting field of $B = 10$ T is applied to align the Co sublattice and interfacial Mn moments in the $+z$ direction. The simulation is performed by a Monte Carlo simulation with adaptive moves and a total of 10^8 steps to allow the system to achieve an equilibrium state at all temperatures. The temperature-dependent magnetization of each material in the system is provided by the field cooling atomistic simulation with an external field as -10 T. From the results in Fig. 6.16, the Curie temperature of the CoGd is much larger than the IrMn due to the small grain size and enhanced finite size effects. After the field cooling procedure, the system is relaxed in zero field before simulated illumination with a laser pulse.

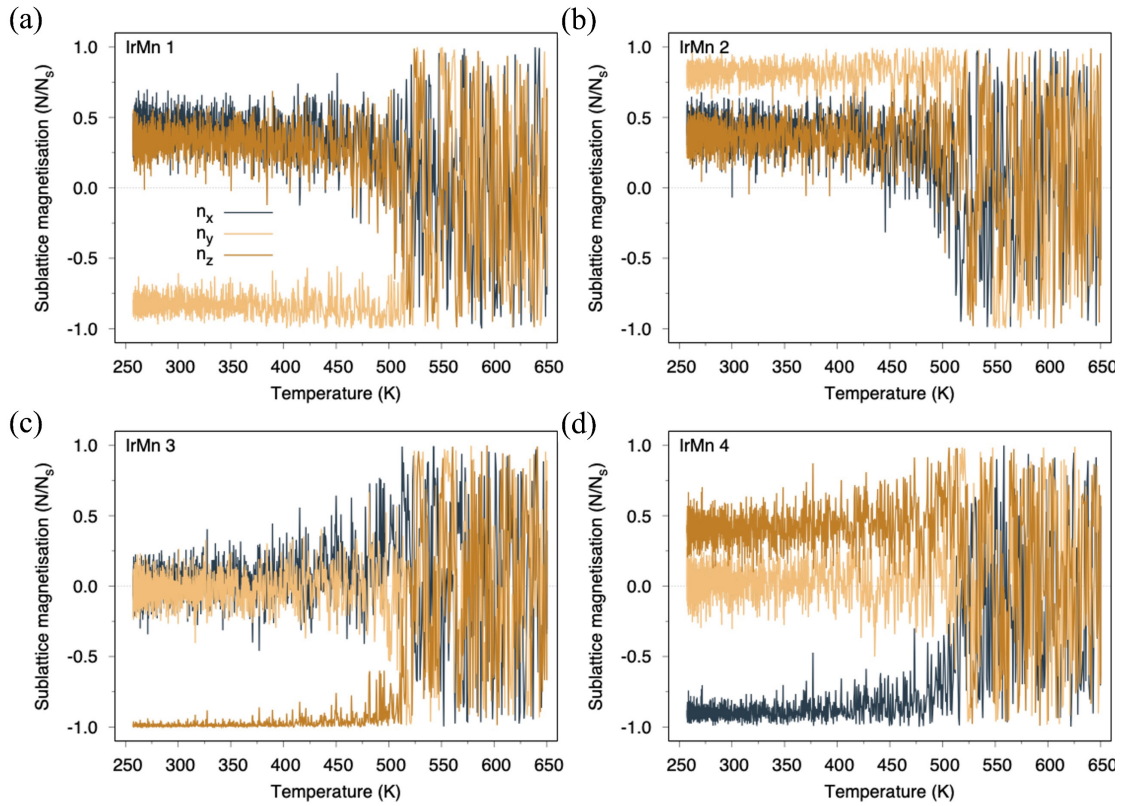


Fig. 6.17 (a)-(d) Field cooling simulations of a single 5 nm IrMn grain for each of the four magnetic sublattices, showing a stable configuration for $T < 500$ K, suggesting a blocking temperature around $T = 500$ K for nanosecond timescales.

To show the setting of the grains we show the temperature-dependent sublattice magnetization for grain 1 during the field cooling procedure in Fig. 6.17(a). Here there are 8 possible ground states of the magnetization corresponding to the different easy axes of the cubic crystal. In the (111) crystal orientation one of the sublattices aligns along the $\pm z$ direction, corresponding to the degree of coupling with the Gd or Co sublattice. For grain 1, this corresponds to the sublattice with the largest number of moments at the IrMn/CoGd interface aligning antiparallel with the Co, indicating stronger coupling to the Gd sublattice. In this case, it is sublattice 3 in Fig. 6.17(c).

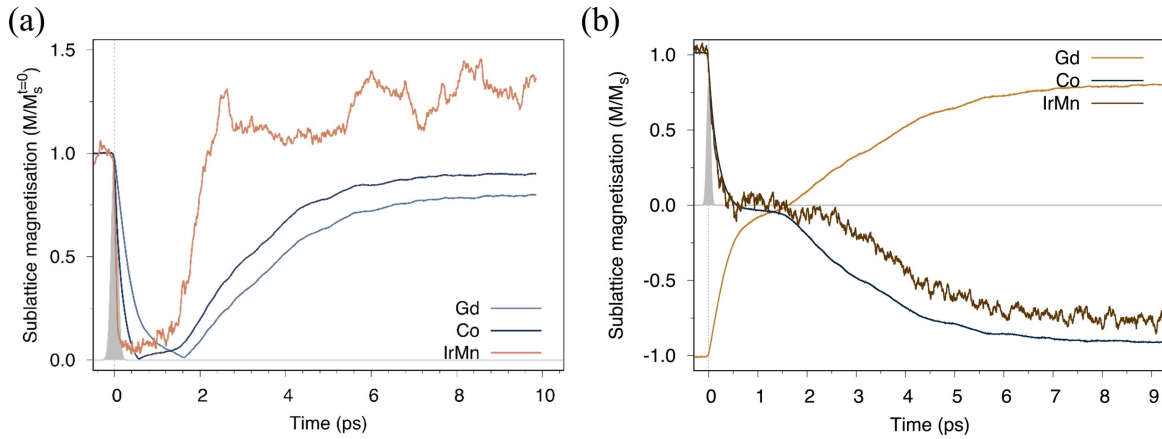


Fig. 6.18 (a) Ultrafast demagnetization of the Gd, Co and IrMn sublattices, showing distinct demagnetization times for each sublattice. (b) Ultrafast switching of the net magnetization of the Gd, Co and IrMn sublattices. The CoGd reverses by thermally induced switching caused by laser heating, while the reversible Mn moment (polarized by the Co) follows the Co magnetization on a slightly longer timescale than the switching.

Fig. 6.18(a) shows the dynamic response of the Gd, Co, and Mn sublattice moments to a 40 fs laser pulse simulated using the two-temperature model, showing ultrafast demagnetization at three distinct timescales. The difference in ferromagnetic demagnetization rates is due to the different magnetic moments and effective damping constants, but the demagnetization of the antiferromagnet is even faster than a ferromagnet with a characteristic timescale of only 15 fs, despite the larger moment of $2.6 \mu_B$ / Mn site. The ultrafast dynamics in antiferromagnets is due to the high frequency optical spin-wave modes available due to the strong antiferromagnetic exchange coupling. At short timescales, the IrMn demagnetizes in the first 0.2 ps, and then fluctuates strongly, while some grains fully switch after 0.5 ps following the Co/Gd magnetization respectively. In Fig. 6.18(b), we show the role of ultrafast heating on the system, showing demagnetization and thermally induced switching of the CoGd and ultrafast disordering of the antiferromagnet, followed by a slow recovery of the total IrMn magnetization parallel to the Co magnetization, while each grain remagnetizes to a single domain state in only 2 ps. Due to the rapid heating, the IrMn grains enter a superparamagnetic regime where the orientations of the four distinct antiferromagnetic sublattices fluctuate on the sub-picosecond timescale immediately after the laser pulse.

Fig. 6.19 shows the time-dependent magnetization for the IrMn sublattice set in the perpendicular $\pm z$ direction by the field cooling procedure, in the perpendicular $\pm z$ direction for 5 characteristic grains. In γ -IrMn₃ there are four distinct sublattices and switching of the antiferromagnet can occur by a full 180° reorientation (I) or by a 109.5° reorientation (II, III, IV) into one of the other three orientations with opposite z-orientation $S_z \sim 0.86$. This partial reorientation is one of the reasons for a reduced perpendicular exchange bias. Each grain has a random coupling to the Co and Gd sublattices, meaning that around half of the grains are set parallel to the Co, and half are set parallel to the Gd magnetization. Switching is indicated by a full perpendicular re-orientation of the IrMn after the pulse.

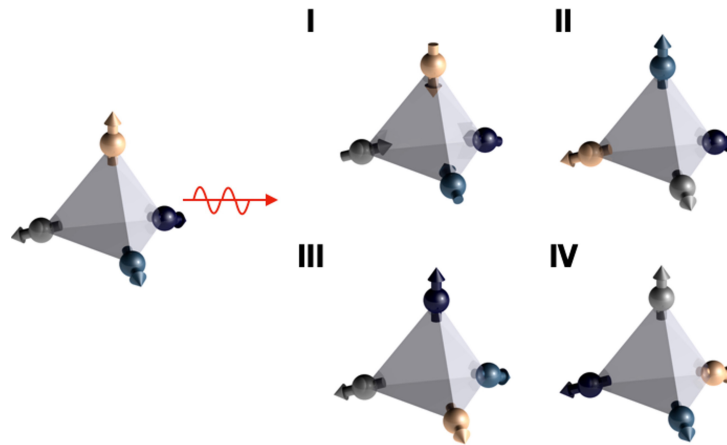


Fig. 6.19 Schematic of the switching process, showing reorientation of the Mn sublattice responsible for the exchange bias.

In Fig. 6.20, the data indicate a coherent ultrafast switching process on the short timescale of ~ 1.5 ps, but after this initial switching many grains form a multidomain state indicating a switched interface but re-nucleation of the grain order in a different magnetic state. This reduces the effective switching probability due to the formation of an indeterminate orientation of the grains, with $n_z \sim 0$ after the pulse. The data shows all grains form a single domain state but not in a well-defined energy minimum, thus the final state will be random, and these grains will not contribute to the exchange bias after the pulse. As the IrMn responds extremely quickly to the laser reaching a spin temperature above the Néel temperature, there are no progressive effects with sequential laser pulses. Thus, the exchange bias is set by the Co direction of each pulse at $t = 1.5$ ps after the pulse.

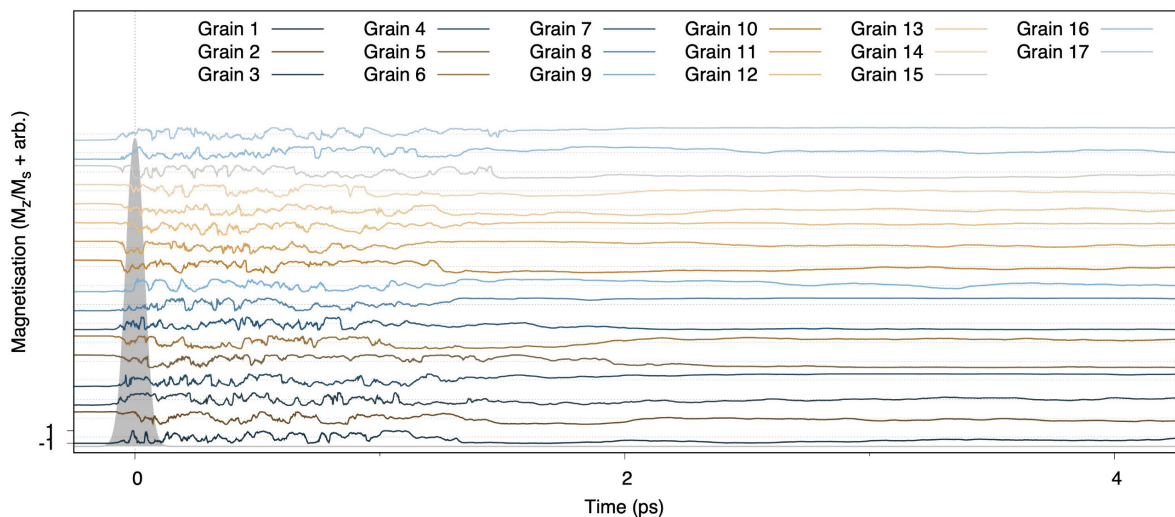


Fig. 6.20 Ultrafast switching of the perpendicular moment of each grain in the system. Individual response of the z-component of the IrMn sublattice magnetization of each grain showing a coherent switching process 1.5-2 ps after the pulse, before achieving a stable state at longer timescales. The sublattice chosen for each grain is the one that is set in the perpendicular direction ($\pm z$).

Grains	Switch after pulse 1 (1.5 ps)	Switch after pulse 1 (long timescale)	Switch after pulse 2 (1.5 ps)	Switch after pulse 2 (long timescale)
1	N	N	N	Indeterminate
2	Y	Y	N	N
3	N	Indeterminate	Y	Indeterminate
4	Y	Y	Y	N
5	N	Y	Y	N
6	Y	Indeterminate	N	N
7	N	N	Y	Y
8	Y	Y	Y	N
9	Y	Indeterminate	N	N
10	Y	Indeterminate	Y	Y
11	N	Indeterminate	N	Indeterminate
12	Y	Indeterminate	Y	Indeterminate
13	Y	Indeterminate	N	Y
14	Y	Y	N	Indeterminate
15	Y	Y	Y	Y
16	Y	Indeterminate	N	Y
17	Y	Y	Y	Y
Switching probability	70.5 %	41.2 %	53 %	35.3 %

Table 6.2 Switched and final state of the grains after the first and second laser pulses.

The simulations indicate a complex process for IrMn switching that is probabilistic, as shown in Table 6.2, all the grains lose their previous configuration information after each pulse, but a certain percentage of grains align with the Co/Gd magnetization after each pulse, which resulted in the reduction of the exchange bias. The final switching probability represents the exchange bias change at different times after the pulse, taking into account the indeterminate grains. There is no particular correlation between switched and unswitched grains suggesting a random process for each grain switching. The small sample size of 17 grains gives a large error estimate $\sim \sqrt{17} \sim 25\%$ on the switching probability and so we believe that the process is independent of pulse number.

The single shot exchange bias switching can be seen as an ultrafast thermal annealing, where the IrMn grains are heated above the Néel temperature and then experience superparamagnetic relaxation above the blocking temperature of the grains. The resetting of the exchange bias by cooling through the blocking temperature in the exchange field from the Co is not significant on the sub-nanosecond timescales of the experiment as seen through the need for multiple pulses. Therefore, the short timescale coherent switching process of the IrMn must play an important role in the single shot switching seen experimentally. However, the large heating after the pulse partially overwrites the switching process causing a less than 100% switching probability, but this is independent of the number of pulses and simply follows the magnetization of the Co/Gd sublattices. Essentially each pulse acts as a reset for the IrMn magnetization where the remagnetization follows the direction of the Co/Gd, but there are no progressive effects as the IrMn is completely demagnetized after each pulse.

6.6 Summary

In this chapter, we have studied the effect of a single laser pulse on a model perpendicularly exchange bias system IrMn/CoGd bilayers. We have shown that the CoGd magnetization switches in the presence of an interfacial exchange coupling with the IrMn. The value and sign of the exchange bias can be repeatedly controlled with a single femtosecond laser pulse, demonstrating ultrafast reorientation of the antiferromagnetic sublattices. Moreover, only using purely thermal heating, exchange bias can also be modified even with laser fluence below the CoGd switching threshold. Dynamic experiments indicate that the single femtosecond laser-induced exchange bias switching can be done within 100 ps. Atomistic simulations show the ultrafast demagnetization and coherent switching dynamics of the IrMn grains on the ultrafast timescale, switching in less than 2 ps. Our results demonstrate the first single shot switching and repeated control of an exchange-biased antiferromagnet expanding the fundamental understanding and application aspects of exchange bias. The IrMn/CoGd system allows ultrafast, field-free, and energy-efficient control of an exchange-biased antiferromagnet with high ordering temperature and thermal stability, making it highly suited to applications.

Chapter 7.

Ultrafast Antiferromagnet Rearrangement in Co/IrMn/CoGd Trilayers

In this chapter, we demonstrate the manipulation of exchange bias in Co/IrMn/CoGd (FM/AFM/FiM) trilayers with double perpendicular exchange bias using a single femtosecond laser pulse. In quasi-static characteristics, we have shown the IrMn thickness-dependent interlayer interaction of the dual exchange bias interface. With the single femtosecond laser excitation, we find the exchange bias switching is generated from the ultrafast rearrangement of the AFM spins at the IrMn/CoGd interface and further demonstrated the competition across the AFM volume orders. In addition, the high repeatable exchange bias switching of IrMn/CoGd provides an ultrafast and efficient antiferromagnets manipulation method and impacts applications for future spintronic devices.

7.1 Co/IrMn/CoGd double exchange bias trilayer

The Co/IrM/CoGd trilayer structure, similar to the IrMn/CoGd bilayer sample, was grown on a glass substrate using magnetron sputtering. The trilayer systems of the Glass/Ta (5.0)/Pt (5.0)/Co (1.0)/Ir₂₀Mn₈₀ (t_{IrMn})/Co₇₇Gd₂₃ (4.0)/Pt (5.0) (nm) with $t_{\text{IrMn}} = 2$ to 8 nm are shown in Fig. 7.1(a). In the CoGd amorphous layer, we also focus on a Co-rich alloy with a 23% Gd concentration. After deposition, the samples were annealed for 1h at 200 °C in an out-of-plane magnetic field of -60 mT. A series of stepped hysteresis loops are obtained by polar MOKE in Fig. 7.1(b). The exchange bias field $\mu_0 H_e$ and coercivity $\mu_0 H_c$ of both interfaces as a function of the IrMn thickness is presented in Fig. 7.1(c). A noticeable exchange bias field of both interfaces can be observed over the 2 nm IrMn, reaching a maximum at $t_{\text{IrMn}} = 5$ nm and decreasing when t_{IrMn} is further increased. The coercivity $\mu_0 H_c$ decreases with increasing t_{IrMn} . According to Meiklejohn's macrospin model, the effective exchange coupling constant in an FM/AFM bilayer is evaluated using $J_{ex} = \mu_0 H_e M_s t$, where M_s is the saturation magnetization of the CoGd (or Co) layer, which is obtained by SQUID-VSM, and t is the CoGd (or Co) layer thickness. We observe that the nearly compensated CoGd layer exhibits a larger exchange bias field than the Co/IrMn interface at t_{IrMn} between 3 and 8 nm, as illustrated in Fig. 7.1(c). The observed distinction can be ascribed to the different magnetic disorder conditions present at the top and bottom interfaces during deposition[117]. These conditions induce stronger exchange interactions at the IrMn/CoGd interface when the t_{IrMn} is between 3 and 6.5 nm, as shown in Fig. 7.1(d). Additionally, the near-compensated CoGd alloy, characterized by a low M_s , also demonstrates a greater exchange bias field for a comparable J_{ex} at $t_{\text{IrMn}} = 8$ nm.

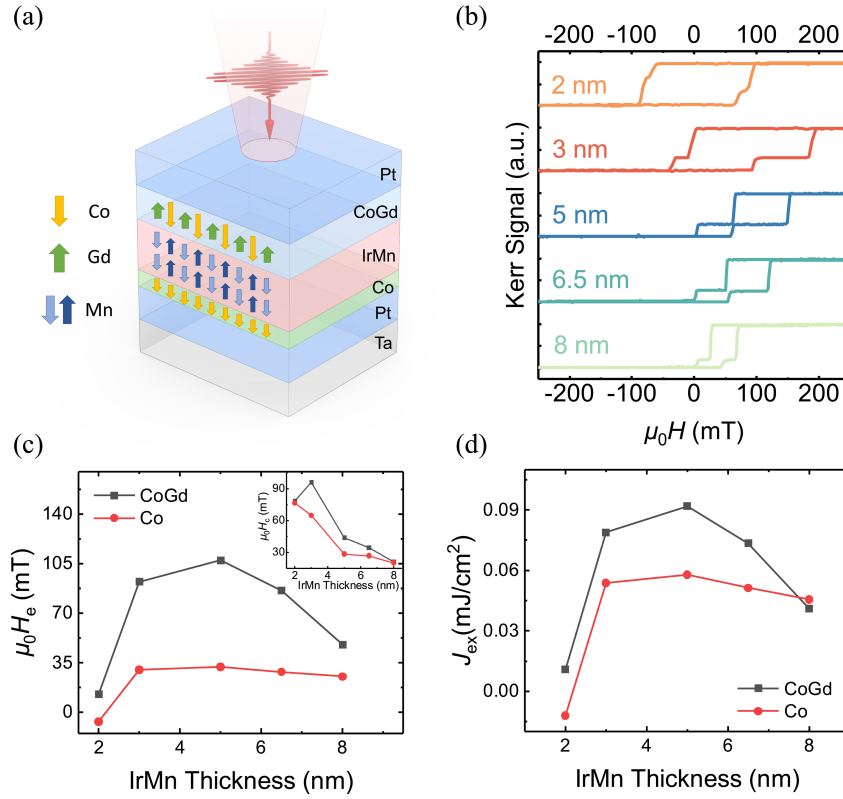


Fig. 7.1 The Co/IrMn/CoGd trilayers magnetic properties characterization. (a) Film stacks structure of Co/IrMn/CoGd perpendicular exchange bias trilayers system. (b) The hysteresis loops at various IrMn thicknesses (t_{IrMn} from 2 nm to 8 nm). Clear stepped hysteresis loops can be obtained at t_{IrMn} from 2 nm to 8 nm. (c) The exchange bias field $\mu_0 H_e$ and coercivity $\mu_0 H_c$ (inset) of CoGd and Co interface as a function of IrMn thickness. (d) The effective exchange coupling constant J_{ex} of both interfaces given by $J_{ex} = \mu_0 H_e M_s t$ as a function of the IrMn thickness (t_{IrMn}).

7.2 Interlayer coupling in Co/IrMn/CoGd

The effect of IrMn layer thickness on the exchange bias field in bilayer systems has been extensively studied[94][95]. Generally, in an IrMn exchange-biased bilayer system, the exchange bias field rapidly increases above the critical thickness (t_c), reaches a maximum (t_{max}), then saturated. This behavior is attributed to the interplay between the interfacial exchange bias and the AFM anisotropy of the IrMn layer. As the thickness of the IrMn layer increases, the interfacial exchange bias becomes less dominant, and the AFM anisotropy of the IrMn layer becomes the primary contributor to the exchange bias field[95]. Consequently, no additional AFM anisotropy is available to support the interfacial exchange bias, leading to the saturation of the exchange bias field beyond a certain thickness. However, in the FM/IrMn/FM trilayers, the additional interlayer effect of the two FM layers must be considered. When IrMn layer thickness $t_{\text{IrMn}} < t_c$, the short-range interaction of the two interfaces is usually induced by RKKY interlayer coupling[118] or orange peel effect[119] and the long-range interaction ($t_{\text{IrMn}} > t_{\text{max}}$) shows the exchange spring behavior[120]. When $t_c < t_{\text{IrMn}} < t_{\text{max}}$, there will be an interplay between the interlayer coupling and the AFM anisotropy of the IrMn layer, which usually

induces exchange bias enhancement and propagation phenomenon of the two interfaces[121][123]. In polycrystalline IrMn structures, the size of the grains must be taken into account as a crucial factor in the propagation of exchange bias[122]. The hysteresis loops of Co (1.0)/IrMn (t_{IrMn})/Co₇₇Gd₂₃ (4.0) trilayers with $t_{\text{IrMn}} = 3$ to 8 nm are shown in Fig. 7.2 (a-d). The major loops (black) reflect the full switching of the entire structure. The minor loops (red) only reflect the reversal of the CoGd layer without Co layer reversal. We can note that the overlapping of major and minor loops differs in various IrMn layer thicknesses. For the thinner 3 and 5 nm IrMn layer (Fig. 7.2(a)(b)), without Co layer switching, the right branch of the CoGd loop shifts leftward. However, for the thicker 6.5 and 8 nm IrMn layers (Fig. 7.2(c)(d)), the CoGd subloops almost overlap with major and minor loops. When $t_{\text{IrMn}}=6.5$ and 8 nm, the exchange bias is generated by the AFM grains of each side and keeps independent during the magnetization reversal. When $t_{\text{IrMn}}<5$ nm, after the full switching of the trilayers, the nonrecoverable reversal of the AFM spins happened in Co/IrMn interface propagating through interlayer coupling across the AFM volume orders and acting on the IrMn/CoGd interface. In addition, the interlayer coupling can be seen as an energy barrier and partially unlocks the exchange coupling of CoGd after Co is fully switched[122]. With the strong interlayer coupling of the two interfaces, the AFM volume orders can be well characterized by the interfacial exchange bias and help us further explore the interfacial and volume AFM orders rearrangement under the femtosecond laser-induced ultrafast dynamics.

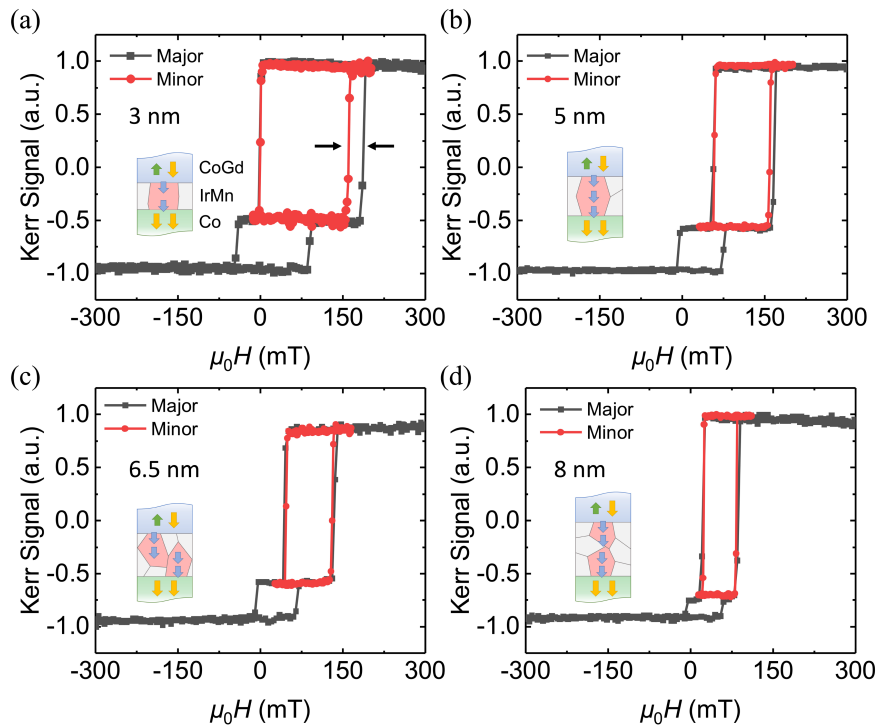


Fig. 7.2 The interlayer coupling of the Co/IrMn and IrMn/CoGd interfaces. (a)-(d) Major (black) and minor (red) loops of Co (1.0)/IrMn (t_{IrMn})/Co₇₇Gd₂₃ (4.0) trilayers with $t_{\text{IrMn}} = 3, 5, 6.5$ and 8 nm. When $t_{\text{IrMn}} = 3$ and 5 nm, the right branch of the minor loop shows a clear leftward shift. When $t_{\text{IrMn}} = 6.5$ and 8 nm, the major and minor loops overlap with each other.

7.3 Exchange bias switching and ultrafast antiferromagnet rearrangement

Single-shot laser-induced exchange bias switching at IrMn/CoGd interface was performed for various laser fluences with IrMn thickness t_{IrMn} ranging from 3 to 8 nm in Fig. 7.3(a)-(d). Due to the laser-induced heating, the temperature of the trilayer system exceeded the Néel temperature of the IrMn layer. In the meantime, the exchange bias of the Co/IrMn interface is only affected by laser heating and the interacted AFM spin configuration itself. In Fig. 7.3, we can note that the maximum amplitude of the exchange bias switching at IrMn/CoGd interface decreases with the increased IrMn thickness. Compared to the initial exchange bias after annealing, 37%~19% of the switched exchange bias varies from 3 nm ~ 8 nm IrMn thickness. However, the exchange bias of Co/IrMn interface reduces close to zero at $t_{\text{IrMn}}=3$ nm and remains positive at $t_{\text{IrMn}}=5, 6.5$, and 8 nm, but is much less pronounced. We can conclude that: (1) The reduction of dual exchange bias indicates that under such an ultrafast laser excitation process, the recovery of the AFM volume orders is not fully deterministic and thus does not allow the interfacial AFM spins to rearrange completely. (2) The amplitude of exchange bias switching in IrMn/CoGd decreases as the thickness of IrMn increases. This effect is attributed to the attenuated interfacial coupling, as depicted in Fig. 7.3(d). (3) The ultrafast demagnetization and antiparallel final state cause a twist in the AFM volume orders, which leads to zero exchange bias at the Co/IrMn interface.

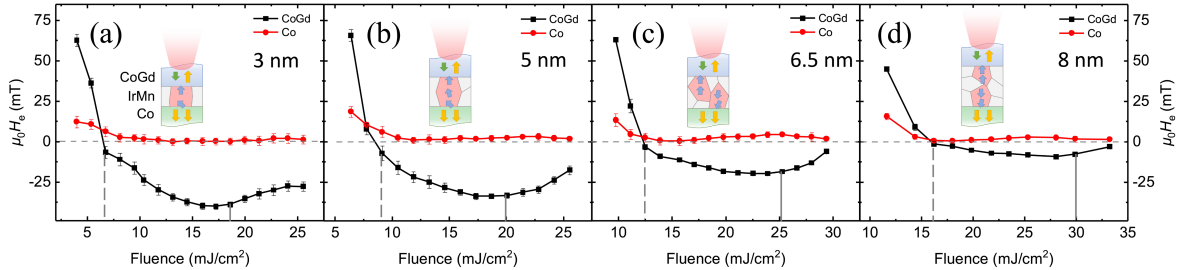


Fig. 7.3 Single-shot exchange bias switching in Co/IrMn/CoGd trilayers. (a)-(d) Exchange bias field of CoGd and Co interface in 3, 5, 6.5 and 8 nm IrMn samples after shining to a single linearly polarized laser pulse with a pulse duration of 40 fs and various fluences. The vertical dash line indicates the threshold fluence of CoGd switching and the solid line indicates the demagnetization fluence that CoGd begins to demagnetize.

From the fluence-dependent exchange bias switching at various IrMn thicknesses, we can only observe the ultrafast AFM spins rearrangement at the IrMn/CoGd interface, and the behavior of AFM volume orders is still unclear. Therefore, we focused on the Co (1.0)/IrMn (3.0)/CoGd (4.0) sample and utilized the exchange bias variation of the two interfaces. The trilayer system with $t_{\text{IrMn}}=3$ nm suggests a strong interlayer interaction in the IrMn volume order. The recovery of exchange bias after laser excitation depends on AFM spin rotation at both interfaces, as well as the competition or propagation during the rearrangement of AFM volume orders on the antiparallel (AP) or parallel (P) configuration of the two interfaces. Firstly, we start from the P initial state, as shown in Fig. 7.4(a). After laser excitation, the exchange bias of IrMn/CoGd interface switches to negative (CoGd-a), Co layer remagnetization to initial but the

exchange bias reduces to zero (Co-a) over the fluence of CoGd switching threshold (vertical dash line), as shown in Fig. 7.4(c). In the other case, we use the external field to reverse the Co layer to AP configuration but with initial positive exchange bias (Fig. 7.4(b)). After the laser shines at zero fields, the exchange bias of both interfaces switches to negative after CoGd begins switching (CoGd-b and Co-b in Fig. 7.4(b)). From the fluence dependent of CoGd interfacial exchange bias with different Co states, we can note that, in the all-optical switching window of CoGd (between the solid and dash line), the AFM spins rearrangement of IrMn/CoGd interface is not affected by the Co/IrMn interface state, which represents almost the same AFM spin configuration at the IrMn/CoGd interface. But the P final state after laser excitation allows AFM layer to further reorder without forming a twist domain wall and propagates to Co/IrMn interface. Over 17 mJ/cm^2 , CoGd demagnetizes and gradually becomes a multidomain state. The exchange bias reduces toward zero, and the AFM spin orders at the IrMn/CoGd interface cannot be well defined. However, with the higher temperature and longer time heating, the negative exchange bias of Co/IrMn interface (Co-b) can lead to the additional pinning of the AFM layer than zero exchange bias situation (Co-a) and result in the exchange bias field of IrMn/CoGd negative shift (CoGd-b) compared to AP final state (CoGd-a). Accordingly, it is observed that the competition and propagation of exchange bias can be discerned over a broad range of laser fluence. Within the switching window of CoGd, the reorientation of AFM spins at the IrMn/CoGd interface can be efficiently achieved through a single laser pulse, which further influences the AFM volume orders. When the laser fluence exceeds the switching window and CoGd loses its dominance of the interfacial AFM spins, the exchange bias of the IrMn/CoGd interface is found to be sensitive to different AFM order configurations owing to interlayer interaction.

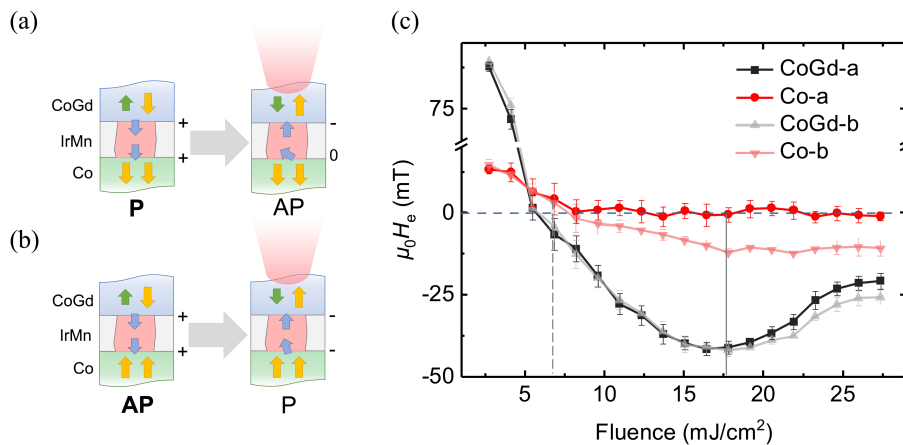


Fig. 7.4 The single-shot exchange bias switching with different Co states at $t_{\text{IrMn}}=3 \text{ nm}$. (a) Switching to the final state (AP) from the initial after-annealing state (P). (b) Shining the laser on the AP initial state and switching to P final state after reversing Co layer by an external field. (c) Evolution of $\mu_0 H_e$ of different CoGd and Co initial state after excitation by one single laser pulse as a function of the laser fluence. Curve CoGd-a and Co-a represent the evolution of $\mu_0 H_e$ from P initial state. Curve CoGd-b and Co-b represent the evolution of $\mu_0 H_e$ from AP initial state. The vertical dash line indicates the threshold fluence of CoGd switching and the solid line indicates the demagnetization fluence that CoGd begins to gradually become a multidomain state.

Furthermore, we investigate the exchange bias repeated switching by multi-pulses excitation. We use the number of laser pulses with a fluence of 16 mJ/cm^2 to shine from the P (Fig. 7.5(a)) and AP (Fig. 7.5(b)) initial state, respectively. The AP initial state is obtained by reversing the Co layer with an external field and then removing the field when shining the laser. The related continuous switching results are shown in Fig. 7.5 (c)(d), a repeatable and stable exchange bias switching can be found at IrMn/CoGd interface in the range of $\pm 40 \text{ mT}$ in both situations. On the contrary, the exchange bias of Co/IrMn interface shows a constant value ($\sim 0 \text{ mT}$ and -8 mT) after the first pulse. Then we use higher fluence with 21 mJ/cm^2 over the CoGd switching window, as shown in Fig. 7.5(e)(f). In the odd number of laser pulses, the CoGd layer begins to demagnetize and the amplitude of the switched exchange bias of IrMn/CoGd interface starts to decrease according to Fig. 7.4(c). However, a significant difference can be noted in the back-switched exchange bias amplitude at the even number of pulses on different Co states (Fig. 7.5 (e)(f)). The demagnetization of CoGd at high fluence will lose dominance on AFM orders, and the effective exchange bias of Co/IrMn can propagate to IrMn/CoGd interface. As shown in Fig. 7.5(f), the negative exchange bias of the Co/IrMn interface effectively prevents the back-switched exchange bias of IrMn/CoGd interface. Therefore, after the first laser excitation, the AFM orders may transition into a metastable state depending on the initial configuration of the two interfaces. The independent behavior of the interfaces upon subsequent laser pulse excitation provides further evidence that the exchange bias switching of the IrMn/CoGd interface is primarily driven by the rearrangement of interfacial AFM spins. Moreover, the AO-HIS of the coupled CoGd layer can be utilized as an ultrafast reset method for the AFM.

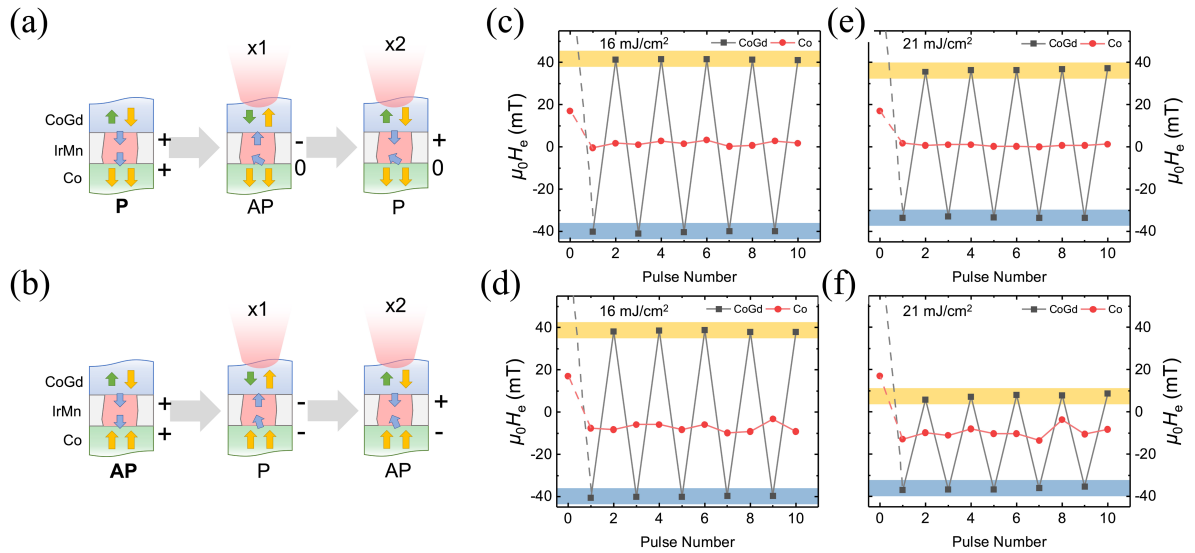


Fig. 7.5 Exchange bias switching with the number of pulses at different Co states. (a) The laser excitation from the P initial state with a laser fluence of (c) 16 mJ/cm^2 and (e) 21 mJ/cm^2 . (b) The laser excitation from AP initial state with a laser fluence of (d) 16 mJ/cm^2 and (f) 21 mJ/cm^2 .

7.4 Summary

In this chapter, we investigated dual perpendicular exchange bias systems in Co/IrMn/CoGd trilayers using both static field switching and ultrafast all-optical manipulation. Our results demonstrate the IrMn thickness-dependent interlayer coupling between the two exchange bias interfaces and reveal that the exchange bias at the IrMn/CoGd interface can be effectively controlled with a single femtosecond laser pulse. This manipulation is attributed to the ultrafast rearrangement of AFM spins at the interface, which also has a significant impact on the AFM volume orders. Furthermore, our observations of the competition between the Co/IrMn and IrMn/CoGd exchange-biased interfaces under ultrafast dynamics highlight the effectiveness of the AO-HIS in enhancing the efficiency of coupled AFM manipulation. These findings provide new insights into exchange bias phenomena and have implications for the development of ultrafast, field-free, and energy-efficient antiferromagnet manipulation techniques.

Chapter 8.

Conclusion

In this thesis, we propose a method for electrically modulating sub-nanosecond antiferromagnetic exchange bias by combining spin-orbit torque, thermal effects, and the Oersted field. We utilized a heavy metal as the bottom electrode and fabricated a three-terminal MTJ device on an AFM/FM composite storage layer. Under DC current, the writing of the antiferromagnetic storage layer is mainly achieved through a combination of the current's thermal effect and the Oersted field. However, with short-pulsed currents, the thermal effect becomes less significant, and the spin current generated by the heavy metal becomes dominant for switching the storage layer. Through macroscopic spin simulations, we establish the writing mechanism for achieving antiferromagnetic state switching by the combined effect of spin-orbit torque and the Oersted field. Our findings provide a new approach for electrically regulating sub-nanosecond antiferromagnetic exchange bias and offer a theoretical basis for developing higher-performance magnetic memory devices.

Furthermore, we have successfully achieved antiferromagnetic exchange bias switching in less than 100 ps using a single femtosecond laser, based on the AFM/FiM perpendicular exchange bias structure. While antiferromagnetic materials exhibit spin dynamics on terahertz timescales, the switching speed is limited in the antiferromagnetic/ferromagnetic exchange bias system due to the coupled ferromagnetic layer. To overcome this limitation and enhance writing speeds, we introduce the CoGd ferrimagnetic alloy. By utilizing the all-optical ultrafast magnetic switching of CoGd under the femtosecond laser, we achieve the dynamics of antiferromagnetism in the terahertz range. Through optimization of structural parameters, we successfully realize exchange bias switching using a single femtosecond laser and investigate the dependence on laser fluence and pulse numbers. Time-resolved measurement demonstrates that the exchange bias switching occurs in less than 100 ps. This research provides a theoretical and experimental foundation for the development of high-speed memories based on antiferromagnetic materials.

This study predicts the ultrafast dynamics of antiferromagnetism at the sub-picosecond level through theoretical modeling. Using atomistic simulations, we accurately describe the grain structure of polycrystalline IrMn materials and the amorphous state of CoGd. Our results show that IrMn exhibits a faster demagnetization rate compared to ferromagnetic materials. Within a short period after laser action, each IrMn grain can be remagnetized to a single-domain state in just 2 ps and stochastically coupled to Co or Gd. In ultrafast timescales, we observe independent and random probabilistic switching between different grains of IrMn. These findings deepen our understanding of the behavior of magnetic moments in antiferromagnetic materials, providing valuable insights for the development of faster and denser magnetic memory devices and other related applications.

Résumé étendu

Depuis l'invention du transistor, les industries de l'informatique et des semi-conducteurs ont connu de nombreuses avancées technologiques significatives. En 1965, Gordon Moore, l'un des fondateurs d'Intel, a prédit que le nombre de transistors pouvant être incorporés dans les circuits intégrés doublerait tous les 18 à 24 mois au cours de la décennie suivante, entraînant un doublement correspondant des performances, connu sous le nom de loi de Moore. Les progrès de la technologie informatique s'accompagnent d'une demande d'amélioration des performances informatiques. Au cours des 50 dernières années, la loi de Moore a vu la taille des circuits intégrés augmenter en même temps que les performances des puces. Aujourd'hui, les très grands circuits intégrés basés sur la technologie CMOS (complementary metal-oxide-semiconductor) sont à la base de toute l'industrie moderne de l'information. Ces progrès stimulent directement le développement de divers secteurs, notamment l'électronique grand public, l'informatique à grande échelle, l'aérospatiale, l'informatisation de la défense, etc.

Cependant, à mesure que la taille des caractéristiques CMOS diminue, l'effet quantique commence à jouer un rôle important. Lorsque les transistors sont réduits à l'échelle nanométrique, des phénomènes tels que l'effet tunnel quantique et la conductivité sous le seuil deviennent importants. Ces facteurs contribuent à un courant de fuite important, ce qui entraîne une augmentation notable de la consommation d'énergie statique des transistors. Dans certains cas, cette consommation statique dépasse même la consommation dynamique causée par les calculs logiques. Le courant de fuite est devenu l'une des principales raisons de la défaillance des dispositifs de mémoire volatile CMOS traditionnels, tels que les mémoires dynamiques à accès aléatoire (DRAM) et les mémoires statiques à accès aléatoire (SRAM), depuis que le nœud du processus a atteint 20 nm. Lorsque la consommation d'énergie de la puce atteint un certain niveau, la température de la puce augmente, ce qui entraîne des problèmes d'échauffement. Les performances et la fiabilité de la puce sont alors compromises. De plus, alors que la vitesse du processeur continue d'augmenter, celle de la mémoire ne progresse pas, ce qui entraîne une disparité croissante entre les deux. Dans l'architecture classique de l'ordinateur de von Neumann, l'échange fréquent de données entre le processeur et la mémoire entraîne une forte consommation d'énergie lors de la transmission. L'ensemble de ces facteurs contribue à une consommation d'énergie élevée, à une fiabilité réduite et à une utilisation inefficace de l'énergie. Ils limitent donc considérablement la miniaturisation et les performances des circuits intégrés (CI). Par conséquent, la loi de Moore, qui devait initialement se poursuivre au moins jusqu'en 2020, a commencé à s'écarter de l'évolution réelle à la fin de l'année 2013.

L'augmentation de la capacité de stockage des données s'accompagne d'une augmentation de la consommation d'énergie. Des statistiques récentes montrent que les plus grands centres de données du monde consommeront plus d'électricité en 2020 que le Royaume-Uni tout entier n'en a produit en 2017. D'ici à 2030, ces centres devraient consommer environ 13 % de l'électricité mondiale. De plus, le secteur des technologies de l'information et de la communication (TIC) représente déjà environ 11 % de la consommation mondiale d'énergie,

soit l'équivalent de la production totale d'électricité du Japon en 2017. Cette forte consommation d'énergie pèse sur l'approvisionnement mondial en électricité et a des conséquences environnementales importantes, notamment l'augmentation des émissions de gaz à effet de serre. Par conséquent, s'attaquer au goulot d'étranglement de la consommation d'énergie des circuits intégrés dans l'"ère post-Moore" est devenu une priorité essentielle dans les domaines de la défense nationale, de la science et de la technologie, et de l'environnement mondial. Il est impératif d'explorer de nouvelles voies technologiques et des approches innovantes pour relever ces défis.

Pour relever ces défis dans l'ère post-Moore, les chercheurs explorent activement de nouvelles voies technologiques et des orientations novatrices. Leur champ d'action s'étend des matériaux fondamentaux aux systèmes architecturaux avancés. Il s'agit notamment du développement de nouveaux matériaux semi-conducteurs, de l'optimisation des processus de miniaturisation des puces, de l'exploration d'architectures de puces innovantes et de l'innovation en matière de modèles et d'algorithmes de calcul. Deux options sont actuellement envisagées pour maintenir les progrès de la loi de Moore. La première consiste à améliorer le processus de fabrication des transistors en introduisant des propositions récentes telles que le Fin Field Effect Transistor (FinFET) et le Gate-All-Around Field Effect Transistor (GAAFET). Il convient toutefois de noter que les coûts de fabrication associés à ces solutions sont relativement élevés. Une autre option explorée est l'utilisation de dispositifs innovants tels que les mémoires non volatiles et les dispositifs logiques. Les dispositifs de mémoire non volatile offrent deux avantages inhérents par rapport aux dispositifs de mémoire volatile CMOS traditionnels tels que la DRAM et la SRAM. Premièrement, ils conservent les données en cas de panne de courant ou de black-out, ce qui élimine le besoin d'une alimentation constante et réduit la consommation d'énergie statique. Deuxièmement, elles permettent l'intégration du stockage des données et du calcul, en combinant le traitement, la transmission et le stockage des données au sein même de la mémoire. Cette intégration réduit considérablement la consommation d'énergie pendant le transfert des données et améliore l'intégration des circuits. En outre, les dispositifs de mémoire non volatile offrent des vitesses de lecture/écriture rapides, une grande fiabilité et une longue durée de vie, ce qui les rend prometteurs pour un large éventail d'applications.

Les mémoires non volatiles actuelles comprennent la mémoire à changement de phase (PCM), la mémoire vive résistive (RRAM), la mémoire vive à pont conducteur (CBRAM) et la mémoire vive magnétorésistive (MRAM). En 2015, le professeur Hansen Huang de l'université de Stanford a souligné que la STT-MRAM est le type de mémoire non volatile le plus populaire au monde après avoir étudié les performances de différents types de dispositifs de mémoire non volatile entre 2001 et 2014. La STT-MRAM présente un avantage significatif sur les autres mémoires non volatiles en termes de vitesse d'écriture des données et de consommation d'énergie pendant l'écriture.

La MRAM a connu trois générations de stockage magnétique. La première génération est la Toggle-MRAM, basée sur l'écriture par champ magnétique. La deuxième génération est la STT-MRAM basée sur le couple de transfert de spin (STT), qui a déjà atteint la production de masse.

La dernière génération est la SOT-MRAM basée sur le couple spin-orbite (SOT). Ces trois générations de mémoire magnétique offrent des avantages significatifs par rapport aux autres technologies de mémoire non volatile en termes de vitesse d'écriture des données et de consommation d'énergie, grâce à leurs différentes approches de l'écriture des données. Avec chaque génération, la vitesse d'écriture de la mémoire magnétique s'est améliorée et sa capacité de stockage a augmenté. Cependant, les trois générations utilisent des matériaux ferromagnétiques comme support de stockage des informations, ce qui limite leurs performances. Tout d'abord, la vitesse d'écriture des données de ces mémoires ferromagnétiques est limitée par la fréquence de résonance ferromagnétique à champ nul, généralement de l'ordre du gigahertz (GHz), qui correspond à des échelles de temps de l'ordre de la nanoseconde. Par exemple, les vitesses d'écriture actuelles de la STT-MRAM et de la SOT-MRAM sont de l'ordre de la nanoseconde. Bien que la SOT-MRAM puisse atteindre des vitesses d'écriture inférieures à la nanoseconde en utilisant des courants d'écriture très élevés à travers son dispositif à trois bornes, cela se traduit par une consommation d'énergie plus élevée. Deuxièmement, en termes de stabilité des données, les matériaux ferromagnétiques sont sensibles aux changements causés par les champs magnétiques externes, ce qui rend les données stockées vulnérables aux interférences. En outre, les matériaux ferromagnétiques eux-mêmes génèrent des champs parasites qui peuvent perturber la stabilité des données dans les bits de données voisins. Ces facteurs contribuent au fait que les puces à mémoire de spin existantes sont confrontées à des goulets d'étranglement en termes de vitesse d'écriture, de fiabilité et de densité de stockage.

Les chercheurs ont proposé d'utiliser une mémoire spintronique basée sur des matériaux antiferromagnétiques pour résoudre les problèmes de vitesse et de fiabilité des mémoires ferromagnétiques actuelles. Contrairement aux matériaux ferromagnétiques, les matériaux antiferromagnétiques sont constitués de deux sous-réseaux avec des moments magnétiques opposés et un fort couplage d'échange. Les matériaux antiferromagnétiques ne présentent donc pas de magnétisme macroscopique et sont moins sensibles aux champs magnétiques externes. De plus, le couplage entre les sous-réseaux génère un champ équivalent important, ce qui permet au matériau antiferromagnétique d'atteindre des fréquences térahertz, nettement supérieures à celles des matériaux ferromagnétiques. Ces avantages ont rendu les matériaux antiferromagnétiques très attrayants pour la prochaine génération de mémoires magnétiques. Cependant, les propriétés non magnétiques des matériaux antiferromagnétiques rendent difficile la détection de leurs moments magnétiques, et les diverses structures de moments magnétiques des différents matériaux antiferromagnétiques ont conduit à différentes explications de leur mécanisme d'écriture. Des percées récentes ont été réalisées en utilisant des hétérostructures métal lourd/antiferromagnétique pour détecter l'état antiferromagnétique grâce à l'effet de couple spin-orbite généré par le courant de spin généré par le métal lourd injecté dans la couche antiferromagnétique. Une autre méthode consiste à utiliser le couplage d'échange entre les matériaux antiferromagnétiques et ferromagnétiques pour réguler indirectement l'antiferromagnétisme de l'interface via une couche ferromagnétique couplée. Cet état peut être lu à l'aide de méthodes efficaces telles que la magnétorésistance géante (GMR), la magnétorésistance tunnel (TMR) ou les effets magnéto-optiques (MO). Cet article se

concentre sur la modulation antiferromagnétique dans les hétérostructures AFM/FM.

Le phénomène de biais d'échange est un effet curieux qui a été largement utilisé dans divers dispositifs de spintronique en raison de sa capacité à fournir un champ de biais important. Cependant, il n'existe pas encore de modèle théorique complet pour expliquer cet effet. Cette thèse vise à consolider les modèles théoriques classiques et les applications spécifiques du biais d'échange dans divers dispositifs spintroniques depuis sa découverte. En outre, les avancées récentes dans la manipulation de l'effet du biais d'échange seront discutées, ce qui non seulement améliore notre compréhension du mécanisme sous-jacent, mais ouvre également de nouvelles possibilités pour les dispositifs électroniques auto-sélectifs. Cet article se concentre sur l'utilisation du couple spin-orbite pour développer des dispositifs de spin hautement fiables et efficaces. En outre, l'article explorera le comportement de commutation et le mécanisme physique du biais d'échange dans les processus ultrarapides en tirant parti de la technologie de commutation tout-optique utilisant des lasers femtosecondes. Cette recherche a le potentiel de fournir des solutions efficaces pour manipuler efficacement le biais d'échange.

Le chapitre 1 présente le contexte du document et donne une brève introduction au contenu des chapitres suivants.

Le chapitre 2 commence par une introduction aux matériaux magnétiques et au stockage des données magnétiques et passe en revue la découverte du biais d'échange, l'évolution des modèles théoriques et ses applications pour les dispositifs spintroniques. Il se concentre en particulier sur les différents modèles théoriques proposés pour le biais d'échange, ainsi que sur l'utilisation traditionnelle de la structure du biais d'échange pour épingler une couche de référence. Le chapitre résume également les différentes techniques appliquées ces dernières années pour manipuler le biais d'échange.

Le chapitre 3 commence par une description de la fabrication des dispositifs spintroniques, qui couvre le dépôt d'un empilement de films magnétiques, les processus de modelage et le dépôt de diélectrique. Les performances électriques du dispositif spintronique sont caractérisées par des mesures de courant continu et d'impulsion. En outre, l'effet magnéto-optique et les mesures correspondantes sont présentés, ainsi que les mesures du magnétisme ultrarapide basées sur le laser femtoseconde.

Le chapitre 4 se concentre sur la conception d'un empilement de MTJ à double biais d'échange, suivi d'une étude détaillée de l'optimisation de la couche de stockage antiferromagnétique/ferromagnétique (AFM/FM). Un contrôle précis des propriétés magnétiques de la couche de stockage est obtenu grâce à des études approfondies sur les épaisseurs de la couche antiferromagnétique, de la couche d'amorçage et de la couche d'insertion. En étudiant la dépendance de la température du biais d'échange et en explorant les conditions optimales de recuit, il est possible d'obtenir la pile MTJ avec des propriétés idéales. Ceci sert de base pour réaliser le contrôle électrique du biais d'échange dans le chapitre suivant.

Le chapitre 5 étudie les caractéristiques de commutation de la polarisation d'échange dans un dispositif MTJ à trois bornes et analyse l'influence du champ d'Oersted et du chauffage par effet

Joule. En outre, il examine la contribution des effets thermiques ou du couple spin-orbite (SOT) par le biais de mesures dans le domaine temporel des impulsions. Enfin, il étudie la dépendance de l'épaisseur de la couche d'insertion W et les dispositifs d'électrode inférieure IrMn pour optimiser la consommation d'énergie dans le processus d'écriture.

Le chapitre 6 se penche sur la manipulation ultrarapide du biais d'échange par laser femtoseconde. Il fournit une caractérisation détaillée de l'hétérostructure à polarisation d'échange perpendiculaire IrMn/CoGd (AFM/FiM), y compris l'épaisseur de l'antiferromagnétique IrMn, la concentration du ferrimagnétique CoGd et la dépendance par rapport à la température. Ce chapitre présente également des expériences sur la commutation répétable ultrarapide du biais d'échange, en explorant la dépendance de la fluence laser et du nombre d'impulsions. Les mesures résolues en temps confirment que la commutation du biais d'échange se produit sur une échelle de temps de 100 ps. Des simulations atomistiques sont utilisées pour explorer plus avant le mécanisme de commutation du biais d'échange, la dynamique sub-picoseconde et le comportement de commutation probabiliste des grains antiferromagnétiques.

Le chapitre 7 réalise la manipulation du biais d'échange dans les tricouches Co/IrMn/CoGd (FM/AFM/FiM) avec un double biais d'échange perpendiculaire. Les caractéristiques quasi-statiques montrent l'interaction intercouche de l'IrMn en fonction de l'épaisseur de l'interface à double biais d'échange. La commutation du biais d'échange induite par un laser femtoseconde unique indique le réarrangement ultrarapide des spins AFM à l'interface IrMn/CoGd et démontre en outre la concurrence entre les ordres de volume AFM.

Le chapitre 8 présente une conclusion et discute de la perspective de cette thèse.

Bibliography

- [1]J M D Coey. *Magnetism and magnetic materials*. (Cambridge University Press. [Reprinted, 2009]).
- [2]Smart, J. S. Molecular Field Treatment of Ferromagnetism and Antiferromagnetism. *Physical Review* **86**, 968–974 (1952).
- [3]Mermin, N. D. & Wagner, H. Absence of Ferromagnetism or Antiferromagnetism in One- or Two-Dimensional Isotropic Heisenberg Models. *Physical Review Letters* **17**, 1133–1136 (1966).
- [4]Blundell, S. & Oxford University Press. *Magnetism in condensed matter*. (Oxford University Press, 2012).
- [5]Bandic, Z. Z. & Victora, R. H. Advances in Magnetic Data Storage Technologies. *Proceedings of the IEEE* **96**, 1749–1753 (2008).
- [6]Richter, H. J. The transition from longitudinal to perpendicular recording. *Journal of Physics D: Applied Physics* **40**, R149–R177 (2007).
- [7]Teruya Shinjo. *Nanomagnetism and Spintronics*. Elsevier eBooks (Elsevier Science, 2009).
- [8]Fullerton, E. E. & Childress, J. R. Spintronics, Magnetoresistive Heads, and the Emergence of the Digital World. *Proceedings of the IEEE* **104**, 1787–1795 (2016).
- [9]Kief, M. T. & Victora, R. H. Materials for heat-assisted magnetic recording. *MRS Bulletin* **43**, 87–92 (2018).
- [10]Baibich, M. N. *et al.* Giant Magnetoresistance of (001)Fe/(001)Cr Magnetic Superlattices. *Physical Review Letters* **61**, 2472–2475 (1988).
- [11]Barnaś, J., Fuss, A., Camley, R. E., Grünberg, P. & Zinn, W. Novel magnetoresistance effect in layered magnetic structures: Theory and experiment. *Physical Review B* **42**, 8110–8120 (1990).
- [12]Grünberg, P. A. Nobel Lecture: From spin waves to giant magnetoresistance and beyond. *Reviews of Modern Physics* **80**, 1531–1540 (2008).
- [13]Mott, N. F. Electrons in transition metals. *Advances in Physics* **13**, 325–422 (1964).
- [14]Yuasa, S. & Djayaprawira, D. D. Giant tunnel magnetoresistance in magnetic tunnel junctions with a crystalline MgO(0 0 1) barrier. *Journal of Physics D* **40**, R337–R354 (2007).
- [15]Kowalska, E. Current-induced dynamics in hybrid geometry MgO-based spin-torque nano-oscillators. (2018).

- [16]Julliere, M. Tunneling between ferromagnetic films. *Physics Letters A* **54**, 225–226 (1975).
- [17]Miyazaki, T. & Nobuki Tezuka. Giant magnetic tunneling effect in Fe/Al₂O₃/Fe junction. *Journal of Magnetism and Magnetic Materials* **139**, L231–L234 (1995).
- [18]Mooodera, J. S., Kinder, L. R., Wong, T. M. & Meservey, R. Large Magnetoresistance at Room Temperature in Ferromagnetic Thin Film Tunnel Junctions. *Physical Review Letters* **74**, 3273–3276 (1995).
- [19]Wei, H. X., Qin, Q. H., Ma, M., Sharif, R. & Han, X. F. 80% tunneling magnetoresistance at room temperature for thin Al–O barrier magnetic tunnel junction with CoFeB as free and reference layers. *Journal of Applied Physics* **101**, 09B501 (2007).
- [20]Mathon, J. & Umerski, A. Theory of tunneling magnetoresistance of an epitaxial Fe/MgO/Fe(001) junction. *Physical Review B* **63**, (2001).
- [21]Butler, W. H., Zhang, X.-G. ., Schulthess, T. C. & MacLaren, J. M. Spin-dependent tunneling conductance of Fe|MgO|Fe sandwiches. *Physical Review B* **63**, (2001).
- [22]Yuasa, S., Nagahama, T., Fukushima, A., Suzuki, Y. & Ando, K. Giant room-temperature magnetoresistance in single-crystal Fe/MgO/Fe magnetic tunnel junctions. *Nature Materials* **3**, 868–871 (2004).
- [23]Parkin, S. S. P. *et al.* Giant tunnelling magnetoresistance at room temperature with MgO (100) tunnel barriers. *Nature Materials* **3**, 862–867 (2004).
- [24]Engel, B. N. *et al.* A 4-Mb toggle MRAM based on a novel bit and switching method. *IEEE Transactions on Magnetics* **41**, 132–136 (2005).
- [25]Das, U. K. & Bhattacharyya, T. K. Opportunities in Device Scaling for 3-nm Node and Beyond: FinFET Versus GAA-FET Versus UFET. *IEEE Transactions on Electron Devices* **67**, 2633–2638 (2020).
- [26]Shalf, J. M. & Leland, R. Computing beyond Moore’s Law. *Computer* **48**, 14–23 (2015).
- [27]Guo, Z. *et al.* Spintronics for Energy- Efficient Computing: An Overview and Outlook. *Proceedings of the IEEE* **109**, 1398–1417 (2021).
- [28]Huai, Y. Spin-Transfer Torque MRAM (STT-MRAM): Challenges and Prospects. *AAPPS bulletin* **18**, (2008).
- [29]Hu, G. *et al.* Spin-transfer torque MRAM with reliable 2 ns writing for last level cache applications. *2019 IEEE International Electron Devices Meeting (IEDM)* **2019: 2.6**, (2019).
- [30]Alzate, J. G. *et al.* 2 MB Array-Level Demonstration of STT-MRAM Process and Performance Towards L4 Cache Applications. *2019 IEEE International Electron Devices Meeting (IEDM)* **2019: 2.4**, (2019).

- [31] Park, J.-H. *et al.* A novel integration of STT-MRAM for on-chip hybrid memory by utilizing non-volatility modulation. *2019 IEEE International Electron Devices Meeting (IEDM) 2019: 2.5*, (2019).
- [32] Naik, V. B. *et al.* Manufacturable 22nm FD-SOI Embedded MRAM Technology for Industrial-grade MCU and IOT Applications. *2019 IEEE International Electron Devices Meeting (IEDM) 2019: 2.3*, (2019).
- [33] Sun, J. Spin-current interaction with a monodomain magnetic body: A model study. *Physical review* **62**, 570–578 (2000).
- [34] Miron, I. M. *et al.* Perpendicular switching of a single ferromagnetic layer induced by in-plane current injection. *Nature* **476**, 189–193 (2011).
- [35] van den Brink, A. *et al.* Spin-Hall-assisted magnetic random access memory. *Appl. Phys. Lett.* **104**, 012403–012403 (2014).
- [36] Wang, M. *et al.* Field-free switching of a perpendicular magnetic tunnel junction through the interplay of spin–orbit and spin-transfer torques. *Nature Electronics* **1**, 582–588 (2018).
- [37] Yasuda, H. *et al.* Voltage-control spintronics memory (VoCSM) having potentials of ultra-low energy-consumption and high-density. *2016 IEEE international electron devices meeting (IEDM) 2016: 27.6*, (2016).
- [38] Peng, S. Z. *et al.* Field-Free Switching of Perpendicular Magnetization through Voltage-Gated Spin-Orbit Torque. *2019 IEEE International Electron Devices Meeting (IEDM) 28.6.1–28.6.4* (2019).
- [39] Butsurin Jinnai *et al.* High-Performance Shape-Anisotropy Magnetic Tunnel Junctions down to 2.3 nm. *2020 IEEE International Electron Devices Meeting (IEDM) 24.6.1–24.6.4* (2020).
- [40] Grimaldi, E. *et al.* Single-shot dynamics of spin–orbit torque and spin transfer torque switching in three-terminal magnetic tunnel junctions. *Nature Nanotechnology* **15**, 111–117 (2020).
- [41] Xiong, D. *et al.* Antiferromagnetic spintronics: An overview and outlook. *Fundamental Research* **2**, 522–534 (2022).
- [42] Moriyama, T., Oda, K., Takuo Ohkochi, Kimata, M. & Ono, T. Spin torque control of antiferromagnetic moments in NiO. *Scientific Reports* **8**, (2018).
- [43] Sevdener Arpacı *et al.* Observation of current-induced switching in non-collinear antiferromagnetic IrMn₃ by differential voltage measurements. *Nature Communications* **12**, (2021).

- [44]Tsai, H. *et al.* Electrical manipulation of a topological antiferromagnetic state. *Nature* **580**, 608–613 (2020).
- [45]Tomoya Higo *et al.* Perpendicular full switching of chiral antiferromagnetic order by current. *Nature* **607**, 474–479 (2022).
- [46]Lin, P.-H. *et al.* Manipulating exchange bias by spin–orbit torque. *Nature Materials* **18**, 335–341 (2019).
- [47]Peng, S. *et al.* Exchange bias switching in an antiferromagnet/ferromagnet bilayer driven by spin–orbit torque. *Nature Electronics* **3**, 757–764 (2020).
- [48]Meiklejohn, W. H. & Bean, C. P. New Magnetic Anisotropy. *Physical Review* **102**, 1413–1414 (1956).
- [49]Soeya, S., Imagawa, T., Mitsuoka, K. & Narishige, S. Distribution of blocking temperature in bilayered Ni₈₁Fe₁₉/NiO films. *Journal of Applied Physics* **76**, 5356–5360 (1994).
- [50]Meiklejohn, W. H. Exchange Anisotropy-A Review. *Journal of Magnetism and Magnetic materials* **33**, 1328–1335 (1962).
- [51]Tsunoda, M., Tsuchiya, Y., Konoto, M. & Takahashi, M. Microstructure of antiferromagnetic layer affecting on magnetic exchange coupling in trilayered NiFe/25 at% NiMn/NiFe films. *Journal of Magnetism and Magnetic Materials* **171**, 29–44 (1997).
- [52]Jungblut, R., R. Coehoorn, Johnson, M. T., de & Angelina H.M.E. Reinders. Orientational dependence of the exchange biasing in molecular-beam-epitaxy-grown Ni₈₀Fe₂₀/Fe₅₀Mn₅₀bilayers (invited). *Journal of Applied Physics* **75**, 6659–6664 (1994).
- [53]Néel, L. Étude théorique du couplage ferro-antiferromagnétique dans les couches minces. *Annales De Physique* **14**, 61–80 (1967).
- [54]Mauri, D., Siegmann, H. C., Bagus, P. S. & Kay, E. Simple model for thin ferromagnetic films exchange coupled to an antiferromagnetic substrate. *Journal of Applied Physics* **62**, 3047–3049 (1987).
- [55]Malozemoff, A. P. Random-field model of exchange anisotropy at rough ferromagnetic-antiferromagnetic interfaces. *Physical Review B* **35**, 3679–3682 (1987).
- [56]Takano, K., Kodama, R. H., Berkowitz, A. E., Cao, W. & Thomas, G. Role of interfacial uncompensated antiferromagnetic spins in unidirectional anisotropy in Ni₈₁Fe₁₉/CoO bilayers (invited). *Journal of Applied Physics* **83**, 6888–6892 (1998).
- [57]Ohldag, H. *et al.* Correlation between Exchange Bias and Pinned Interfacial Spins. *Physical Review Letters* **91**, (2003).

- [58]Fulcomer, E. & S.H. Charap. Thermal fluctuation aftereffect model for some systems with ferromagnetic-antiferromagnetic coupling. *Journal of Applied Physics* **43**, 4190–4199 (1972).
- [59]Nozières, J. P. *et al.* Blocking temperature distribution and long-term stability of spin-valve structures with Mn-based antiferromagnets. *Journal of Applied Physics* **87**, 3920–3925 (2000).
- [60]Baltz, V., B. Rodmacq, A. Zarefy, L. Lechevallier & B. Dieny. Bimodal distribution of blocking temperature in exchange-biased ferromagnetic/antiferromagnetic bilayers. *Physical Review B* **81**, (2010).
- [61]Jenkins, S. *et al.* Atomistic origin of exchange anisotropy in noncollinear γ -IrMn₃-CoFe bilayers. *Physical Review B* **102**, (2020).
- [62]Jenkins, S., Chantrell, R. W. & Evans, R. F. L. Exchange bias in multigranular noncollinear IrMn₃/CoFe thin films. *Physical Review B* **103**, (2021).
- [63]Jenkins, S., Chantrell, Roy. W. & Evans, R. F. L. Atomistic simulations of the magnetic properties of Ir_xMn_{1-x} alloys. *Physical Review Materials* **5**, (2021).
- [64]Jenkins, S., Chantrell, Roy. W. & Evans, Richard. F. L. Atomistic origin of the athermal training effect in granular IrMn/CoFe bilayers. *Physical Review B* **103**, (2021).
- [65]Iusipova, Iu. A. & Popov, A. I. Spin Valves in Microelectronics (A Review). *Semiconductors* **55**, 1008–1020 (2021).
- [66]Dupas, C. *et al.* Very large magnetoresistance effects induced by antiparallel magnetization in two ultrathin cobalt films. *Journal of Applied Physics* **67**, 5680–5682 (1990).
- [67]Dieny, B. *et al.* Giant magnetoresistive in soft ferromagnetic multilayers. *Physical Review B* **43**, 1297–1300 (1991).
- [68]Ioan Lucian Prejbeanu *et al.* Thermally assisted MRAM. *Journal of Physics: Condensed Matter* **19**, 165218–165218 (2007).
- [69]Ioan Lucian Prejbeanu *et al.* Thermally assisted MRAMs: ultimate scalability and logic functionalities. *Journal of Physics D* **46**, 074002–074002 (2013).
- [70]Bandiera, S. & B. Dieny. Thermally Assisted MRAM. *Springer eBooks* 1–29 (2015)
- [71]Wadley, P. *et al.* Electrical switching of an antiferromagnet. *Science* **351**, 587–590 (2016).
- [72]Chen, X. *et al.* Electric field control of Néel spin-orbit torque in an antiferromagnet. *Nature Materials* **18**, 931–935 (2019).
- [73]Manchon, A. *et al.* Current-induced spin-orbit torques in ferromagnetic and antiferromagnetic systems. *Reviews of Modern Physics* **91**, (2019).

- [74]H.-U. ter Meer *et al.* Direct Imaging of Current-Induced Antiferromagnetic Switching Revealing a Pure Thermomagnetoelastic Switching Mechanism in NiO. *Nano Letters* **21**, 114–119 (2020).
- [75]Takeuchi, Y. *et al.* Chiral-spin rotation of non-collinear antiferromagnet by spin–orbit torque. *Nature Materials* **20**, 1364–1370 (2021).
- [76]Shieh, H.-P.D & Kryder, M. H. The influence of deposition conditions on the magneto-optic effect in GdTbCo films. *IEEE Transactions on Magnetics* **21**, 1632–1634 (1985).
- [77]Vaterlaus, A., Beutler, T. C. & Meier, F. Spin-lattice relaxation time of ferromagnetic gadolinium determined with time-resolved spin-polarized photoemission. *Physical Review Letters* **67**, 3314–3317 (1991).
- [78]Wolfgang Hübner & Bennemann, K. H. Simple theory for spin-lattice relaxation in metallic rare-earth ferromagnets. *Physical review* **53**, 3422–3427 (1996).
- [79]Beaurepaire, E., Merle, J. C., A. Daunois & Bigot, J.-Y. Ultrafast Spin Dynamics in Ferromagnetic Nickel. *Physical Review Letters* **76**, 4250–4253 (1996).
- [80]Stanciu, C. D. *et al.* All-Optical Magnetic Recording with Circularly Polarized Light. *Physical Review Letters* **99**, (2007).
- [81]Cornelissen, T. D., Córdoba, R. & Koopmans, B. Microscopic model for all optical switching in ferromagnets. *Applied Physics Letters* **108**, 142405 (2016).
- [82]Vallobra, P. *et al.* Manipulating exchange bias using all-optical helicity-dependent switching. *Physical Review B* **96**, (2017).
- [83]Kelly, P. J. & Arnell, R. D. Magnetron sputtering: a review of recent developments and applications. *Vacuum* **56**, 159–172 (2000).
- [84]Moreau, W. M. *Semiconductor Lithography*. (Springer Science & Business Media, 2012).
- [85]Pirati, A. *et al.* EUV lithography performance for manufacturing: status and outlook. *Extreme Ultraviolet (EUV) Lithography VII* (2016)
- [86]Nojiri, K. & Springerlink (Online Service. *Dry Etching Technology for Semiconductors*. (Springer International Publishing, 2015).
- [87]Martin, P. M. *Handbook of deposition technologies for films and coatings: science, applications and technology*. (Elsevier, 2010).
- [88]Sala, G. *et al.* Real-time Hall-effect detection of current-induced magnetization dynamics in ferrimagnets. *Nature Communications* **12**, (2021).
- [89]Knudsen, O. The Faraday Effect and Physical Theory, 1845-1873. *Archive for History of Exact Sciences* **15**, 235–281 (1976).

- [90]Qiu, Z. & Bader, S. D. Surface magneto-optic Kerr effect. *Review of Scientific Instruments* **71**, 1243–1255 (2000).
- [91]Porter, G. Flash photolysis and spectroscopy. A new method for the study of free radical reactions. *Proceedings of the Royal Society of London. Series A. Mathematical and Physical Sciences* **200**, 284–300 (1950).
- [92]Sharma, P., Albisetti, E., Monticelli, M., Bertacco, R. & Petti, D. Exchange Bias Tuning for Magnetoresistive Sensors by Inclusion of Non-Magnetic Impurities. *Sensors* **16**, 1030 (2016).
- [93]Liu, H. *et al.* The optimization of Ta buffer layer in magnetron sputtering IrMn top spinvalve. *Thin Solid Films* **441**, 111–114 (2003).
- [94]Nowak, U. *et al.* Domain state model for exchange bias. I. Theory. *Physical review* **66**, (2002).
- [95]Ali, M. *et al.* Antiferromagnetic layer thickness dependence of the IrMn/Co exchange-bias system. *Physical Review B* **68**, (2003).
- [96]Aley, N. P. *et al.* Texture Effects in IrMn/CoFe Exchange Bias Systems. *IEEE Transactions on Magnetism* **44**, 2820–2823 (2008).
- [97]Chen, W. *et al.* Influence of seed layer on the magnetoresistance properties in IrMn-based magnetic tunnel junctions. *Journal of Magnetism and Magnetic Materials* **546**, 168674–168674 (2022).
- [98]Ali, M., Marrows, C. H. & Hickey, B. J. Controlled enhancement or suppression of exchange biasing using impurity layers. *Physical Review B* **77**, (2008).
- [99]Stiles, M. D. & McMichael, R. D. Coercivity in exchange-bias bilayers. *Physical Review B* **63**, (2001).
- [100]Kerr, E., Sebastiaan van Dijken & Coey, D. Influence of the annealing field strength on exchange bias and magnetoresistance of spin valves with IrMn. *Journal of Applied Physics* **97**, 093910–093910 (2005).
- [101]Ohldag, H. *et al.* Correlation between Exchange Bias and Pinned Interfacial Spins. *Physical Review Letters* **91**, (2003).
- [102]Samik DuttaGupta *et al.* Spin-orbit torque switching of an antiferromagnetic metallic heterostructure. *Nature Communications* **11**, (2020).
- [103]Baldrati, L. *et al.* Mechanism of Néel Order Switching in Antiferromagnetic Thin Films Revealed by Magnetotransport and Direct Imaging. *Physical Review Letters* **123**, (2019).
- [104]Wang, X., Pauyac, C. O. & Manchon, A. Spin-orbit-coupled transport and spin torque in a ferromagnetic heterostructure. *Physical Review B* **89**, (2014).

- [105]Fang, B. *et al.* Electrical Manipulation of Exchange Bias in an Antiferromagnet/Ferromagnet-Based Device via Spin–Orbit Torque. *Advanced Functional Materials* 2112406 (2022).
- [106]Zhang, W. *et al.* Spin Hall Effects in Metallic Antiferromagnets. *Physical Review Letters* **113**, (2014).
- [107]105.Wang, X. *et al.* Spin transmission in IrMn through measurements of spin Hall magnetoresistance and spin-orbit torque. *Physical review* **101**, (2020).
- [108]Aradhya, S. V., Rowlands, G., Oh, J.-H., Ralph, D. & Buhrman, R. A. Nanosecond-Timescale Low Energy Switching of In-Plane Magnetic Tunnel Junctions through Dynamic Oersted-Field-Assisted Spin Hall Effect. *Nano Letters* **16**, 5987–5992 (2016).
- [109]Haruo Honjo *et al.* First demonstration of field-free SOT-MRAM with 0.35 ns write speed and 70 thermal stability under 400°C thermal tolerance by canted SOT structure and its advanced patterning/SOT channel technology. *2019 IEEE International Electron Devices Meeting (IEDM)* 28.5.1–28.5.4 (2019).
- [110]Dong, J. *et al.* Tunneling Magnetoresistance in Noncollinear Antiferromagnetic Tunnel Junctions. *Physical Review Letters* **128**, (2022).
- [111]Shao, D.-F., Zhang, S.-H., Li, M., Eom, C.-B. & Tsymbal, E. Y. Spin-neutral currents for spintronics. *Nature Communications* **12**, (2021).
- [112]Ostler, T. A. *et al.* Ultrafast heating as a sufficient stimulus for magnetization reversal in a ferrimagnet. *Nature Communications* **3**, (2012).
- [113]Radu, I. *et al.* Transient ferromagnetic-like state mediating ultrafast reversal of antiferromagnetically coupled spins. *Nature* **472**, 205–208 (2011).
- [114]Chen, J. Y., Thiyagarajah, N., Xu, H. J. & Coey, J. M. D. Perpendicular exchange bias effect in sputter-deposited CoFe/IrMn bilayers. *Applied Physics Letters* **104**, 152405 (2014).
- [115]Koplak, O. V., Gornakov, V. S., Kabanov, Yu. P., Kunitsyna, E. I. & Shashkov, I. V. Temperature Dependence of the Exchange Anisotropy of a GdFeCo Ferrimagnetic Film Coupled to the IrMn Antiferromagnet. *JETP Letters* **109**, 722–728 (2019).
- [116]Bello, J.-L. *et al.* Impact of interfaces on magnetic properties of $Gd_x(Fe_{90}Co_{10})_{1-x}$ alloys. *Applied Physics Letters* **121**, 212402 (2022).
- [117]Malinowski, G., Hehn, M. & Panissod, P. Impact of the interface magnetic disorder on the exchange bias between ferromagnetic and antiferromagnetic layers. *Journal of Physics: Condensed Matter* **18**, 3385–3391 (2006).
- [118]Moritz, J., Vinai, G. & Dieny, B. Large Exchange Bias Field in (Pt/Co) \times 3/IrMn/Co Trilayers With Ultrathin IrMn Layers. *IEEE Magnetics Letters* **3**, 4000204–4000204

- (2012).
- [119]Moritz, J., Bacher, P., Auffret, S. & Dieny, B. Interlayer coupling between out-of-plane magnetized multilayers across a thin antiferromagnetic spacer. *Journal of Magnetism and Magnetic Materials* 323, 2391–2397 (2011).
- [120]Castro, I. L. et al. The role of the (111) texture on the exchange bias and interlayer coupling effects observed in sputtered NiFe/IrMn/Co trilayers. *Journal of Applied Physics* 113, 203903 (2013).
- [121]Xu, Y., Ma, Q., Cai, J. W. & Sun, L. Evidence of bulk antiferromagnet spin rearrangement during ferromagnetic layer reversal in a double exchange bias sandwich. *Physical Review B* 84, (2011).
- [122]Zhan, X. Z. et al. Probing the Transfer of the Exchange Bias Effect by Polarized Neutron Reflectometry. *Scientific Reports* 9, 6708 (2019).
- [123]Nam, D. N. H. et al. Propagation of exchange bias in CoFe/FeMn/CoFe trilayers. *Applied Physics Letters* 93, 152504 (2008).
- [124]Dalla Longa, F., Kohlhepp, J. T., de Jonge, W. J. M. & Koopmans, B. Resolving the genuine laser-induced ultrafast dynamics of exchange interaction in ferromagnet/antiferromagnet bilayers. *Physical Review B* **81**, (2010).
- [125]Ma, X. et al. Ultrafast spin exchange-coupling torque via photo-excited charge-transfer processes. *Nature Communications* **6**, (2015).
- [126]Kumberg, I. et al. Accelerating the laser-induced demagnetization of a ferromagnetic film by antiferromagnetic order in an adjacent layer. *Physical Review B* **102**, (2020).
- [127]Peeters, M. J. G., van Ballegoie, Y. M. & Koopmans, B. Influence of magnetic fields on ultrafast laser-induced switching dynamics in Co/Gd bilayers. *Physical Review B* **105**, (2022).
- [128]Zhang, W. et al. Role of spin-lattice coupling in ultrafast demagnetization and all optical helicity-independent single-shot switching in $[\text{SEP}]_{\text{Gd}}^{[\text{SEP}]}\text{Gd}_{1-x-y}\text{Tb}_y\text{Co}_x[\text{SEP}]_{\text{Co}}^{[\text{SEP}]}$ alloys. *Physical Review B* **105**, (2022).
- [129]Alzate-Cardona, J. D., Sabogal-Suárez, D., Evans, R. F. L. & Restrepo-Parra, E. Optimal phase space sampling for Monte Carlo simulations of Heisenberg spin systems. *Journal of Physics: Condensed Matter* **31**, 095802 (2019).
- [130]Evans, R. F. L. et al. Atomistic spin model simulations of magnetic nanomaterials. *Journal of Physics: Condensed Matter* **26**, 103202 (2014).
- [131]Jakobs, F. et al. Unifying femtosecond and picosecond single-pulse magnetic switching in Gd-Fe-Co. *Physical Review B* **103**, (2021).
- [132]Ceballos, A. et al. Role of element-specific damping in ultrafast, helicity-independent,

all-optical switching dynamics in amorphous (Gd,Tb)Co thin films. *Physical Review B* **103**, (2021).

[133]Moreno, R., Ostler, T. A., Chantrell, R. W. & Chubykalo-Fesenko, O. Conditions for thermally induced all-optical switching in ferrimagnetic alloys: Modeling of TbCo. *Physical Review B* **96**, (2017).

[134]Kim, J. & Jung, I-H. Thermodynamic modelling of Mn-Y and Mn-Gd systems for application of RE in Mg alloy development. *Canadian Metallurgical Quarterly* **52**, 311–320 (2013).